

High Accuracy Measurement of the $^{238}\text{U}(\text{n},\gamma)$ Cross Section at the CERN n_TOF Facility

2014

Tobias Wright

School of Physics and Astronomy

The University of Manchester.

A thesis submitted to the University of Manchester for the degree of Doctor of
Philosophy in the Faculty of Engineering and Physical Sciences.



Contents

List of Figures	4
List of Tables	9
Abstract	10
Declaration	11
Copyright Statement	12
Acknowledgements	13
1 Introduction, Motivation and Objectives	15
1.1 Motivation	15
1.2 Nuclear data for nuclear technologies	17
1.3 Neutron cross sections	18
1.4 How to measure neutron capture cross sections	21
1.4.1 The time-of-flight method	22
1.4.2 Gamma ray detection techniques	24
1.5 Neutron time-of-flight facilities	25
1.6 Current status on ^{238}U $\sigma_{n,\gamma}$	26
1.7 Objectives	29
2 Experimental set-up	30
2.1 The n_TOF facility at CERN	30
2.2 Characteristics of the neutron beam	33
2.2.1 Neutron flux	33
2.2.2 Neutron beam profile	37
2.2.3 Neutron energy resolution	38
2.2.4 Neutron beam monitors	41
2.2.5 Data acquisition system (DAQ)	42

2.3	The n_TOF Total Absorption Calorimeter (TAC)	43
2.4	Experimental campaign	46
2.4.1	Samples	46
2.4.2	Beam intensity	47
2.4.3	Proportionality between detection systems	48
3	Operation and performance of the TAC	51
3.1	Event building: from BaF ₂ signals to TAC events	51
3.1.1	Pulse shape analysis for BaF ₂ signals	51
3.1.2	Digitiser's timing calibration	53
3.1.3	Deposited energy calibration	55
3.1.4	Coincidence analysis	57
3.1.5	Time-of-flight to neutron energy calibration	58
3.1.6	Dead-time and pile-up in the TAC	59
3.2	Backgrounds	62
3.2.1	Beam-off background	62
3.2.2	Beam-on (sample out) background	65
3.2.3	Neutron Scattering (Sensitivity) Background	67
3.3	Detection efficiency and analysis conditions	69
3.4	Effect of the γ -flash on the TAC	72
4	Analysis and results on ²³⁸U	74
4.1	²³⁸ U Data reduction: Yield procurement	74
4.1.1	Background subtraction	74
4.1.2	Pile-up and dead-time correction	81
4.1.3	Discussion on the high neutron energy limit	85
4.1.4	Yield creation using the Saturated Resonance Method	88
4.1.5	Uncertainties	91
4.2	²³⁸ U Cross section analysis	92
4.2.1	Resonance analysis below 5 keV	92
4.2.2	Analysis above 5 keV	99
4.3	Results for the ²³⁸ U(n, γ) cross section	99
4.3.1	Comparison and discussion with resolved resonance evaluated data below 5 keV	100
4.3.2	Comparison and discussion with unresolved resonance evaluated data	105
5	Summary and conclusions	107

<i>CONTENTS</i>	3
A ^{238}U Resonance paramters	110
References	122

List of Figures

1.1	Predicted worldwide electricity consumption [1].	16
1.2	Carbon emissions for different sources of energy [2].	17
1.3	Different partial cross sections for ^{238}U from the JEFF-3.1.2 library.	19
1.4	Breit-Wigner curves using partial and total widths for the first resonance in ^{238}U taking values from JEFF-3.1.2.	21
2.1	The lead spallation target used at n_TOF	31
2.2	An overview of the CERN accelerator complex and the n_TOF facility	32
2.3	An overview of the 200 m n_TOF beam line	32
2.4	The n_TOF evaluated neutron flux with and without borated water as a moderator and the corresponding uncertainties [3].	37
2.5	The n_TOF beam profile, measured and simulated (for two different collimators) [3].	38
2.6	The different effects that cause experimental resonance broadening. The total broadening is shown alongside the average spacing between resonances.	40
2.7	A demonstration of the expected ^{238}U resonance shape using the code SAMMY with and without the Resolution Function alongside experimental data.	41
2.8	The TAC in the experimental area.	43
2.9	One hemisphere of the borated polyethylene neutron absorber used during the campaign to reduce the background from scattered neutrons.	45
2.10	Digitised signals from the TAC (blue) and the reconstruction by the PSA routine (black)[4].	45
2.11	The samples used within the campaign: ^{238}U (left) and $^{\text{nat}}\text{C}$ (right).	47
2.12	Proton beam intensity distribution for LOW and MED pulses.	48
2.13	Silicon detector amplitude spectrum; the triton peak distinctly falls between the two dashed vertical lines.	49

3.1	AmBe spectra for an individual BaF ₂ crystal for two versions of the PSA routine. The two dashed lines represent the photopeak energy (4.440 MeV) and the single escape peak energy (3.929 MeV).	53
3.2	⁸⁸ Y decay scheme highlighting the two γ -rays used for the timing calibration.	54
3.3	Linear time calibration fits for four example flash-ADC modules which exhibit different internal clocks. Detector #14 (top right) is from the same module as the reference detector so is already synchronised.	54
3.4	Three amplitude spectra from detector #35 corresponding to ¹³⁷ Cs (top left), ⁸⁸ Y (top right) and AmBe (bottom left) with the Gaussian fits shown in red. Example fits to the four energy points are shown in the bottom right.	56
3.5	Example of a single BaF ₂ modules response to the two ⁸⁸ Y peaks over time. The shaded areas represent one channel either side of the mean value.	57
3.6	Individual detector resolutions for three separate energy points. . .	57
3.7	Left: ²³⁸ U time-of-flight spectrum showing the first four resonances included in the fit. Right: the fit to these data and the values found in the nuclear data libraries to determine the neutron energy calibration parameters.	59
3.8	Time interval distributions for initial signals (E_1) between 6 and 6.5 MeV and subsequent (E_2) signal amplitudes.	61
3.9	Dead-time values for the TAC for all combinations of (E_1) and (E_2). .	61
3.10	Typical TAC deposited energy spectra for the neutron energy ranges 1 eV-10 keV (left) and 1 keV-10 keV (right).	62
3.11	A typical neutron energy spectrum for the analysis conditions $m_{cr} > 1$ and $2.5 < E_{sum}(\text{MeV}) < 5.75$	63
3.12	Beam-off deposited energy spectra for runs with and without the ²³⁸ U sample present on linear scale (above) and log scale (below). .	64
3.13	Experimental beam-off neutron energy spectra with the sample present and the corresponding fits for different analysis conditions in linear (above) and log (below) scales.	65
3.14	Sample out deposited energy spectra after subtracting the beam-off background with different cuts in multiplicity for 1-10 keV neutrons in linear scale (above) and logarithmic scale (below).	66

3.15	The theoretical carbon yield (left), using the cross section from JEFF-3.1.2 and the measured experimental carbon yield (right) for different cuts in multiplicities.	68
3.16	The neutron sensitivity for different multiplicities in the TAC. . . .	69
3.17	TAC ^{238}U deposited energy spectra in linear (above) and logarithmic (below) for the neutron energy range 1-10 eV.	70
3.18	An approximation of the experimental yield (ignoring neutron scattering and pile-up/dead-time corrections) of the first ^{238}U resonance for different analysis conditions compared to the expected yield as predicted by SAMMY from the JEFF-3.1.2 ^{238}U cross section. . . .	72
3.19	The neutron energy interval 1-100 eV for ^{238}U and background (sample out) data with and without conditions.	72
3.20	The response of a single BaF_2 crystal to the γ -flash.	73
4.1	^{238}U , sample out and beam-off neutron energy spectrum.	75
4.2	Expected ^{238}U neutron scattering contribution for the chosen analysis conditions of $m_{cr} > 1$ and $2.5 < E_{sum}(\text{MeV}) < 5.75$ taking the resonance parameters in the JEFF-3.1.2 database.	76
4.3	^{238}U and carbon deposited energy spectrum in the neutron energy range 1 keV to 10 keV for $m_{cr} > 2$. The carbon spectrum has been scaled to match the number of ^{238}U counts above 7 MeV to allow an estimation of the scattering contribution within the ^{238}U analysis conditions chosen ($m_{cr} > 1$ and $2.5 < E_{sum}(\text{MeV}) < 5.75$).	78
4.4	Three example resonances (top: 36.7 eV, middle: 347.8 eV, bottom: 991.8 eV) and their neutron scattering contribution as determined experimentally.	79
4.5	Neutron scattering contribution at high neutron energies for ^{238}U with 20 bins per decade.	81
4.6	^{238}U count rate for minimal conditions ($m_{cr} > 0$, $E_{sum} > 1$ MeV) for the two pulse intensities used for this work.	82
4.7	Three example resonances (top: 6.7 eV, middle: 20.9 eV, bottom: 66.1 eV) corresponding to different count rates before and after applying the dead-time correction.	84
4.8	The evaluated neutron flux in the energy region 10 to 50 keV highlighting the structures present within this energy region.	85
4.9	^{238}U neutron spectrum for differing pulse intensities; the points at which these data sets deviate indicate the effect of the γ -flash. . . .	86
4.10	^{238}U counting rate for LOW and MED pulses at high neutron energies.	87

4.11	^{238}U total number of counts for the two binnings used for this analysis.	88
4.12	The first 6.7 eV saturated ^{238}U resonance as fitted by SAMMY. . .	89
4.13	The saturated peak of the first 6.7 eV ^{238}U resonance as fitted by SAMMY.	89
4.14	The second saturated resonance of ^{238}U as fitted by SAMMY, where the normalisation has been taken from the first resonance and only the neutron energy has been left as a free parameter within the fit.	90
4.15	The third saturated resonance of ^{238}U as fitted by SAMMY, where the normalisation has been taken from the first resonance and only the neutron energy has been left as a free parameter within the fit.	91
4.16	The remaining background levels found in the valleys between ^{238}U resonances as fitted by SAMMY.	92
4.17	SAMMY fits (red) to experimental data (black) in the neutron energy interval 1-100 eV.	93
4.18	SAMMY (red) to experimental data (black) fits in the neutron energy interval 100-200 eV.	93
4.19	SAMMY (red) to experimental data (black) fits in the neutron energy interval 200-300 eV.	94
4.20	SAMMY (red) to experimental data (black) fits in the neutron energy interval 300-500 eV.	94
4.21	SAMMY fits (red) to experimental data (black) in the neutron energy interval 500-700 eV.	94
4.22	SAMMY fits (red) to experimental data (black) in the neutron energy interval 700-1000 eV.	95
4.23	SAMMY fits (red) to experimental data (black) in the neutron energy interval 1-1.5 keV.	95
4.24	SAMMY fits (red) to experimental data (black) in the neutron energy interval 1.5-2 keV.	95
4.25	SAMMY fits (red) to experimental data (black) in the neutron energy interval 2-2.5 keV.	96
4.26	SAMMY fits (red) to experimental data (black) in the neutron energy interval 2.5-3 keV.	96
4.27	SAMMY fits (red) to experimental data (black) in the neutron energy interval 3-3.5 keV.	96
4.28	SAMMY fits (red) to experimental data (black) in the neutron energy interval 3.5-4 keV.	97
4.29	SAMMY fits (red) to experimental data (black) in the neutron energy interval 4-4.5 keV.	97

4.30	SAMMY fits (red) to experimental data (black) in the neutron energy interval 4.5-5 keV.	97
4.31	Experimental data for 20 bins/decade (black) and 10000 Bins/decade (red) in the neutron energy interval 1-30 keV.	99
4.32	Ratios of all resonance kernels below 5 keV from the SAMMY fits and the ENDF/B-VII.1 and JEFF-3.1.2 libraries, where the starred points represent resonances where the kernels are the same in both evaluated libraries. The SAMMY fits to the resonances circled in blue are shown in Figure 4.34	100
4.33	Ratios of all resonance kernels below 5 keV from the SAMMY fits and the ENDF/B-VII.1 and JEFF-3.1.2 libraries, where the starred points represent resonances where the kernels are the same in both evaluated libraries excluding the 1211 eV resonance. The SAMMY fits to the resonances circled in blue are shown in Figure 4.34	101
4.34	Experimental data (black) and fits (red) for four example resonances compared to the ENDF/B-VII.1 (blue) and JEFF-3.1.2 (green) libraries.	102
4.35	Projections of the resonance kernel ratios between TAC data and the ENDF/B-VII.1 and JEFF-3.1.2 libraries for different energy regions. Above 1 keV the two libraries are equal therefore just one projection is shown.	102
4.36	Kernel ratios as a function of the resonance kernel.	103
4.37	Projections of the TAC/evaluated resonance kernels for two regions: weak and strong resonances. The dashed lines represent Gaussian fits to the data and the horizontal lines are the full width at half maximum.	104
4.38	Unresolved resonance capture yield compared to current JEFF and ENDF evaluations.	105

List of Tables

1.1	A comparison of the two main European time-of-flight facilities, n_TOF and GELINA who differ in their neutron production methods.	26
1.2	Summary of the current and requested uncertainties for the $^{238}\text{U}(n,\gamma)$ cross section as stated in the NEA HPRL [5].	28
2.1	Neutron induced reaction cross sections considered standard by the IAEA.	33
2.2	The detectors and reactions used to determine the neutron flux . .	35
2.3	Integrated number of neutrons per nominal proton pulse (7×10^2 protons) in each energy decade corresponding to the capture set up with borated water as a moderator.	36
2.4	Details of time allocation to each particular sample configuration. .	46
2.5	Details of the samples used during the experimental campaign . . .	47
2.6	Ratios of counts between detectors used during the ^{238}U runs. . . .	50
3.1	Approximate TAC efficiencies for different analysis conditions. . . .	71
4.1	Expected scattering contribution for s-wave resonances in different neutron energy regions.	77
4.2	Summary of all the uncertainties related to the experimental ^{238}U capture yield.	91
4.3	^{238}U resonance parameters from the performed SAMMY fits and the JEFF-3.1.2 and ENDF/B-VII.1 libraries. The first three resonances (marked with *) were saturated, thus could not be correctly fitted. .	98
4.4	Comparison of experimental and evaluated data for the $^{238}\text{U}(n,\gamma)$ cross section in the energy interval 3 keV - 25 keV.	106
A.1	^{238}U resonance parameters. Resonances marked with * should be assigned a larger uncertainty due to the large multiple scattering contribution. Furthermore, the first three resonances (marked with ^a) were saturated therefore could not be correctly fitted.	110

Abstract

ABSTRACT OF THESIS submitted to The University of Manchester by Tobias Wright for the Degree of Doctor of Philosophy and entitled: High Accuracy Measurement of the $^{238}\text{U}(\text{n},\gamma)$ Cross Section at the CERN n_TOF Facility.

Date of submission: 27/03/2014

The radiative capture cross section of a highly pure (99.999%), 6.125(2) grams ^{238}U sample ($(9.56\pm0.05)\times10^{-4}$ atoms/barn) has been measured in the 185 m flight path at the CERN neutron time-of-flight facility n_TOF in the energy range 0.3 eV-20 keV. The Total Absorption Calorimeter (TAC) detection system, an array of 40 BaF₂ crystals, was used utilising the total absorption technique, where all the γ -rays from the capture cascades are detected. These data have undergone careful background subtraction, with special care being given to the background originating from neutrons scattered by the ^{238}U sample. Pile-up and dead-time effects have been corrected for using an innovative correction method valid for variable high count rates within a complex detection system such as the TAC. The resulting capture yield has an uncertainty of up to 2.2% below 5 keV and up to 3.7% between 5 and 20 keV, in line with the accuracy requested in the NEA High Priority Request List. A resonance analysis has been performed up to 5 keV with the code SAMMY. Between 5 and 20 keV, the cross section is treated as unresolved and averaged. The results confirm the excellent quality of the most recent nuclear data evaluations within quoted uncertainties and suggest some improvements. In particular, these TAC data suggest a 2% increase in the average cross section in the energy range 2-9 keV and a 5% reduction in the energy range 9-20 keV.

Declaration

No portion of the work referred to in the thesis has been submitted in support of an application for another degree or qualification of this or any other university or other institute of learning.

Copyright Statement

The author of this thesis (including any appendices and/or schedules to this thesis) owns certain copyright or related rights in it (the Copyright) and he has given The University of Manchester certain rights to use such Copyright, including for administrative purposes.

Copies of this thesis, either in full or in extracts and whether in hard or electronic copy, may be made only in accordance with the Copyright, Designs and Patents Act 1988 (as amended) and regulations issued under it or, where appropriate, in accordance with licensing agreements which the University has from time to time. This page must form part of any such copies made.

The ownership of certain Copyright, patents, designs, trade marks and other intellectual property (the Intellectual Property) and any reproductions of copyright works in the thesis, for example graphs and tables (Reproductions), which may be described in this thesis, may not be owned by the author and may be owned by third parties. Such Intellectual Property and Reproductions cannot and must not be made available for use without the prior written permission of the owner(s) of the relevant Intellectual Property and/or Reproductions.

Further information on the conditions under which disclosure, publication and commercialisation of this thesis, the Copyright and any Intellectual Property and/or Reproductions described in it may take place is available in the University IP Policy (see <http://documents.manchester.ac.uk/DocuInfo.aspx?DocID=487>), in any relevant Thesis restriction declarations deposited in the University Library, The University Library's regulations

(see <http://www.library.manchester.ac.uk/aboutus/regulations/>) and in The University's policy on Presentation of Theses.

Acknowledgements

I would like to acknowledge financial support from the Nuclear Decommissioning Authority (NDA) for funding of the research project and industrial supervision, both managed on behalf of NDA by the National Nuclear Laboratory.

I would like to thank my University of Manchester supervisor Prof. Jon Billowes for securing and giving me the opportunity to work within the nuclear physics group. Through his hard work he has given me every opportunity I could have imagined throughout this PhD to further myself as both a scientist and as a person and has had faith in me right from the beginning, for which I am eternally grateful. Alongside the academic supervision and knowledge Jon has passed onto me, there has also been many memorable moments including some evenings at CERN which are eternally cemented in my memory.

I sincerely thank Dr. Carlos Guerrero, my supervisor from the n_TOF collaboration, CERN for truly taking me under his wing. Working with Carlos has been an honour and there has never been a dull moment. I thought it would be difficult working so closely with someone in a different country, but through the hard work of Carlos the level of supervision I have received has never faltered, in fact never even moved from 100%. This is despite him being seemingly involved in every experiment pertaining to nuclear data throughout Europe. From first meeting Carlos walking down the tunnel during a late evening at CERN, I knew he was a person that not only was a brilliant scientist but also had great personal qualities, making me feel welcome in a new, alien and quite terrifying place. I feel very privileged that we have worked in such close contact for so long, so thank you Carlos!

Throughout my PhD I have been incredibly lucky to have worked in many different places with many different great people. From the University of Manchester, I would like to thank all the students I have shared an office with for making it such an enjoyable experience but in particular Dr. Andrew Pollitt for any linux problems I ran into and Dr. Tim Ware for helping me throughout the first two years. At CERN, there are many people who have made visiting such an enjoy-

able experience but in particular I would like to thank Prof. Enrico Chaiveri, the spokesperson for the n_TOF collaboration who made me feel part of the team so easily, Dr. Eric Berthoumieux for help with any problem I came up against, Dr. Frank Gunsing for many interesting conversations and to the Italian team of Dr. Cristian Massimi and Federica Mingrone for working with me on the ^{238}U data. I have made a life long friend in Dr. Jonathan Duplissy, from the CLOUD collaboration at CERN who I shared a flat with for many months in Ferney Voltaire. Lastly, I owe a huge amount to Ben Buckland, a great friend in Geneva who has been continuously letting me sleep on his sofa during my repeated return trips to CERN.

I was lucky enough to spend some time working with the team at CIEMAT, who developed many of the tools used within this work so I would like to thank Dr. Daniel Cano-Ott and Emilio Mendoza for their patience, knowledge and teaching during that period. Also, Carlos Javier for showing me around Madrid and teaching me about the Spanish fiesta.

From IRMM, GEEL I would like to thank Dr. Peter Schillebeeckx for his constant enthusiasm and insightful contributions to this work but especially for coordinating the ^{238}U ANDES contribution.

From the NNL I would like to thank Dr. Robert Mills for providing Industrial supervision and expert knowledge on all aspects on nuclear data.

Thank you to my family and Becky, for putting up with a lot and always being there when I needed them. Especially Becky, who has put up with a lot of travelling, working and uncertainty that many people wouldn't take.

CHAPTER 1

Introduction, Motivation and Objectives

Nuclear energy is a vital part of the worldwide energy mix, and the United Kingdom's (UK) nuclear industry in particular is undergoing a strong rejuvenation as the current fleet of nuclear reactors come to the end of their lives. As will be shown, an accurate knowledge of nuclear data is crucial in all aspects of the nuclear industry, and this manuscript deals with a key isotope relevant to all generations, models and types of nuclear reactor. The epithermal capture cross section of this isotope, ^{238}U , is especially crucial to the next generation of nuclear reactors, therefore this work is very timely providing a modern and accurate measurement of the $^{238}\text{U}(\text{n},\gamma)$ cross section to aid development within the industry.

1.1 Motivation

The United Nations predict the world population will increase by 2 billion to 8.7 billion by 2035 which undeniably stipulates a large increase in energy production. Notably, as can be seen in Figure 1.1, electricity use is increasing twice as fast as overall energy use and is likely to rise by more than two-thirds by 2035, thus the global demand for cleanly-generated electricity is gigantic and a challenge.

Currently, nuclear power is responsible for producing only around 11% of the world's electricity despite it being more environmentally friendly than the three other main methods of electricity production on a large scale today, as illustrated in Figure 1.2. Electricity generated from nuclear power is virtually carbon free, however this isn't the only benefit it has compared to the other three largest global electricity producers: coal ($\sim 41\%$), natural gas ($\sim 22\%$) and hydro ($\sim 16\%$) [1]. Nuclear provides base load electricity steadily throughout the day, which is

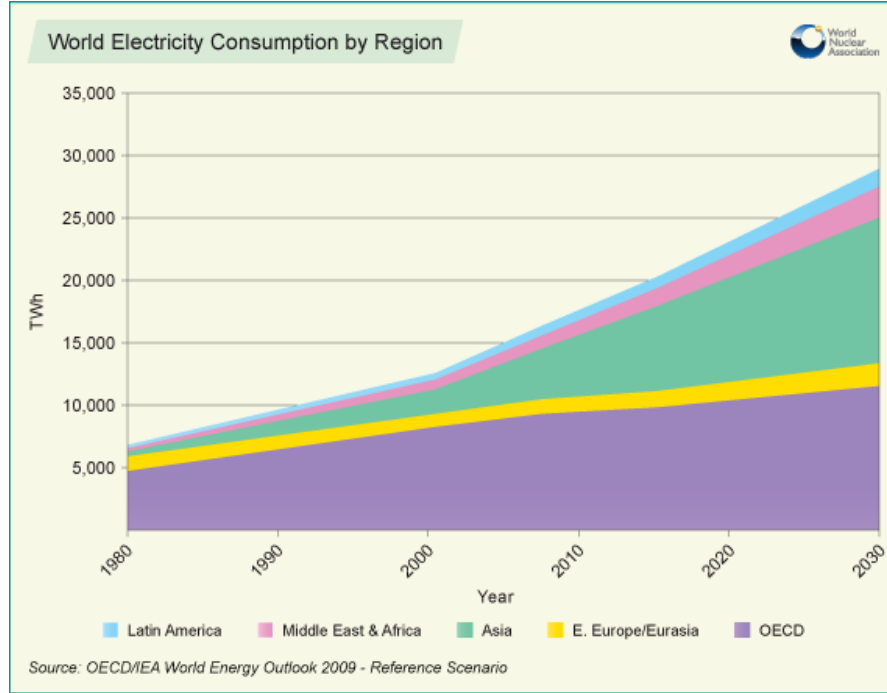


Figure 1.1: Predicted worldwide electricity consumption [1].

something hydro and other renewable energy sources cannot achieve due to their reliance on natural phenomena. Furthermore, nuclear power uses as its primary fuel uranium, which is plentiful, giving an impressive security of supply compared to the vulnerability of relying on other countries to supply oil and gas. Moreover the economics of nuclear power are further improving as the price of fossil fuels continues to increase, and governments give incentives to encourage carbon reductions. Finally, the majority of the costs for nuclear energy is in the capital cost of the plant itself, giving long term security to the final electricity production costs since any fluctuations or increases in fuel prices contribute a very small proportion to the end electricity production cost.

These attractive qualities have led to a so called nuclear renaissance and in particular the UK has committed to replace the 16 operating reactors which will soon be reaching the end of their lifetimes. There is one common feature amongst all 16 reactors, and even common to the first ever man made nuclear reactor by Enrico Fermi in 1942, known as Chicago Pile-1 [6] which is that they all use uranium as a fuel. The basis of any nuclear reactor is accurately understanding how the fundamental subatomic neutral particle, the neutron interacts with the materials within the reactor, of which in the vast majority of cases contains uranium. As will be explained in Section 1.3, the neutron interacts with each material in a variety of ways, and each interaction is governed by a probability depending on the energy of the neutron known as the *cross section*. These cross sections change drasti-

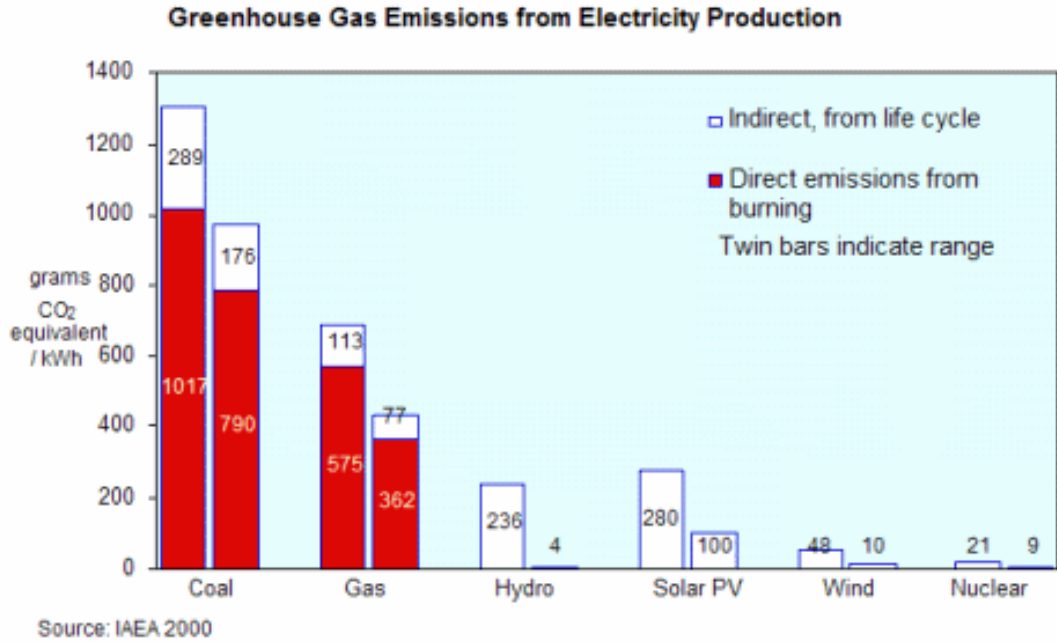


Figure 1.2: Carbon emissions for different sources of energy [2].

cally from isotope to isotope, and microscopic and phenomenological models are unable to recreate these interaction probabilities accurately, therefore these cross sections must be measured in dedicated experiments. The motivation for measuring new neutron cross sections is clear; new designs of reactors require previously unmeasured cross sections and higher accuracies. This thesis deals with one such measurement; namely the measurement of the ^{238}U radiative capture cross section which will be detailed in the following pages.

1.2 Nuclear data for nuclear technologies

Nuclear data is a collection of quantifiable information relating to the structure, decay or interaction of nuclei. These physical quantities are of vital importance to many fields, from fundamental nuclear physics to the space industry, however the biggest user of these data sets is the one of most interest: the nuclear energy industry. These data may come from models, measurements and evaluations. In the case of measured data they are included within EXFOR (Experimental Nuclear Reaction Data) [7]. This is a database coordinated by the International Atomic Energy Agency with contributions from national, regional and specialised nuclear reaction data centres which contains an extensive compilation of experimental nuclear reaction data. These data are made available to the global community; as

of November 2013 in total it contains information from 20160 experiments which forms the backbone of nuclear data. In our case, the nuclear data of interest are neutron cross sections, specifically neutron capture cross sections and one can use EXFOR as a tool to view all previous $^{238}\text{U}(n,\gamma)$ measurements performed. Each of these entries within EXFOR contains not just any experimental results found, but also all possible further information about the experiment such as research facility, measuring temperature and sample information.

A wealth of information is available to the industrial community through EXFOR, however these data must go through an evaluation stage before it is presented to industry. An evaluation is required because an individual measurement could only contain partial data for example in a small energy region and it could be inaccurate or even completely wrong. The goal of an evaluation is to create an evaluated data file for each isotope containing information on all reaction channels across the full energy range. This is done by putting together all the experimental information and also the models for any information that may be missing.

Nuclear energy agencies produce a final nuclear data library which gives the best results when used within industry. Examples of these nuclear data libraries are ENDF/B-VII.1 (USA, 2011) [8], JEFF-3.1.2 (Europe, 2012) [9], JENDL-4.0 (Japan, 2012) [10], CENDL-3.1 (China, 2009) [11] and Brond 2.2 (Russia, 1992) [12]. These data libraries are upgraded to take into account new available data or evaluation techniques. A recent project, CIELO (**C**ollaborative **I**nternational **E**valuated **L**ibrary **O**rganization) [13], aims to produce an evaluated library common to Europe, North America and Asia - an unprecedented task. One isotope under study for this project is ^{238}U , due to its key relevance within the nuclear industry, and the results of the measurement presented in this manuscript shall contribute to this project, as discussed at the inaugural meeting [14].

The NEA (**N**uclear **E**nergy **A**gency) manages the High Priority Request List [5], a set of industrial and scientific requests deemed of high importance to current and future technologies which require new measurements to be performed. Here one finds the most current and pressing nuclear data requests, of which currently there are 36. One of these requests is for the $^{238}\text{U}(n,\gamma)$ cross section, solidifying the importance of a new measurement of this quantity.

1.3 Neutron cross sections

The neutron cross section σ is a physical quantity representing the probability of a neutron interacting with a specific nucleus. The total cross section gives the probability of any interaction, however this can be decomposed into a sum of

partial cross sections, each giving the probability of a neutron undergoing a certain reaction with that nucleus:

$$\sigma_{total} = \sigma_{capture} + \sigma_{fission} + \sigma_{scattering} + \dots, \quad (1.1)$$

The three examples of interactions given in Equation 1.1 are three of the most important within a nuclear reactor, however are by no means comprehensive. Indeed, in the nuclear data libraries ^{238}U cross section data are held for over 50 reactions. The concept of a nuclear cross section is easily understood if one thinks of the neutron as a classical point particle and nuclei as solid spheres. Then, as the area of the nucleus increases (its apparent cross section), the interaction probability of the neutron also increases. From this view, cross sections are usually measured in barns, where one barn is 10^{-24} cm^2 , which is approximately the cross sectional area of a single uranium nucleus. Figure 1.3 gives an example of the current neutron capture (n, γ), neutron fission (n,f) and neutron elastic scattering (n,n) cross sections in JEFF-3.1.2 for ^{238}U .

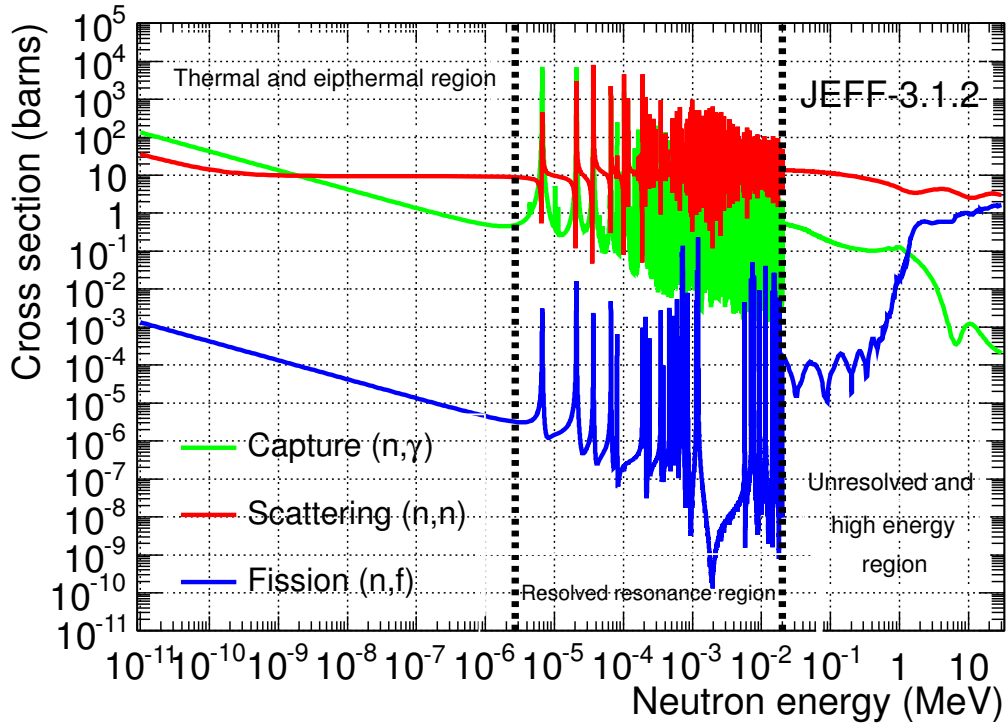


Figure 1.3: Different partial cross sections for ^{238}U from the JEFF-3.1.2 library.

There are three clear energy regions marked on Figure 1.3, which are typical to heavy nuclei and each have specific characteristics:

1. Thermal and eipthermal region: Between the thermal point (25 meV) and

the first resonant structure (eV region), the cross section is smooth and is proportional to the time the neutron spends within close contact of the nucleus. This is commonly thought of as the $\frac{1}{v}$ or $\frac{1}{\sqrt{E}}$ region, as $\sigma \sim t \sim \frac{1}{v} \sim \frac{1}{\sqrt{E}}$.

2. Resolved resonance region: From the first resonance structure up to a few keV (depending on the nucleus), structures are seen where the cross section rapidly changes many orders of magnitude. These structures are due to unbound levels in the compound nucleus ($n + {}^{238}\text{U} \rightarrow {}^{239}\text{U}^*$), as will subsequently be described.
3. Unresolved and high energy region: As the neutron carries more energy the compound nucleus is formed in a more excited state and the resonances start to overlap as their intrinsic widths become comparable to the distance between resonances (Unresolved resonance region). Eventually, the distance between resonances becomes smaller than their intrinsic widths and all resonance structure is lost (high energy region).

This work deals with the epithermal/resolved resonance region, therefore it is this that will be the focus of the following sections. To explain the observed resonance structure, one must utilise the theory of the compound nucleus. This is the production of a nucleus in an excited state by the addition of a neutron with energy E_n . This so called compound nucleus has an excitation energy of approximately $E^* = S_n + \frac{A}{A+1}E_n$, where A is the atomic mass of the nucleus and S_n is the neutron separation energy of the compound nucleus, which for ${}^{239}\text{U}^*$ is 4806.38 ± 0.17 keV. At certain energies, this excitation energy gives rise to a configuration within the nucleus which is quasi-stationary, known as a resonance and defined by its half life τ , which is intrinsically related to the resonance width, Γ ($\Gamma \propto \frac{1}{\tau}$). Furthermore, each resonant state of the nucleus has a corresponding energy, spin and parity. This excitation energy is lost either via the emission of radiation (neutron capture), two or more fragments (fission), a subsequent neutron with equal (elastic scattering) or lower (inelastic scattering) energy, or any other open reaction channel.

A good approximation to describe the shape of the resonances is with the *Breit-Wigner* formula, formulated by G. Breit and E. Wigner in 1936 to describe the capture of slow neutrons [15] which is given here for a resonance at energy E_0 in a simplified form:

$$\sigma(E) \sim \frac{\Gamma^2}{(E - E_0)^2 + \frac{\Gamma^2}{4}}. \quad (1.2)$$

The resonance width can be composed by the summation of a set of partial widths relating to the individual decay probability from each channel. For example in the resolved resonance region of ^{238}U these would be capture (Γ_γ), fission (Γ_f) and scattering (Γ_n) widths. Figure 1.4 demonstrates the Breit-Wigner curves corresponding to the partial widths found in JEFF-3.1.2 for the first ^{238}U resonance (6.67 eV) (Γ_f is negligible for this resonance).

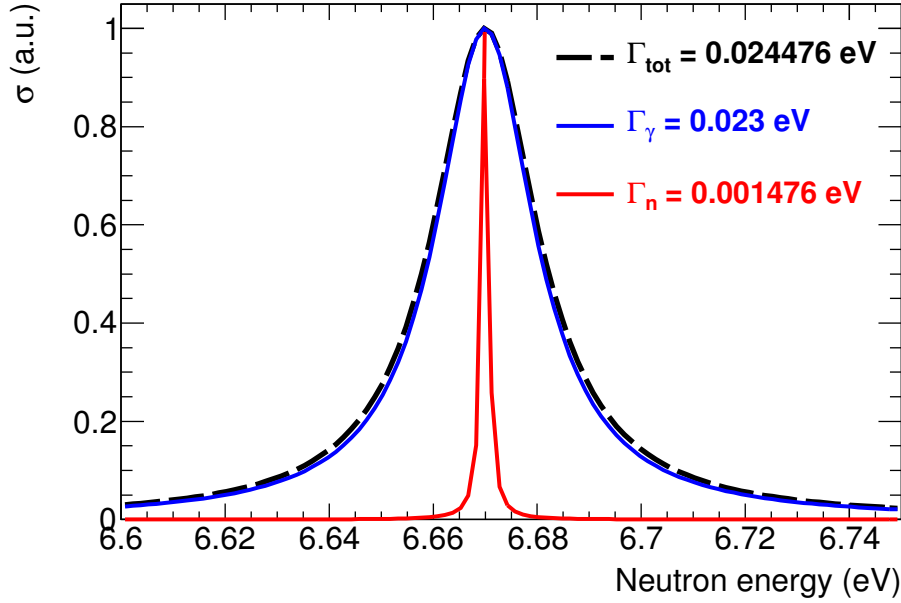


Figure 1.4: Breit-Wigner curves using partial and total widths for the first resonance in ^{238}U taking values from JEFF-3.1.2.

These partial widths contribute towards a nuclide's resonance parameters, which are what are found in nuclear data libraries within the resolved resonance region, rather than a point-wise cross section. The underlying theory of this resonance description is given by the *R-matrix* formalism, of which more details can be found in the references [16] and [17].

1.4 How to measure neutron capture cross sections

The concept of a cross section can be understood from an experimental point of view. If we consider a neutron source with intensity I (neutrons/s) impinging upon a thin sample of an isotope with a density of nuclei N (nuclei/cm³) and thickness Δx (cm) then the reaction rate R (reactions/s) is proportional to the number of

neutrons and target nuclei with the cross section (σ) providing the proportionality constant between the two:

$$R = \sigma \cdot I \cdot (N \cdot \Delta x), \quad (1.3)$$

therefore to perform a partial cross section measurement, it is clear that the requirements are: a source of neutrons of known intensity, a set-up to measure the reaction rate and finally a well characterised sample. To measure this partial cross section, one must detect the secondary particles emitted in the reaction; in the case of neutron capture these are γ rays.

To measure the cross section at a single energy point, a mono-energetic neutron source can be used, for example the nuclear fusion of a deuterium and tritium atom results in the ejection of a 14.1 MeV neutron. However, to perform an accurate cross section measurement across a wide range of energies the *time-of-flight* method is best.

1.4.1 The time-of-flight method

The time-of-flight method requires a pulsed neutron source from which the neutrons, with a distribution of energies, travel down an evacuated beam path for a known distance L . If the time of neutron production (t_{prod}) is known, one can calculate the time the neutron took to travel through the beam path before undergoing a capture reaction by measuring the time that the γ ray is detected (t_{det}). Since we know the mass of the neutron, ignoring relativistic effects we can calculate the energy of the neutron E_n :

$$E_n(\text{eV}) = \frac{1}{2}m_n v^2 = \left(\frac{72.2983 \cdot L(\text{m})}{t_{det}(\mu\text{s}) - t_{prod}(\mu\text{s})} \right)^2. \quad (1.4)$$

One important quality when performing a capture cross section measurement is the neutron energy resolution, especially if you are measuring individual resonances. Three factors affect this resolution:

1. Flight path length and uncertainty: A longer flight path has the advantage of a better energy resolution.
2. Time resolution of the detection system: This affects the uncertainty in t_{det} .
3. Spread in neutron production time: This affects the uncertainty in t_{prod} .

These points depend on the facility and detection systems being used. Different experimental facilities will be discussed in the following section (1.5) and the

specific case of interest for this work will be discussed in detail within Chapter 2.

The observable quantity during a capture cross section measurement is the experimental reaction yield ($Y_{n,\gamma}$). This is defined as the probability of a single neutron with a given energy undergoing a capture reaction:

$$Y_{n,\gamma} = \frac{C_{n,\gamma}(E_n) - B(E_n)}{\varepsilon_{n,\gamma}\phi_n(E_n)}, \quad (1.5)$$

where $C_{n,\gamma}(E_n)$ is the measured counting rate, $B(E_n)$ is the background counting rate, $\varepsilon_{n,\gamma}$ is the efficiency of the detection system for capture reactions and finally $\phi_n(E_n)$ is the incident neutron flux, which in the case of this work is defined as the number of neutrons integrated over the full spatial beam profile as a function of neutron energy (see Chapter 2). This capture yield is related to the capture and total cross sections as well as the areal density n (atoms/unit area) of the sample by:

$$Y_{n,\gamma}(E_n) = (1 - e^{-n\sigma_t(E_n)}) \frac{\sigma_{n,\gamma}(E_n)}{\sigma_t(E_n)}, \quad (1.6)$$

where the first term gives the probability of a neutron induced reaction taking place and the second term gives the probability that this is a capture reaction. The yield given by Equation 1.6 is to be considered ideal because it does not include a series of experimental effects that must be accounted for. These are:

1. Multiple scattering: There is a non negligible probability that an incident neutron is scattered one or more times within the sample before being subsequently captured at a different t_{det} and also with a different energy E_n , thus affecting the shape of a resonance. This depends on the sample size, and also the scattering to capture cross section ratio.
2. Thermal broadening: The target nuclei have some thermal motion, depending on the temperature of the sample. Therefore the incident neutron encounters the nuclei in motion and thus the kinetic energy of the neutron in the reference system of the nuclei is changing. The overall effect is a broadening of the observed resonances.
3. Resolution broadening: Neutrons entering the evacuated beam line with a given energy may have followed different paths and spent different times within the neutron production target, introducing a non-trivial relationship between the time-of-flight ($t_{det} - t_{prod}$) of the neutron and its energy. The overall effect is a broadening of the observed resonances and is known as the Resolution Function. This depends very much on the individual experimental

facility, and the Resolution Function for the n_TOF facility will be described in Section 2.2.3.

4. Self-absorption: γ rays produced within the sample can be absorbed by the sample itself, therefore losing energy or being absorbed prior to detection.

As mentioned earlier, within the resolved resonance region a cross section can be accurately described by a set of resonance parameters, therefore it is the goal of a capture measurement to obtain these. Typically, the measured capture yield is analysed by a code such as SAMMY [18] or REFIT [19], which allows one to extract the mentioned resonance parameters taking properly into consideration all the experimental effects stated above. In an iterative process, these codes take a set of initial resonance parameters and find final ones using a Bayesian (SAMMY) or Least-Squares (REFIT) fitting procedure to the experimental data.

1.4.2 Gamma ray detection techniques

As has been explained, to measure a capture cross section one must detect the γ rays produced within the subsequent EM cascade that allows the compound nucleus to reach the ground state from the initially excited state at an energy of $E = S_n + \frac{A}{A+1}E_n$. The detailed properties of the γ ray cascades change from isotope to isotope and due to the statistical nature of the deexcitation process one decay is completely different to the next one, only the total energy of the cascade remains constant. Therefore the goal in a capture cross section measurement is to be able to detect these cascades minimising the detection efficiency with respect to the properties of the cascades, which is not straightforward. The two most commonly used detection methods for this purpose are outlined below:

1. Total energy detectors: In this technique, based on an original idea from Maier-Leibnitz and first utilised in 1967 [20], a low efficiency γ ray detector is used such that only one γ ray out of the capture cascade is detected, however the detection efficiency is proportional to the γ ray energy. Under these conditions, the efficiency for detecting a cascade will be proportional to the total cascade energy and independent of the actual cascade path. In reality an ideal detector in which the efficiency is low and perfectly proportional to the γ ray energy does not exist. The problem is overcome by using the Monte Carlo based so-called Pulse Height Weighting Technique [21].
2. Total absorption detectors: In this technique, the best efforts are made to detect the complete cascade following a neutron capture reaction. The requirements for this method are a large solid angle coverage and high intrinsic

detection efficiency. Additionally, powerful background rejection capabilities are achieved when the detector also features segmentation, high photo peak efficiency and good energy resolution. An example of this detection set-up is the TAC at the n_TOF facility which will be extensively described in Chapter 3.

The two techniques have their individual advantages and disadvantages. Namely, the total absorption technique yields powerful background rejection capabilities and high efficiencies, however it may sometime suffer from neutron sensitivity and dead-time/pile-up issues. The total energy detectors can be very insensitive to neutrons and much less sensitive to γ rays, allowing measurements to continue to higher neutron energies where neutron scattering dominates over capture.

1.5 Neutron time-of-flight facilities

The main characteristics describing a time-of-flight facility are the flight path length and intensity and resolution of the neutron beam which is related to the neutron production method. The main method of neutron production for these measurements is either accelerated electrons or protons, which then cause photo-fission or spallation reactions respectively.

Facilities that are based upon an electron accelerator produce photons from Bremsstrahlung emission by the electrons impinging on a heavy target, which then undergo photo-fission reactions producing neutrons. Current operational facilities like this are GELINA [22] of the EC-JRC-IRMM [23] at GEEL in Belgium and the RPI facility [24] in New York state, USA. The ORELA facility [25] at Oak Ridge National Laboratory in Tennessee, USA was recently shut down, however in the past was a world leading time-of-flight facility based on an electron accelerator.

Facilities based upon a proton accelerator can produce neutrons through spallation reactions. Examples of operational spallation facilities are the n_TOF facility [3], at CERN in Switzerland, the LANSCE [26] facility at Los Alamos National Laboratory in New Mexico state, USA and ANNRI at the Japan Proton Accelerator Research Complex (J-PARC) project in Japan [27].

Some further considerations for each experimental facility are number of flight paths available, pulse repetition frequency and number of neutrons produced per burst all of which define the suitability of a facility for a particular measurement. Table 1.1 summaries the main characteristics of the two main European time-of-flight facilities, n_TOF and GELINA. A detailed investigation into these two specific time-of-flight facilities can be found in Reference [28].

Table 1.1: A comparison of the two main European time-of-flight facilities, n_TOF and GELINA who differ in their neutron production methods.

	n_TOF	GELINA
Incident particle	20 GeV proton	100 MeV electron
Production mechanism	Spallation	(γ, f)
Flight path	185 m ^a	30 m ^b
Average pulse frequency (Hz)	0.278	800
Pulse width (ns)	6	11
Energy range (eV)	0.025 - 10^9	10 - $4 \cdot 10^6$
$\Delta E/E$ @ 10 keV	0.05%	0.3%
$\Delta E/E$ @ 1 MeV	0.5%	<2%
$\phi_n(n/cm^2/s)$ (0.025 eV - 10 MeV)	$1.3 \cdot 10^5$	$3.3 \cdot 10^6$
$\phi_n(n/cm^2/pulse)$ (0.025 eV - 10 MeV)	$4.6 \cdot 10^5$	4160

^a A second, 20 m vertical flight path beam line will become on-line in 2014 [29].

^b GELINA has 12 flight paths between 10 and 400 m. Statistics corresponding to a single flight path are given here.

The two facilities are equivalent in most aspects (neutron energy resolution and time integrated neutron flux) however the neutron flux per pulse is far superior at the n_TOF facility. This characteristic especially lends itself to the measurement of radioactive samples, where the contribution from activity of the sample (proportional to the measuring time and thus inversely proportional to the number of neutrons per pulse) becomes the dominant source of background. On the whole however, for non or low level radioactive samples, such as the one of interest for this work, the biggest difference between the two facilities is from the backgrounds and individual experimental effects present within each facility. As will be discussed in the following section (1.6), measuring the same sample at both facilities provides complementary results, which can both reduce systematic errors and improve the current understanding of each facility.

1.6 Current status on ^{238}U $\sigma_{n,\gamma}$

Before 2008, the resonance parameters (up to 10 keV) of the ^{238}U evaluated neutron cross section were based on two high accuracy capture measurements from Moxon [30] and G. de Saussure *et al.* [31] in 1967 and 1973 respectively alongside numerous transmission measurements. The high importance of the ^{238}U capture cross section led to a recent evaluation by Derrien *et al.* [32] in 2008, the results of which the three main neutron cross section libraries (ENDF/B-VII.1, JEFF-3.1.2 and JENDL 4.0) have adopted. The new evaluation took into account the high-resolution neutron capture cross section measurement of G. de Saussure *et al.* and also

Macklin *et al.* [33] in 1991, which measured two samples of thicknesses 0.0031 and 0.0124 atoms/barn allowing the resolved resonance region to be extended up to 20 keV. The results from this evaluation are summarised in the following:

- From thermal up to 1 keV:
 - The thermal capture value was decreased by $\sim 0.4\%$ to $\sigma_0=2.683$ b, following the recommendation of Trkov *et al.* [34].
 - The shape of the capture cross section in this energy range was checked with the capture measurements of Crovi *et al.* [35]. The first three large s-wave resonances (6.7, 20.8 and 36.6 eV) were fitted with the seven transmission spectra of Olsen [36] and the four transmission measurements performed at room temperature at GELINA by Meister *et al.* [37] and the capture measurements of de Saussure *et al.* [31].
 - The capture data of de Saussure was found to be well normalised to the 6.7 eV resonance, but had to be significantly renormalised to be in agreement with the transmission data of Olsen (~ 1.08 at 100 eV).
 - From 250 eV to 1 keV the Macklin *et al.* capture measurements were included in the fit. In the region 250 -500 eV these data required an energy dependant normalisation and above 500 eV were also significantly renormalised (~ 1.08 at 500 eV).
- From 1 to 20 keV, capture data was fitted using SAMMY with the transmission data of Olsen *et al.* [38] and Harvey *et al.* [39]:
 - The simultaneous fit of transmission data and the capture data of de Saussure could not be obtained without first subtracting a background of 40 ± 20 mb followed by an unexplained energy dependant normalisation correction factor F [40]:

$$F = 0.845e^{0.38421\sqrt{E(\text{eV})}}. \quad (1.7)$$

- The Macklin data required a similar background subtraction of 85 ± 30 mb for the thin sample and 140 ± 60 mb for the thick sample followed by a normalisation of ~ 1.13 to agree with the transmission data.

It is noted that these two capture data included in the most recent evaluation had to be renormalised by sizeable factors and the these factors are not even constant in energy. One could conclude these capture experiments have suffered from large systematic (8-13%) errors. Indeed, discrepancies within these data sets

limit the uncertainty of the $^{238}\text{U}(n,\gamma)$ cross section. The required improvement of this for future nuclear reactors gave rise to the entry in the high priority request list (HPRL) [5], which is summarised in Table 1.2.

Table 1.2: Summary of the current and requested uncertainties for the $^{238}\text{U}(n,\gamma)$ cross section as stated in the NEA HPRL [5].

Neutron Energy	Current Uncertainty (%)	Requested Uncertainty (%)
22.6 - 454 eV	2	1
2.03 - 9.12 keV	3	1
9.12 - 24.8 keV	9	2 - 5

The low requested uncertainties are a result of the report [41], however the request states that “any attempt that significantly contributes to reducing the present accuracy for this quantity is strongly encouraged. Any such attempt will significantly enhance the accuracy with which reactor integral parameters may be estimated and will therefore impact economic and safety margins.”. The request is valid for a variety of innovative reactor systems, each of which requires specific accuracies hence the final uncertainty is quoted according to these different requirements.

Indeed, recently (2011) a new cross section measurement in the energy range 10 eV to 100 keV has been reported [42][43] using the DANCE calorimeter at the LANSCE facility; however, these data have been published so recently (March 2014) that no information is available in EXFOR thus we do not perform a comparison to these data. Furthermore, from the publication it is unclear whether these new data meets the demands from the NEA HPRL.

In light of this, a proposal to measure the $^{238}\text{U}(n,\gamma)$ cross section at both the n_TOF and GELINA facility using two different detection systems was accepted in 2009 [44] within task 1.2 of the EC-FP7 ANDES project [45]. Transmission measurements at the GELINA facility are also proposed under ANDES. The first capture detection technique proposed for the measurement was the total energy detection method, which requires γ ray detectors with a relatively low detection efficiency that is directly proportional to the γ ray energy. At n_TOF and GELINA, C_6D_6 detectors are used with a combination of the pulse height weighting technique [21]. The second detection method, which is the one utilised in this work, is the total absorption technique with the n_TOF Total Absorption Calorimeter (TAC) [4], described and discussed in Chapters 2 and 3.

By using two different detection techniques at two separate facilities, the overall systematic uncertainty is reduced; furthermore, each technique has its unique advantages and disadvantages thus they are complementary to each other. The C_6D_6 detectors are very inefficient at detecting neutrons, reducing any background

from neutrons scattered by the sample. Furthermore, they are not limited by any experimental conditions in neutron energy therefore can measure up to high neutron energies at n_TOF. In contrast, the TAC is limited by the so called γ -flash therefore has an upper limit on neutron energy of ~ 40 keV as will be explained in Section 4.1.3. However, as will become apparent in Chapter 3 the TAC has powerful background rejection capabilities, giving a better signal to background ratio than found with the C_6D_6 .

The measurement of the $^{238}\text{U}(n,\gamma)$ cross section with the TAC in the resolved energy region, between 1 and 20 keV is the focus of this PhD and will form the remainder of this manuscript.

1.7 Objectives

The objectives of this thesis is to obtain a $^{238}\text{U}(n,\gamma)$ capture yield from the TAC measurement at the n_TOF facility in the energy range 1 eV - 20 keV and where possible the corresponding resonance parameters with the lowest uncertainty achievable. To do this, the whole analysis procedure will be accurately documented, starting from the experimental set-up and the properties of the neutron beam leading on to the latter analysis stages, the usage of the TAC and finally the resonance analysis.

The uncertainties introduced within each stage of the analysis must be understood and correctly propagated leading to a final result that is accurate and trustworthy. The results of this work will aid the CIELO evaluation due in 2015 leading to the most accurate $^{238}\text{U}(n,\gamma)$ cross section to date. This manuscript aims to explain the complex analytical techniques and tools utilised throughout this work as well as presenting the results of this analysis. The final results will be compared to the evaluations, allowing a quantifiable comparison of this work with previous.

CHAPTER 2

Experimental set-up

Since 2001, the n_TOF facility has been operating at CERN as a neutron time-of-flight experiment which was first proposed by Rubbia et al [46] in 1998. The facility's history can be split into three main periods: phase one (2001/4), phase two (2008/12) and phase three (2014 onwards). These continuous upgrades have allowed many new and accurate cross section measurements to be completed. This chapter outlines the facility and its capabilities before describing the $^{238}\text{U}(n,\gamma)$ experimental campaign, corresponding to phase two. The samples and detectors used for the capture measurement are presented alongside information on the beam monitoring system and finally the quality checks performed.

2.1 The n_TOF facility at CERN

The neutron beam at n_TOF makes use of the high instantaneous flux of protons supplied by the CERN accelerator complex. Neutrons are produced via spallation reactions from 20 GeV/ c protons from the Proton Synchrotron (PS) impinging on a cylindrical lead target (40 cm in length and 60 cm in diameter). The target is surrounded by 1 cm of water, which serves as both a coolant and a moderator of the neutrons. The neutron spectrum is then further moderated by 4 cm of borated water ($\text{H}_2\text{O} + 1.28\%\text{H}_3\text{BO}_3$) surrounding the front face of the target, as seen in Fig. 2.1, producing a neutron spectrum from thermal up to GeV energies. The inclusion of borated water drastically reduces the in beam γ -ray background, caused by neutron capture reactions in hydrogen which are always followed by the emission of a 2.2 MeV γ -ray. The introduction of the cylindrical target and a separate cooling and moderation circuit in 2008 marks the beginning of phase two at n_TOF.

The current evacuated beam line, of 185 metres, is at a 10° angle with respect

to the proton beam and leads to the first experimental area (EAR-1). The second beam line, of 20 metres, leaves the target vertically with only the 1 cm layer of cooling water to moderate the neutron spectrum and leads to the second experimental area (EAR-2). The introduction of the second beam line in 2014 marks the beginning of phase three, and this new experimental area is yet to be commissioned. The experiment presented in this manuscript has been performed at the existing EAR-1 (185 m flight path) during 2011, thus during phase two. Figure 2.2 gives an overview of the n_TOF facility during phase two which will be discussed in the following sections. See Reference [47] for a more detailed discussion.

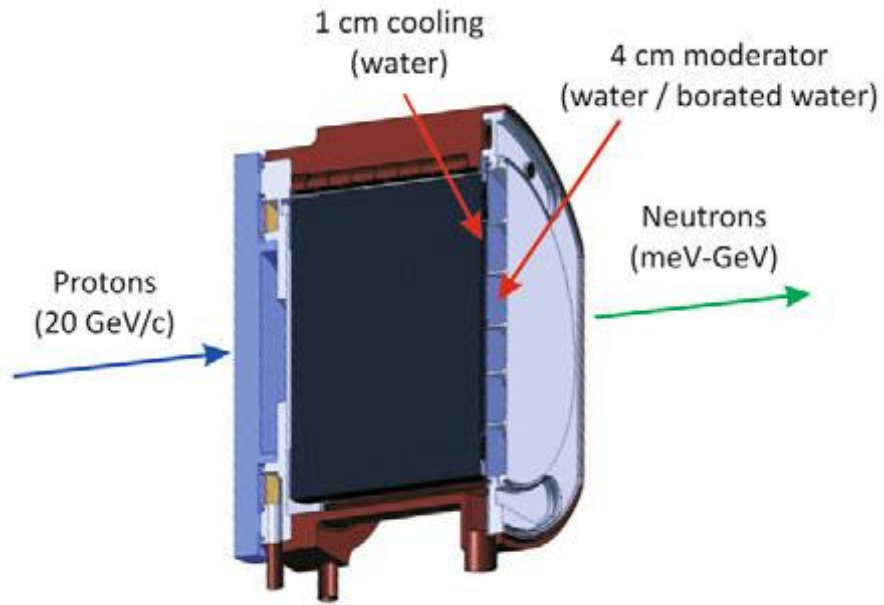


Figure 2.1: The lead spallation target used at n_TOF

The characteristics of the neutron beam are due to the proton beam, the target, coolant and moderator and finally the neutron beam line. The proton beam has a pulse width of ~ 7 ns, a maximum repetition rate of 0.4 Hz and a maximum intensity of $8 \cdot 10^{12}$ protons per pulse, however this can be reduced to lower values when needed. Around 600 neutrons are emitted per proton and the low repetition rate means there is no overlap of neutrons between pulses. The spallation reaction produces many particles other than neutrons, and their production is forward peaked thus the beam line is angled at 10° to the proton beam line to reduce the amount of in beam charged particles and γ -rays.

Figure 2.3 shows the full 200 m neutron beam line. Initially, the neutrons pass through a source screening collimator which is 2 m long, located 136.7 m after the target and is composed of 1 m of iron and 1 m of concrete. It has an inner diameter of 11.5 cm, and has historically been slightly misaligned to the beam

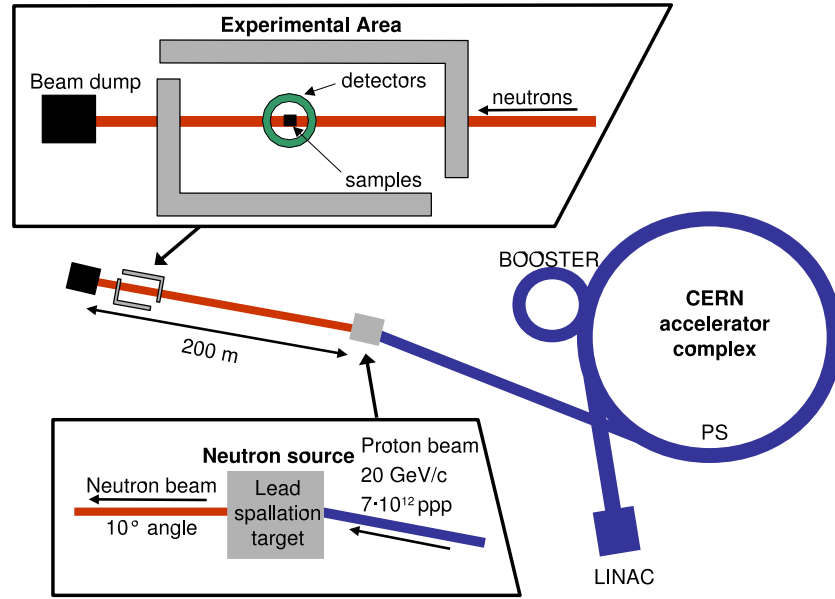


Figure 2.2: An overview of the CERN accelerator complex and the n_TOF facility

but during the long shut down of 2013/14 this is being realigned. At 145.4 m a 3.6 Tm sweeping magnet (200 cm long, 44 cm gap) deflects the charged particles in the beam. At a final stage before the experimental area, the neutrons pass through a beam shaping collimator which is situated 178 m after the target and has two working modes allowing the beam to be tailored for either capture or fission cross section measurements. For capture, a narrow beam is required and the collimator has a diameter of 18 mm with 235 cm of steel and 50 cm of borated polyethylene. Whereas for fission, a large beam is advantageous to allow the use of very thin samples so the diameter is 80 mm with 50 cm borated polyethylene, 125 cm of steel and 75 cm more borated polyethylene. We are interested in the capture beam, therefore it is this set up that will be described in the following sections. The neutrons then reach the experimental area, which is a cave 7.9 m long beginning 182.3 m from the target. Downstream from here at 200 m from the target there is a polyethylene beam dump situated in the so called escape line.

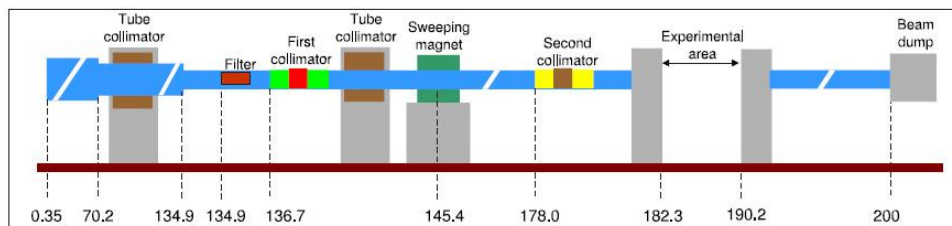


Figure 2.3: An overview of the 200 m n_TOF beam line

Any detector along the beam line observes a burst of relativistic particles after the spallation reaction. This is caused by the so called γ -flash which is comprised of high energy photons and charged particles. In principle, any charged particles produced in the lead target are swept away by the magnet however charged particles can subsequently be produced through the interaction of high energy neutrons and photons within the second collimator. The result within a detector is a signal which is usually saturating after which the detection system must take some time to recover. The timing of this signal is a useful reference measurement of the time of the spallation reaction, however the time a detector takes to recover from the γ -flash can limit the maximum neutron energy a detection system can measure up to.

2.2 Characteristics of the neutron beam

The main characteristics of a time-of-flight facility are the intensity, profile and energy resolution of the neutron beam, the beam monitors and the data acquisition system. This section outlines these features for the n_TOF facility.

2.2.1 Neutron flux

Within the n_TOF collaboration and for this work we refer to the neutron flux as the number of neutrons integrated over the full spatial beam profile as a function of neutron energy. This quantity is vital for all neutron time-of-flight experiments, and therefore any uncertainty in the flux propagates to the final result. In order to experimentally determine the neutron flux, one measures a neutron induced reaction which is defined as a standard [48]. This means the uncertainty of the reaction cross section is below 1%. The standard reaction cross sections and their corresponding energy ranges are shown in Table 2.1 as given by the IAEA [49].

Table 2.1: Neutron induced reaction cross sections considered standard by the IAEA.

Reaction	Energy range
$^1\text{H}(n,n)$	1 keV to 20 MeV
$^3\text{He}(n,p)$	0.0253 eV to 50 keV
$^6\text{Li}(n,t)$	0.0253 eV to 1 MeV
$^{10}\text{B}(n,\alpha)$	0.0253 eV to 250 keV
$^{10}\text{B}(n,\alpha_1\gamma)$	0.0253 eV to 250 keV
$^{12}\text{C}(n,n)$	0.0253 eV to 1.8 MeV
$^{197}\text{Au}(n,\gamma)$	0.0253 eV, and 0.2 to 2.5 MeV
$^{235}\text{U}(n,f)$	0.0253 eV, and 0.15 to 20 MeV
$^{238}\text{U}(n,f)$	threshold to 20 MeV

To experimentally determine the neutron flux, one must compare the measured reaction yield $Y_{n,x}^{meas}$ with the expected theoretical yield $Y_{n,x}^{th}$. The measured reaction yield is defined as

$$Y_{n,x}^{meas} = \frac{C(E_n) - B(E_n)}{\varepsilon_{n,x} \cdot \phi_n(E_n)}, \quad (2.1)$$

where $C(E_n)$ and $B(E_n)$ are the total and background counts, $\varepsilon_{n,x}$ is the efficiency for detecting the relevant reaction and $\phi_n(E_n)$ is the neutron flux to be determined. The expected theoretical yield, neglecting multiple scattering (i.e. for thin targets) is defined as

$$Y_{n,x}^{th} = (1 - e^{-n\sigma_{n,t}(E_n)}) \frac{\sigma_{n,x}(E_n)}{\sigma_{n,t}(E_n)} \lim_{n\sigma_{n,t} \rightarrow 0} \approx n\sigma_{n,x}(E_n), \quad (2.2)$$

where n is the areal density of the sample in atoms per barn and $\sigma_{n,x}$ and $\sigma_{n,t}$ are the reaction and total cross sections in barns respectively. When measuring a thin sample, self shielding effects become negligible thus this approximation is valid, and one can calculate the neutron flux by combining the two equations

$$\phi_n(E_n) = \frac{C(E_n) - B(E_n)}{\varepsilon_{n,x} \cdot n \cdot \sigma_{n,x}(E_n)}. \quad (2.3)$$

The neutron flux has been determined measuring three standard reaction cross sections as summarised in Table 2.2 by means of four different detection systems. These measurements and corresponding results will briefly be discussed here however for more details see References [3] and [50].

Firstly, the SiMon (**S**ilicon **M**onitors) detectors [51] were used to measure the ${}^6\text{Li}(n,\alpha){}^3\text{H}$ reaction which is a standard between 25 meV and 1 MeV. The uncertainties in the angular distribution of the reaction products limit the use of the SiMon detector to below ~ 150 keV. More information on the SiMon can be found in section 2.2.4.

The MicroMegas (MGAS) detectors [52, 53] were used to measure the ${}^{10}\text{B}(n,\alpha){}^7\text{Li}$ reaction, which is also a standard between 25 meV and 1 MeV. The MGAS detector is a gas detector with two volumes, separated by a thin micromesh. As a charged particle travels through the first volume, in this case the α particle, ionisation occurs within the gas and the produced electrons are multiplied and amplified by an avalanche process in the second volume. However, the detector is also sensitive to protons produced by elastic n-p collisions, and this background limits the energy range of the MGAS to below ~ 150 keV.

The ${}^{235}\text{U}(n,f)$ reaction is a standard at 25 meV and also between 150 keV and

200 MeV and has been measured by three different detection systems at n_TOF. This reaction has also been used to measure the flux above 200 MeV, since there are no standard reaction cross section in this energy range. Firstly, the MGAS (described above) was used to measure the cross section, however it is limited by the γ -flash to measure beneath 10 MeV. Secondly, the detector H19 from PTB (Physikalisch-Technische Bundesanstalt) [54, 55] was used, which consists of an ionisation chamber with 10 ^{235}U deposits, 76 mm in diameter and around $500 \mu\text{g}/\text{cm}^2$ on both sides of five platinum electrodes. This amounts to a total amount of around $201.4 \pm 0.5 \text{ mg } ^{235}\text{U}$. The PTB detector is also limited by the γ -flash to measure below 3 MeV, however the sample masses and efficiencies are very well known allowing a very accurate normalisation to be performed. Finally, the neutron flux has also been measured by the PPAC (Parallel Plate Avalanche Chamber) detectors [56]. They recover very quickly after the gamma flash, allowing data to be taken up to 1 GeV. The PPACs are also used in fission cross section measurements at n_TOF, see for example Reference [56].

Table 2.2: The detectors and reactions used to determine the neutron flux

Detector	Sample and reaction	Areal density($\frac{\mu\text{g}}{\text{cm}^2}$)	E_n where σ_n is standard	Upper E_n limit for detection
PTB	$^{235}\text{U}(\text{n},\text{f})$	500 (10 samples)	25 meV, 0.15-200 MeV	3 MeV
SiMon	$^6\text{Li}(\text{n},\text{t})$	300	25 meV to 1 MeV	150 keV
MGAS	$^{10}\text{B}(\text{n},\alpha)$	55	25 meV to 1 MeV	150 keV
MGAS	$^{235}\text{U}(\text{n},\text{f})$	470	25 meV, 0.15-200 MeV	1 MeV
PPAC	$^{235}\text{U}(\text{n},\text{f})$	279	25 meV, 0.15-200 MeV	1 GeV

This results in different measurements of the neutron flux in different energy regions, and what is required is one overall value for the neutron flux, defined as the *evaluated neutron flux*. This is found by combining the individual measurements and estimating the overall systematic uncertainty by comparing the flux values in energy regions which overlap more than one detector, and taking the Root Mean Square (RMS). All the fluxes are normalised to that measured by the PTB at 25 meV since the associated sample masses and detector efficiency are extremely well known and at this energy all the reactions have a standard cross section. Figure 2.4 shows the evaluated neutron flux for the capture collimator set up with the corresponding statistical and systematic uncertainties, of which tabulated values can be found in Table 2.3.. At high neutron energies (MeV range), we

see peaks corresponding to knock on nuclear reactions found in the typical neutron evaporation spectrum, which can be partially moderated as is seen in the intermediate energy region which follows an isoethargic distribution. At low energies, we find thermalised neutrons, and it is this region of the flux that is reduced significantly when borated water is used as a moderator instead of water due to the high $^{10}\text{B}(n,\alpha)$ cross section. Structures are seen within the flux corresponding to transmission dips from the resonances in ^{27}Al , ^{55}Mn and ^{113}Cd which are present in the beam line, which can limit the accuracy in cross section measurements in certain neutron energy regions.

Overall, the flux is determined within 1% uncertainty between thermal and 100 eV, 2% between 100 eV and 10 keV, 3-4% between 10 keV and 1 MeV and 2-3% between 1 and 200 MeV. Above 200 MeV, there are no standard cross sections therefore the statistical uncertainty is used in this region, which is between 3 and 4%. Importantly, the accuracy of the neutron flux within the energy region of this work (<20 keV) sets the lower limit on the accuracy that can be reached within this measurement: 1% below 100 eV and 2% between 0.1 and 20 keV.

Table 2.3: Integrated number of neutrons per nominal proton pulse (7×10^2 protons) in each energy decade corresponding to the capture set up with borated water as a moderator.

Neutron energy	Neutrons/Pulse	Statistical	Systematic
10-100 meV	1.5×10^4	2.0%	1.0%
0.1-10 eV	1.3×10^4	2.0%	1.0%
1-10 eV	2.0×10^4	2.0%	1.0%
10-100 eV	2.5×10^4	1.4%	1.0%
0.1-1 keV	2.9×10^4	1.4%	2.0%
1-10 keV	3.2×10^4	1.3%	2.0%
10-100 keV	4.4×10^4	1.3%	3.0 - 4.0%
0.1-1 MeV	1.3×10^5	0.9%	3.0 - 4.0%
1-10 MeV	1.5×10^5	0.9%	2.0 - 3.0%
10-100 MeV	5.0×10^4	2.0%	2.0 - 3.0%
0.1-1 GeV	4.7×10^4	2.0%	-
0.1 - 100 keV	1.63×10^5	1.3 - 2.0%	1.0 - 4.0%

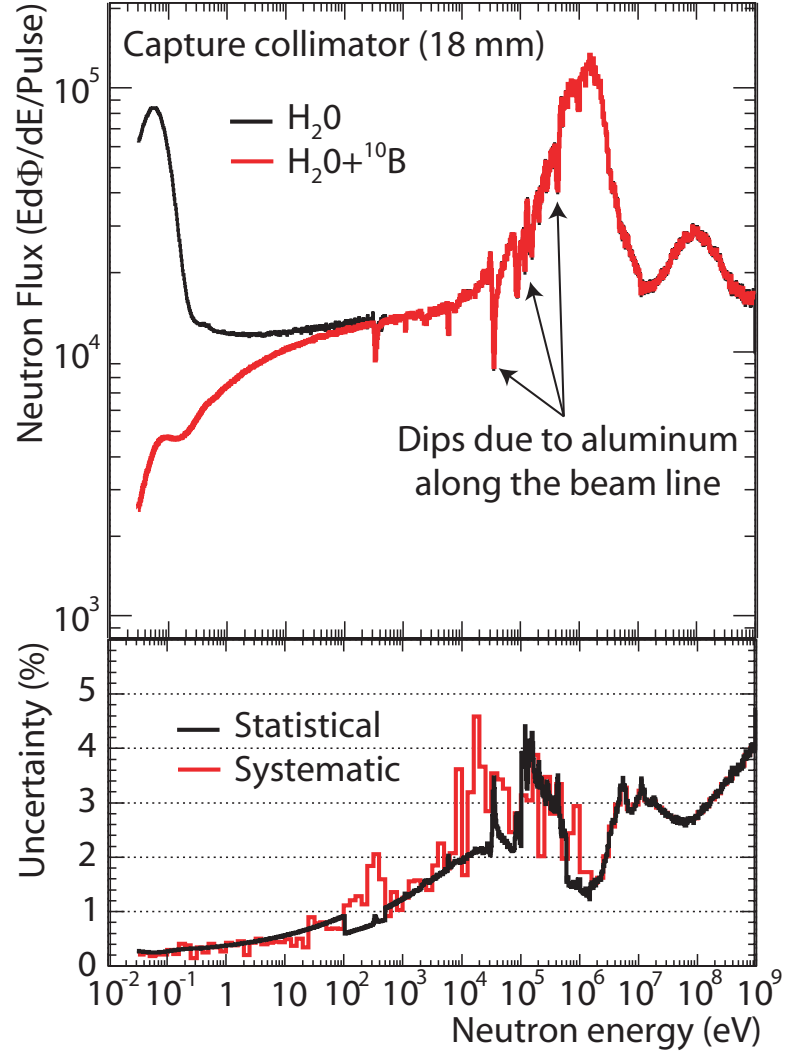


Figure 2.4: The n_TOF evaluated neutron flux with and without borated water as a moderator and the corresponding uncertainties [3].

2.2.2 Neutron beam profile

The spatial profile of the beam plays an important role in a capture cross section measurement as it is vital to accurately know what proportion of the beam the sample being measured covers (the beam interception factor N_{BIF}). In this particular measurement, the samples have been chosen to be approximately the same size as the beam reducing any uncertainties introduced in calculating N_{BIF} . The spatial profile of the beam is determined mainly by the second collimator and it also changes with neutron energy due to the different moderation paths neutrons of different energies follow after being produced within the lead target. This profile has been measured using a 5 cm diameter 2D pixelated MicroMegas (pixel-MGAS) detector [57] which has 308 square pixels of 2.5 mm side length. Furthermore, the beam profile has been simulated using FLUKA [58]. Figure 2.5

shows the expected profile from simulations for the two available collimator diameters and the experimental results with the capture (18 mm in diameter) set up. The agreement between data and simulations is excellent except in the tails, where the measurement is affected by background.

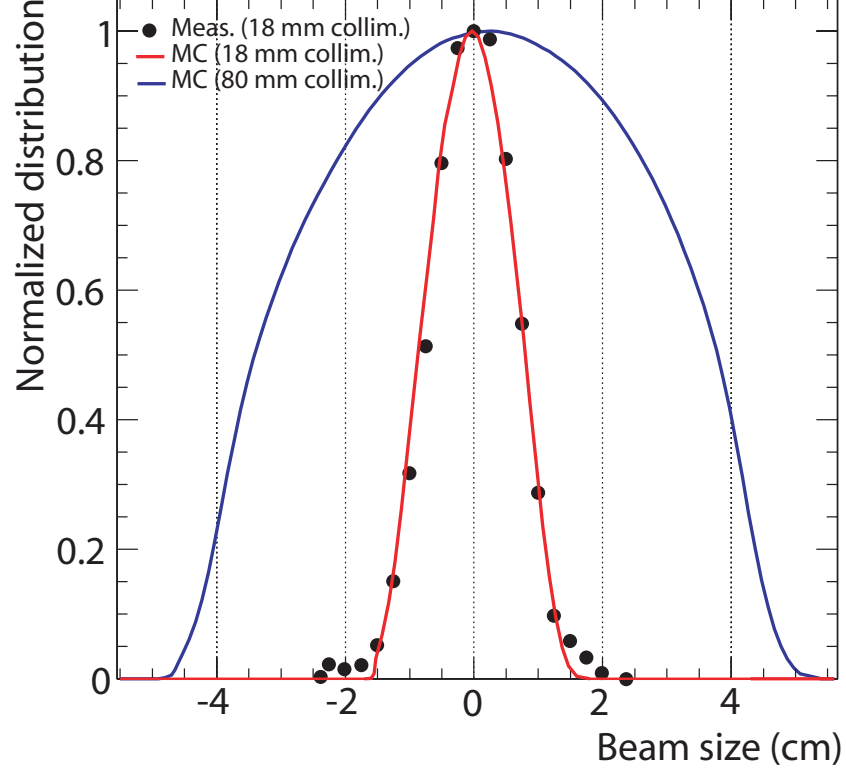


Figure 2.5: The n_TOF beam profile, measured and simulated (for two different collimators) [3].

The neutron beam has an approximately gaussian shape, with a full width at tenth maximum of ~ 3.0 cm for capture mode with $\sigma \sim 0.7$ cm. Many previous capture measurements used samples of only 1 cm diameter, intercepting less than 20% of the beam, whereas the present samples (see Section 2.4.1) cover more than 95% of the beam. In this way, we reduce any uncertainty from calculating the fraction of the beam the samples intercept over all neutron energies.

2.2.3 Neutron energy resolution

To measure a neutron capture cross section in the resolved resonance region, excellent neutron energy resolution must be available to allow neighbouring resonances to be individually resolved. The spread of neutrons of a certain energy ($\Delta E/E$) arises from three main points:

1. The proton pulse width (7 ns RMS).

2. The uncertainty in the neutron flight path L :

- The uncertainty on the distance between the spallation target and the sample.
- The uncertainty on the moderation distance (described by the Resolution Function).
- The uncertainty due to the Doppler effect. The Free Gas Model (FGM) is a good approximation of the thermal broadening which results in a Gaussian broadening of the resonances with a standard deviation:

$$\sigma_D = \sqrt{\frac{2k_b T}{M/m} \cdot E_n}, \quad (2.4)$$

where M/m is the ratio of the masses of the target nucleus and the incident particle.

3. The uncertainty due to the detectors response.

In the case of the ^{238}U measurement with the TAC, the uncertainty in the the detector response time and the absolute flight path determination is negligible (see Chapter 3 and Section 4.1 respectively) and the remaining contributions to the neutron energy uncertainty are displayed in Figure 2.6.

As can be seen from Figure 2.6 the two dominating components to $\Delta E/E$ are Doppler broadening and the Resolution Function and the characteristics of the n_TOF facility allow ^{238}U resonances to be resolved up to the current limit of the Resolved Resonance Region, 20 keV. The uncertainty due to the Doppler effect arises due to the fact that the target nuclei have a distribution of kinetic energies corresponding to their temperature which broadens the resonances. The uncertainty due to the Resolution Function takes into account the spread in measured time for neutrons of the same kinetic energy due to neutrons taking different moderation paths between the target and the experimental area. This resolution is customarily thought of in terms of equivalent travelled distance, but can also be thought of as a change in the neutron time-of-flight or a change in the neutron kinetic energy.

$$R_t(\delta t)d\delta t = R_L(\delta L)d\delta L = R_E(\delta E)d\delta E. \quad (2.5)$$

The Resolution Function ($R_E(E_n)$) is determined through Monte Carlo simulations of the neutron beam and subsequently validated against experimental data for well known resonances. This was done using the code FLUKA [58], developed at CERN. In the past, the Resolution Function was described analytically, with

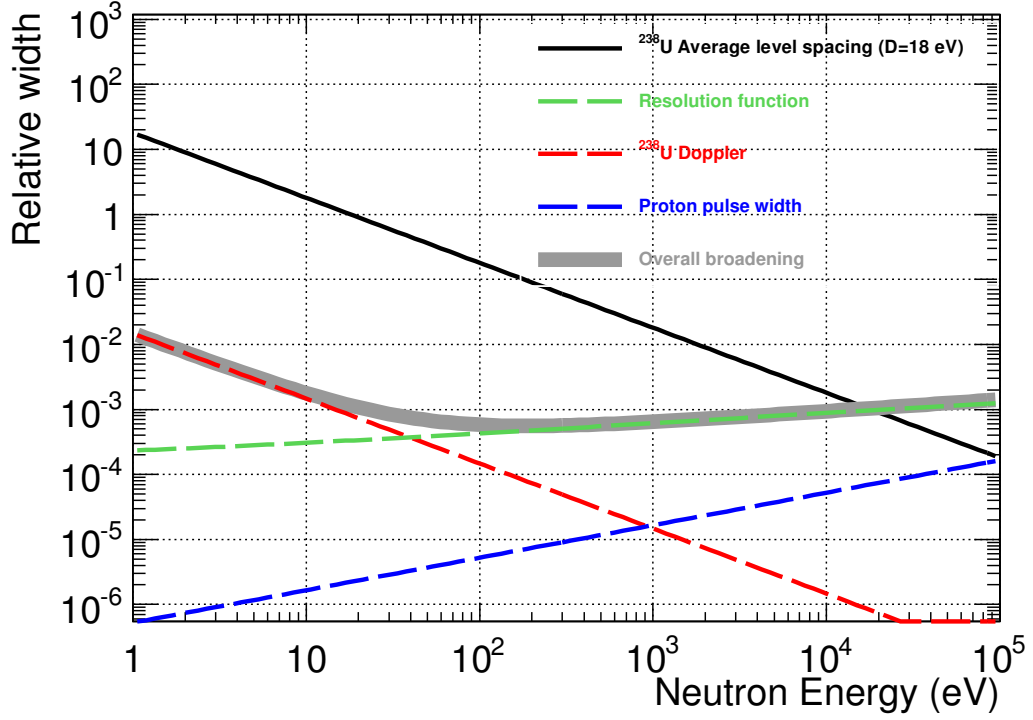


Figure 2.6: The different effects that cause experimental resonance broadening. The total broadening is shown alongside the average spacing between resonances.

an energy dependence inside the function with two different representations; one based on the equivalent neutron distance, the other based on the equivalent neutron time [59]. Recently, a numerical Resolution Function has been developed, again based on FLUKA simulations, which is advantageous as it allows a more accurate description of the overall broadening. The Resolution Function not only broadens the resonances, but also introduces an asymmetric shape. Therefore to accurately determine the properties of a resonance size this quantity must be correctly known. Figure 2.7 demonstrates the expected shape of a ^{238}U resonance taking the resonance parameters from JEFF-3.1.2 with and without Resolution Function broadening effects alongside experimental data (see Chapter 4 for more information).

In the energy range of interest, both Doppler broadening and the Resolution Function effect the resonances. As is demonstrated in figure 2.7, the resonance shape is correctly reproduced when applying the Resolution Function, therefore in the analysis we can determine not just the resonance areas (defined through the *resonance kernel*) but also the shape.

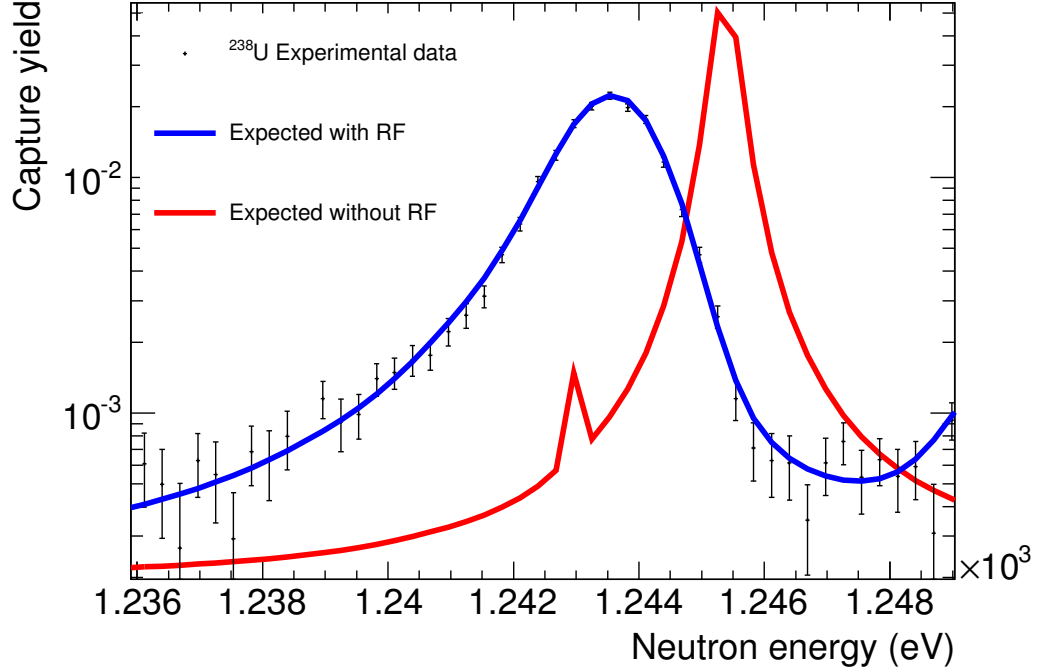


Figure 2.7: A demonstration of the expected ^{238}U resonance shape using the code SAMMY with and without the Resolution Function alongside experimental data.

2.2.4 Neutron beam monitors

During the experimental campaign, both the proton and neutron beam intensities are continuously monitored. In normal circumstances the neutron beam intensity should be proportional to that of the proton beam; however this proportionality must be checked because closed vacuum valves, changes in the moderator temperature or the aperture of the proton beam could affect this proportionality. Firstly, the Wall Current Monitor (PKUP) detector relays the intensity of each proton pulse. Secondly, the intensity of the neutron beam is monitored by the SiMon detectors (**Silicon Monitors**) [51] which measure the $^6\text{Li}(n,\alpha)^3\text{H}$ reaction. A thin Mylar foil with a thin deposit of ^6Li is inserted in the beam, and the subsequent alpha and triton particles produced in the reaction are detected by silicon detectors placed outside the beam.

Both the proton and neutron intensities are measured for monitoring purposes and part of the analysis process consists of, as discussed in Section 2.4.3, investigating the mentioned proportionality on a run by run basis.

2.2.5 Data acquisition system (DAQ)

The data acquisition system (DAQ) at n_TOF [60] must support very fast data transfer rates, a large memory buffer and a dead-time free system to maximally benefit from the high instantaneous neutron flux. Rather than an analog based system, where data are initially manipulated on the fly before being stored, the DAQ at n_TOF is based on high performance flash-ADC digitisers, which directly digitise and store the signals (raw data), allowing a dedicated off line analysis to take place. This means any problems in the raw data, such as pile-up, baseline shifts and threshold levels can be optimally dealt with using dedicated pulse shape analysis routines for each detector. Furthermore, most of the front-end electronics such as preamplifiers and time and energy amplifiers are not required since the data processing can be totally done using software. The taking of such vast amounts of data comes with its problems; namely data storage and data transfer rates.

When a pulse of protons is incident on the lead target, the DAQ receives a trigger, which opens a 32 ms time window for which the DAQ is taking data. The 32 ms in neutron time-of-flight corresponds to 0.3 eV, which is thus the lowest neutron energy for which the cross section can be measured. During these 32 ms, all detector outputs are digitised at a sampling rate of 250 MSamples/s by 8-bit flash-ADCs. This large amount of data then undergoes a “zero” suppression algorithm on the fly which takes only signals above a certain threshold. These data sets simply contain header files (giving information such as date, run number) and the digitised data with time stamps, in binary format. This is then formatted in a data buffer, and typically four data buffers are grouped into a data stream. These data stream files are then stored temporarily in a local temporary disk pool with a maximum size of 2 Gb. Once this file size limit is reached, it is transferred via GigaBit ethernet to the **C**ern **A**dvanced **S**TORage manager (CASTOR) [61], where it is stored on both disk and tape. Dedicated pulse shape analysis routines have been developed for analysing the raw data from each detector which transforms the digitised “movies” into a list of signals with their corresponding time-of-flight, amplitude and area. An example of a digitised movie and the associated pulse shape analysis is given in the following section for the particular case of the Total Absorption Calorimeter detector.

2.3 The n_TOF Total Absorption Calorimeter (TAC)

The **T**otal **A**bsorption **C**alorimeter (TAC) [4] is a segmented array of 40 BaF₂ crystals, designed to detect the complete γ -ray cascade emitted during a neutron capture reaction. It is based on a previous BaF₂ calorimeter at FZK [62] and is suited for capture cross section measurements due to the TAC's high solid angle coverage and high intrinsic detection efficiency. The 40 crystals are composed of 12 pentagonal and 28 hexagonal BaF₂ crystals of 15 cm thickness which fit together as a hollow sphere with an inner radius of 10 cm covering 95% 4π solid angle. Each individual crystal is surrounded by two layers of 0.1 mm thick Teflon foil and a 0.1 mm thick polished aluminium sheet to optimise light collection. Furthermore, the crystals are encased by a protective layer of ¹⁰B enriched carbon fiber which has the purpose of absorbing neutrons so they don't reach the crystals. The crystals are all supported by an aluminium honeycomb structure, which is split into two hemispheres that can be separated allowing access to the centre of the TAC.

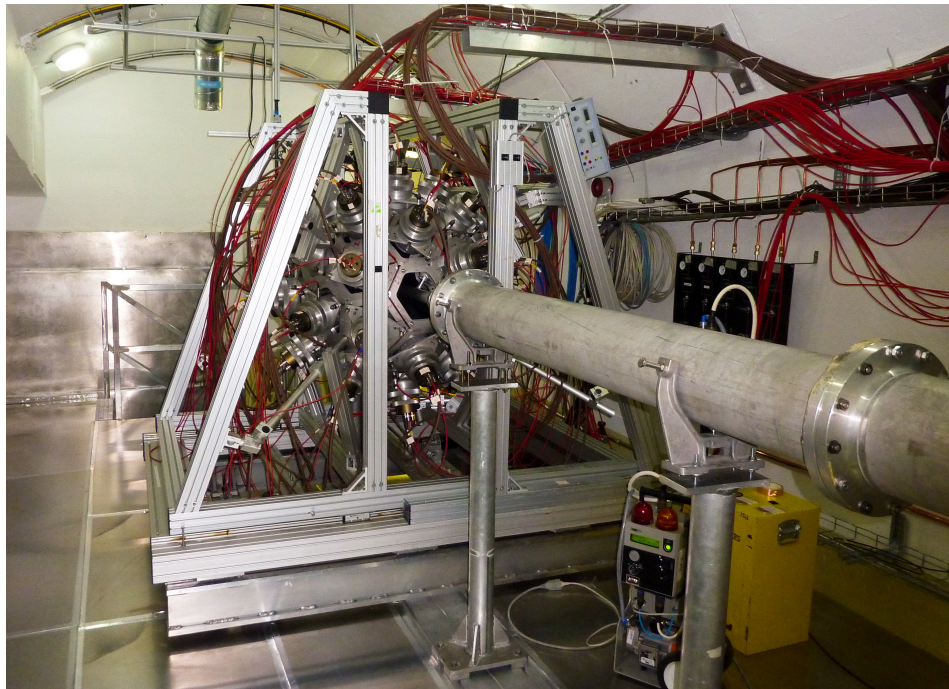


Figure 2.8: The TAC in the experimental area.

For time-of-flight measurements, using an array of BaF₂ crystals is advantageous for three main reasons:

- Fast timing properties: the 0.6 ns fast component (τ_{fast}) reduces the uncertainty in the neutron detection time (δt_{det}).

- Good energy resolution: Typically $\sim 13\%$ at 1 MeV which allows one to distinguish between different reactions according to their Q-values.
- High total absorption efficiency: By detecting the energy of the whole capture cascade one obtains powerful background rejection capabilities.

However, the use of a calorimeter such as the TAC for neutron time-of-flight measurements also has limitations. Firstly, the fast component takes only around 20% of the light output, the remaining arriving as the slow component with a decay time of 630 ns which is caused by delayed fluorescence and phosphorescence. It can be that a second signal is sitting on top of a previous one (pile-up) and is thus difficult to identify (dead-time). An intrinsic background is present due to radium impurities (^{226}Ra) within the crystals, which give rise to a sizeable level of α and β signals. Signals produced by α -particles lack a fast component, therefore can be discriminated by pulse shape analysis. The second limitation is that from the *neutron sensitivity*, that is the probability of detecting scattered neutrons within the TAC (see Section 3.2.3 for details). Due to the sizeable capture cross section of barium, the probability of detecting scattered neutrons is much higher within the TAC compared to for example C_6D_6 detectors. In order to minimise the probability of detecting neutrons scattered in the sample and subsequently being captured in the TAC, the hollow space between the sample and the BaF_2 crystals is filled with a borated polyethylene neutron absorber. The neutron absorber material was carefully selected using Monte Carlo simulations [63] to find the best material for moderating/absorbing neutrons whilst minimally attenuating the γ -rays. The most suitable material was found to be ^6LiH , however this was not a possibility due to its flammable nature. Therefore, an inert non-flammable borated polyethylene (enriched to 5% of ^{10}B) was used, as can be seen in figure 2.9.

The signals are analysed with a dedicated pulse shape analysis routine [64], which fits the two scintillation components separately, fitting a Lorentzian to the fast component ($\tau_{fast}=0.6$ ns), and an exponential decay to the slow component ($\tau_{slow}=630$ ns). An example of several fits to BaF_2 signals is illustrated in Figure 2.10.

The signals from all individual detectors are grouped into TAC events using a coincidence window of 20 ns after the first signal. Each TAC event is characterised by its time-of-flight (that of the first signal in the event), the sum energy of all the signals involved (deposited energy E_{sum}) and the number of BaF_2 crystals involved in the event (multiplicity m_{cr}). The good energy resolution, high segmentation and high absorption efficiency of the TAC allows identifying and rejecting background events by applying analysis conditions in m_{cr} and E_{sum} , as will be discussed in

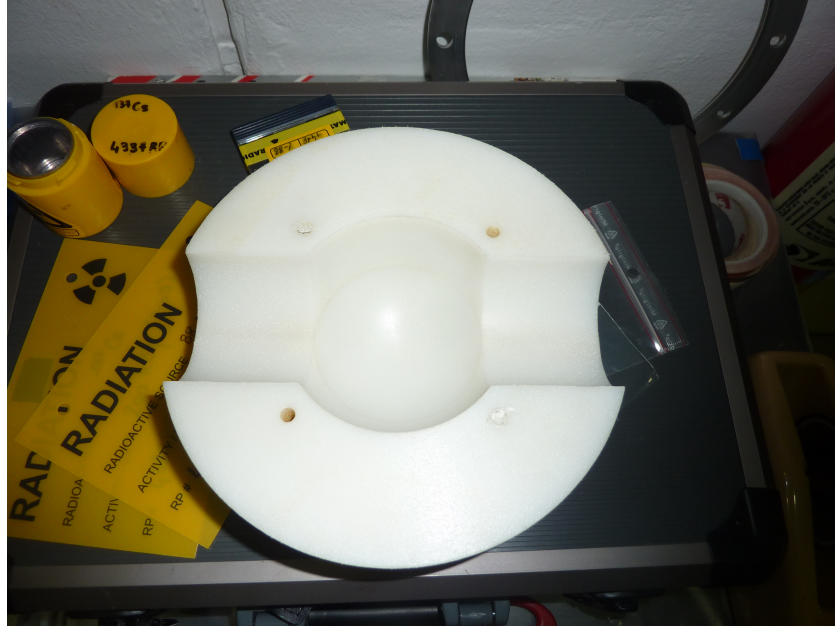


Figure 2.9: One hemisphere of the borated polyethylene neutron absorber used during the campaign to reduce the background from scattered neutrons.

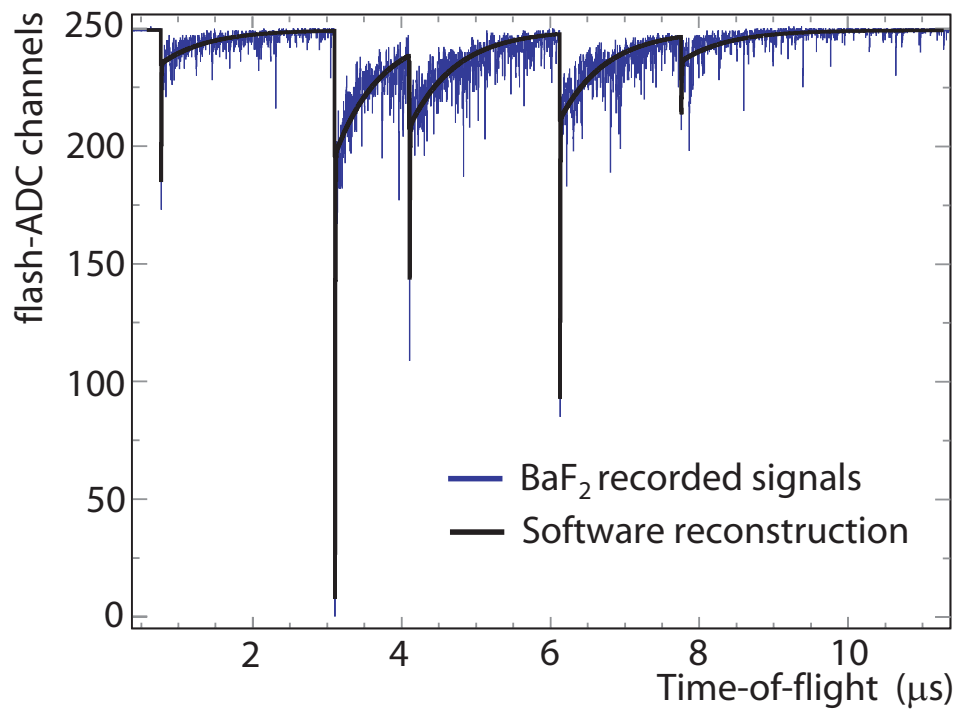


Figure 2.10: Digitised signals from the TAC (blue) and the reconstruction by the PSA routine (black)[4].

Chapter 3.

The TAC has been used extensively within n_TOF's history to make capture cross section measurements of the minor actinides (^{237}Np [65], $^{233,236}\text{U}$ [66, 67], ^{240}Pu [68], $^{241,243}\text{Am}$ [69]) and also to delve into fundamental nuclear structure

(level densities [70] and photon strength functions [71]), however there are many individualities to each measurement, therefore the analysis may follow a slightly different procedure than that used in previous measurements.

2.4 Experimental campaign

The capture cross section measurement of ^{238}U with the TAC started on the 15th September 2011 and ran for a total of 35 days. Beam was taken 24 hours a day whilst someone was on shift allowing online variables to be monitored and checked, for example detector voltage, vacuum levels, magnet current and proton beam intensity. Energy calibrations of the TAC crystals were performed on a weekly basis to monitor any shifts in detectors' gains (see section 3.1.3 for more information). As well as measuring ^{238}U , it was necessary to also measure a natural carbon sample, take measurements without any sample and, finally, in the absence of beam both with and without the ^{238}U sample in place. The carbon measurement is performed because carbon is considered a pure neutron scatterer so is used to characterise the neutron scattering background (see Section 3.2.3). Finally, the sample out and beam-off measurements allow one to study the backgrounds not related to the sample and the beam respectively. Table 2.4 summarises all the measurements performed and the time spent on each one.

Table 2.4: Details of time allocation to each particular sample configuration.

Sample	# Protons	Running time
^{238}U	$1.12 \cdot 10^{17}$	24.7 days \sim 70.5%
Sample out	$1.05 \cdot 10^{17}$	6.6 days \sim 19%
$^{\text{nat}}\text{C}$	$7.05 \cdot 10^{16}$	2.7 days \sim 7.5%
Beam-off (with ^{238}U)	-	0.6 days \sim 2%
Beam-off (without ^{238}U)	-	0.3 days \sim 1%
Total	$2.96 \cdot 10^{17}$	34.9 days

2.4.1 Samples

The ^{238}U sample was provided by the EC-JRC-IRMM [23], where an isotopic analysis was performed in 1984. It is an extremely pure (99.999%) 6.125(2) grams sample which contains <1 ppm of ^{234}U , ~ 11 ppm of ^{235}U and <1 ppm of ^{236}U . Furthermore, it was accurately weighed after transportation to CERN.

It is a wide, approximately rectangular sample ($\sim 53.90 \times 30.30$ mm), which with perfect alignment covers 97% of the n_TOF neutron beam and in order to comply with radioprotection regulations, the sample was encased in ~ 60 microns

of aluminium foil and ~ 75 microns Kapton. Details of the two samples used throughout the measurement are summarised in table 2.5.

Table 2.5: Details of the samples used during the experimental campaign

Sample	Size (mm ²)	Mass (g)	Areal density (Atoms/barn)
²³⁸ U	1621.22 \pm 0.05 (53.90 \times 30.30 mm)	6.125 \pm 0.002	(9.56 \pm 0.05) $\times 10^{-4}$
natC	1635.18 \pm 0.65 (53.35 \times 30.65 mm)	14.638 \pm 0.002	(44.9 \pm 0.05) $\times 10^{-3}$

The samples are more massive than habitually used with the TAC at n_TOF. They thus have the advantage that the count rate is very high, allowing good statistics to be reached and a better capture to background ratio; however the high count rate leads to sizable dead-time and pile-up effects in the data which must be minimised as much as possible (see Section 2.4.2) and then corrected for (see Sections 3.1.6 and 4.1.2).

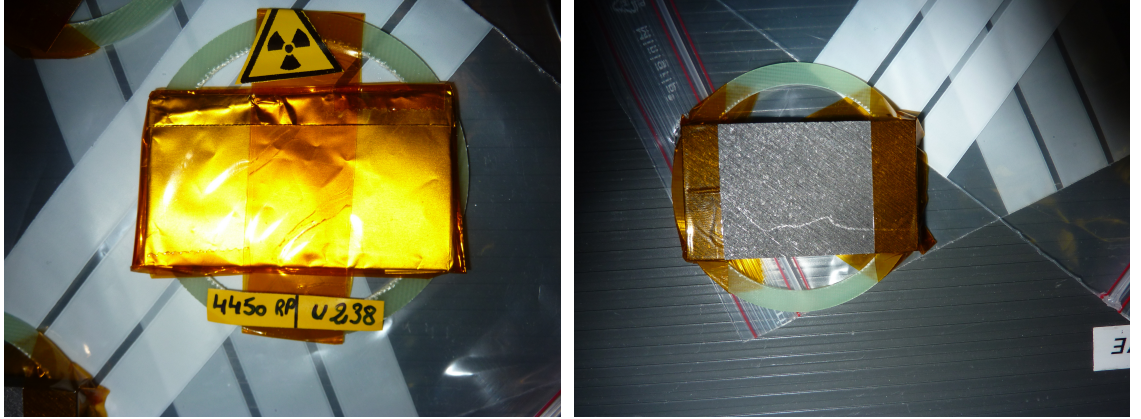


Figure 2.11: The samples used within the campaign: ²³⁸U (left) and natC (right).

2.4.2 Beam intensity

The normal operation at n_TOF consists of two different pulsed beam intensities: a dedicated TOF beam of 8×10^{12} ppp (protons per pulse) and a parasitic EAST beam of 3×10^{12} ppp. However, due to the large count rates associated to the massive samples, the beam intensity was reduced for this specific measurement to avoid too much pile-up in the TAC. As shown in Figure 2.12, data were taken with two different beam intensities: LOW ($\sim 0.5 \times 10^{12}$ ppp) and MED ($\sim 1.0 \times 10^{12}$ ppp). The data were also taken at higher intensities to investigate the effect of the γ -flash (see section 4.1.3), but the corresponding data were not used due to the high count rates.

Furthermore, the use of two different beam intensities has allowed us to compare the two data sets after correcting for dead-time and pile-up and thus make sure

that the correction methods are accurate (see Section 4.1.2).

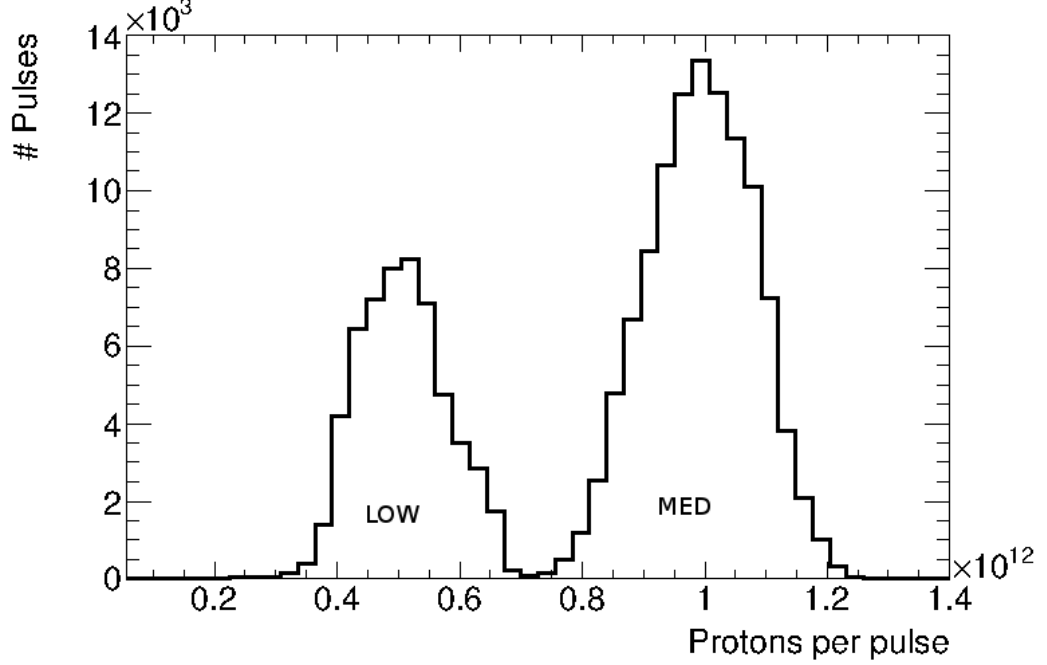


Figure 2.12: Proton beam intensity distribution for LOW and MED pulses.

2.4.3 Proportionality between detection systems

Although the experiment is monitored in real time during the running period, these data must be still be accurately checked after the experiment before being used in the final analysis. This is done by performing so called *quality checks*, which aim to systematically confirm that each detector in use was performing correctly. For each proton/neutron pulse, there are four detection systems, and the number of counts relative to each other should follow the same proportionality over the whole campaign. Firstly, the proton beam is monitored by two different detection systems; the variable “Pulse Intensity” is given from the CERN accelerator complex (in this case the Proton Synchrotron (PS)) and the PKUP is a detector operated by n_TOF which measures the intensity of the proton pulse just before the lead spallation target. Secondly, the neutron beam is monitored by the SiMon detection system, as explained in section 2.2.4. Finally, the γ -rays from (n,γ) reactions in the sample are detected in the TAC.

Firstly, we must define what we measure as true counts from each detector. For the proton detectors, this is simple as the value of the Pulse Intensity is given through the PS and the PKUP value is given by the full integral of the signal.

The SiMon detection system measures the reaction ${}^6\text{Li}(n,t){}^4\text{He}$ and it is possible to see both the triton and the α -particle in the spectrum. Figure 2.13 shows the amplitude spectrum for one of the four silicon detectors, in the neutron energy range 1 eV to 10 keV. The triton peak can clearly be seen between the two dashed lines, therefore by gating in this region for all four detectors we obtain an accurate representation of the number of neutrons in the beam.

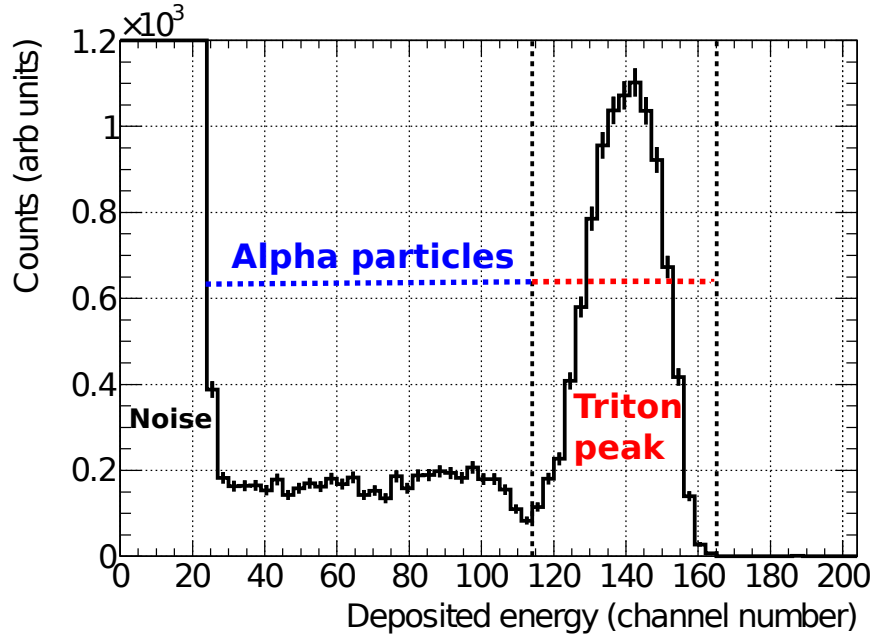


Figure 2.13: Silicon detector amplitude spectrum; the triton peak distinctly falls between the two dashed vertical lines.

Finally, we must quantify the number of capture events detected in the TAC. As will be shown in chapter 4, by imposing conditions on the measured multiplicity (m_{cr}) and deposited energy E_{sum} within the TAC of $m_{cr} > 2$ and $2.5 < E_{sum}(\text{MeV}) < 5.75$ one has an accurate numerical representation of the capture events in the TAC. For each run we calculate two different values for the number of protons, one value for the number of neutrons and one value for the number of capture events. The ratios of these four quantities should remain constant over time for each different measurement, therefore any major differences will flag up problems. The ratios have been calculated for each run during the campaign, and the coefficient of variation ($CV = \sigma/\mu$) quantifies the level of agreement between different detection systems.

From table 2.6 we find a very good agreement of the measurement of protons between the PKUP and Pulse Intensity, giving confidence that these detectors were stable during the whole campaign. However, it is seen that comparing any detector

Table 2.6: Ratios of counts between detectors used during the ^{238}U runs.

Detector ratio	Coefficient of variation
PKUP/Pulse Intensity	0.53
SiMon/Pulse Intensity	10.02
TAC/PKUP	0.97
TAC/Pulse Intensity	1.35

with the silicon detectors gives a poor agreement of around 10%. Unfortunately, this means the SiMon detection system was not stable during the experimental campaign, therefore it cannot be used as an accurate neutron monitor. However, it is seen that the PKUP and measured TAC counts agree within 1%, therefore the PKUP can be used to normalise measured counts. A small number of runs ($\sim 3\%$ corresponding to $<1\%$ of total neutrons) have detector count ratios differing by more than three σ from the mean, and these runs (outliers) have been discounted from the analysis. The loss in statistics is negligible whereas we can be confident we are only using data in the final analysis where all the detectors were working correctly.

CHAPTER 3

Operation and performance of the TAC

This chapter aims to build on the description given of the TAC in Section 2.3, documenting and showcasing the calorimeter’s qualities and capabilities. The TAC has been used for cross section measurements at n_TOF previously, however each measurement utilises the calorimeter in the most advantageous way, therefore a detailed analysis of the detector properties is presented for this specific measurement.

3.1 Event building: from BaF₂ signals to TAC events

The Total Absorption Calorimeter (TAC) is a complex detection system comprised of 40 individual BaF₂ crystals, each of which provide one input into the DAQ which are then stored on disk and tape for analysis. The event building consists of transforming these individual signals into something more useful to utilise the calorimeter’s capabilities best and allow an accurate cross section to be measured.

3.1.1 Pulse shape analysis for BaF₂ signals

The first stage of the TAC analysis is to perform a pulse shape analysis (PSA) of each individual detector’s data. This process was introduced in Section 2.3 and example BaF₂ signals with their corresponding fits can be seen in Figure 2.10. Details on the PSA process can be found in Reference [64]. The goal of this process is to identify the signals in the data buffer and analyse each of them providing a total amplitude value (giving the energy of the γ -ray), a time stamp at which

the signal was produced (giving the time-of-flight value) and finally identification of the incident particle to discriminate between γ -rays and α -particles. This is performed by, after noise rejection, fitting the two BaF₂ scintillation components (fast and slow) with a Lorentzian and an exponential, respectively. The time of the signal is given by the fast component whilst the integral is calculated from the slow component. The signals from the Ra contaminants in the crystals do not feature the fast component and thus the ratio of fast to slow component integrals allow the identification and elimination of the the alpha signals.

The TAC was first mounted and commissioned in 2004 and although the crystal's scintillation properties will not have changed over time, other properties such as the optical coupling of the PMT may have changed. This is apparent if one looks at the deposited energy spectra for calibration sources from previous and current TAC measurements, where a clear degradation in detector energy resolution is observed. Many iterative alterations on the PSA routine were performed over the original algorithm from 2004 in order to optimise its performance, such as changing the decay constants used to fit the signals. However, the best improvement was found by altering a parameter in the code, α , which sets the signal/background rejection level. The routine works out the root mean squared (RMS) of the noise level, and then originally triggered at 2.5 times over this level. By triggering at five times over this level, the routine was found to show much improved results. Figure 3.1 shows the response of a single BaF₂ crystal to an AmBe source that emits a single γ -ray of 4.440 MeV. The two spectra correspond to results from the original (red) and optimised (black) PSA routine.

The 4.440 MeV single γ -ray produced can cause pair production, and the resulting positron will undergo annihilation producing a further two 511 keV γ -rays. If one of these γ -rays escapes undetected but the remaining energy from the decay is deposited within the detector, a peak appears at 511 keV beneath the photopeak (single escape peak). If a detectors resolution is sufficiently broad, the single escape peak is obscured by the proximity of the photopeak, which was the case for the AmBe spectra with the original (red) PSA routine. The visibility of the single escape peak in the optimised (red) PSA routine clearly illustrates the improvements in resolution.

This PSA routine has been applied to data from each BaF₂ module and the following parameters have been extracted: signal integral (used for the energy calibration), time (used for the time-of-flight and thus for the subsequent neutron energy calibration) and particle type (used to differentiate α background signals from the γ -ray signals of interest).

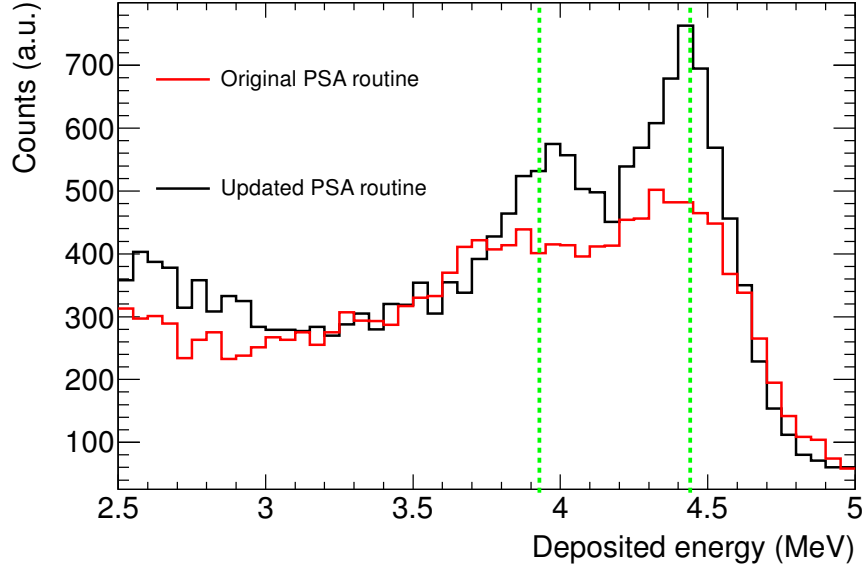


Figure 3.1: AmBe spectra for an individual BaF₂ crystal for two versions of the PSA routine. The two dashed lines represent the photopeak energy (4.440 MeV) and the single escape peak energy (3.929 MeV).

3.1.2 Digitiser's timing calibration

Each of the 40 crystals must be accurately calibrated in time for coincidence and time-of-flight measurements to be performed. The signals from the 40 detectors input into 10 different flash-ADC modules which each contain its own internal clock. These clocks are accurate within 2 ppm, which may seem more than adequate, however this actually means that deviations as large as 64 ns appear from clock to clock along the 32 ms acquisition time following each incident neutron pulse.

To calibrate the ten digitisers in time, a ⁸⁸Y calibration source was used. Figure 3.2 shows the relevant decay scheme, where ⁸⁸Y mostly decays via electron capture almost always producing two γ -rays within <1 ps, which can be considered instantaneous to the TAC.

By gating one γ -ray in a reference detector and looking for the second elsewhere within the TAC, all the detectors can be calibrated in time. Figure 3.3 shows examples of the calibrations, plotting the detection time, τ_{first} , of the first γ -ray in the reference detector against the detection time difference of the second γ -ray: $\Delta t = \tau_{first} - \tau_{second}$.

Using this method, all the clocks are calibrated to within a few ns, resulting in an uncertainty from the flash-ADC comparable to that due to the signal time-of-flight. This accuracy will affect the size of the coincidence window chosen (see Section 3.1.4 and the probability of event pile-up (see Section 3.1.6).

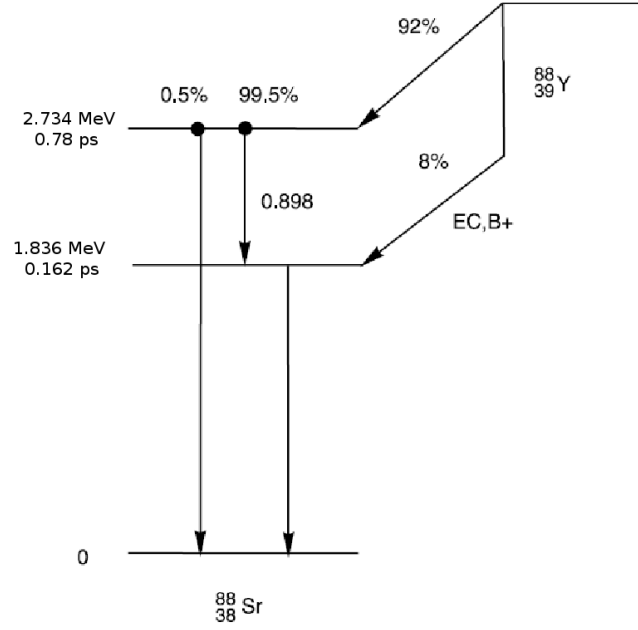


Figure 3.2: ^{88}Y decay scheme highlighting the two γ -rays used for the timing calibration.

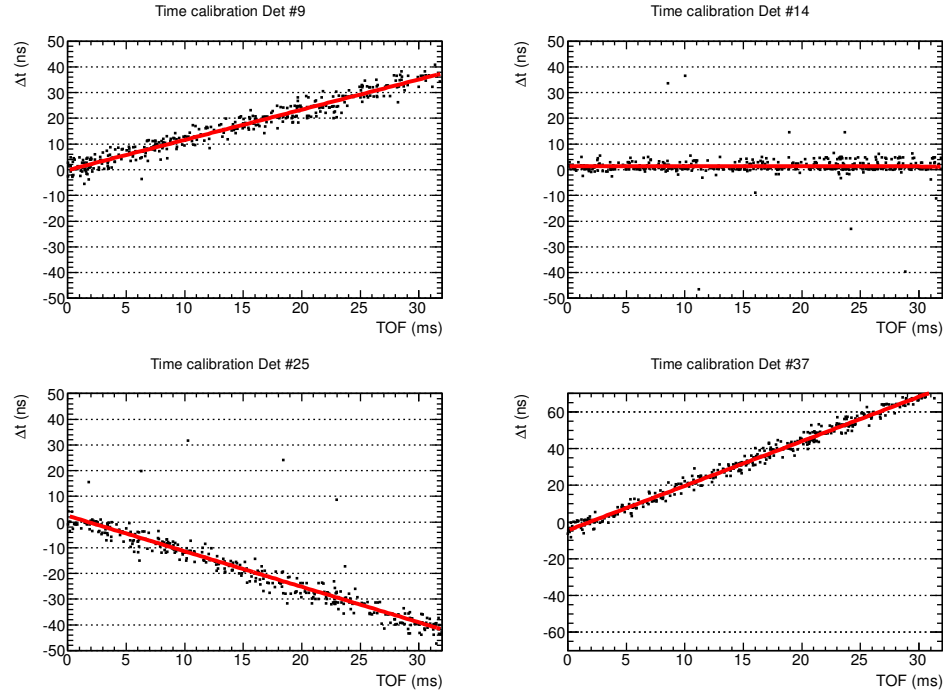


Figure 3.3: Linear time calibration fits for four example flash-ADC modules which exhibit different internal clocks. Detector #14 (top right) is from the same module as the reference detector so is already synchronised.

3.1.3 Deposited energy calibration

As will become apparent, an accurate energy calibration for each detector within the TAC is vital for detecting capture cascades and discriminating from backgrounds. Energy calibrations were performed on at least a weekly basis with four different energy points with the neutron absorber in place, as it is during the experiment. The four energy points correspond to three calibration sources: ¹³⁷Cs (0.661 MeV), ⁸⁸Y (0.898 MeV, 1.836 MeV) and AmBe (4.44 MeV). The individual detectors amplitude spectra were then analysed using the software package ROOT [72] which allowed the background to be stripped and the photo-peak to be fitted with a Gaussian:

$$f(x) = Ae^{\frac{-(x-\mu)^2}{2\sigma^2}}, \quad (3.1)$$

where the amplitude is given by A and μ is the mean value corresponding to the energy of the γ -ray. The detectors resolution can be expressed in absolute (ΔE) or relative ($\Delta E/E$) terms being given by the full width at half maximum:

$$\Delta E = FWHM = 2\sqrt{2\ln 2}\sigma = 2.35482\sigma. \quad (3.2)$$

Figure 3.4 shows the amplitude spectra from one BaF₂ detector corresponding to the three calibration sources and example Gaussian fits to the photo-peaks. The spread of γ -ray energies used for calibration is key, as one sees in the bottom right panel of 3.4 just taking the first three energy points and extrapolating from 1.836 MeV up to ~ 5 MeV can be inaccurate. The inclusion of a high energy γ -ray energy point results in a much more accurate calibration as demonstrated by the difference between the blue and green lines. Some detectors demonstrated a non linear response, therefore a second order polynomial was used to provide an accurate calibration valid for high γ -ray energies for each individual detector.

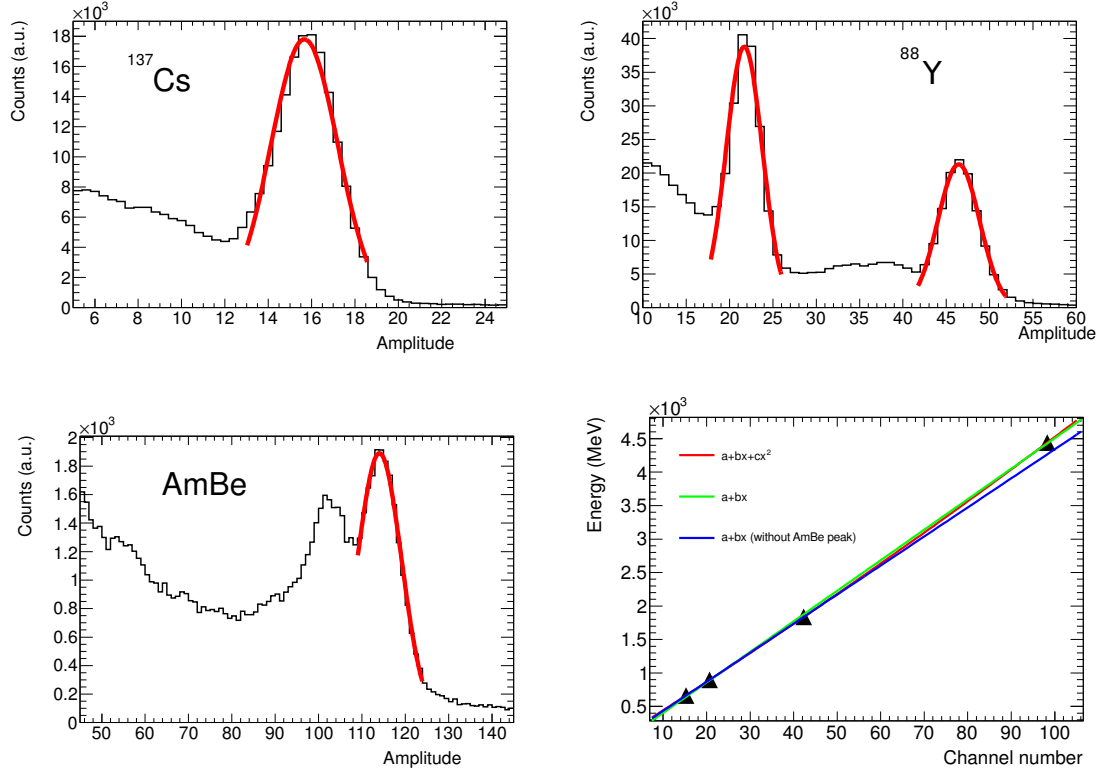


Figure 3.4: Three amplitude spectra from detector #35 corresponding to ^{137}Cs (top left), ^{88}Y (top right) and AmBe (bottom left) with the Gaussian fits shown in red. Example fits to the four energy points are shown in the bottom right.

The gain of each detector may change during the two months of measurements. These gain changes can be monitored on a weekly basis using the calibration points, or on a daily basis using the position of the known α -peaks in the amplitude spectra. However, Figure 3.5 demonstrates that the detectors were stable within one channel throughout the whole of the experimental campaign, corresponding to approximately a 50 keV shift which can be considered negligible.

Figure 3.6 shows the individual crystal resolutions for the ^{137}C and ^{88}Y calibration sources illustrating a vast variation in energy resolution between the detectors. When the TAC was first constructed, the average crystal resolution for the ^{137}Cs peak (662 keV) was 14.3% [73], better than the current 18.0%. However, this resolution is still more than adequate for the requirements of a calorimeter performing capture measurements, where the purpose of the resolution is to discriminate between true and background events.

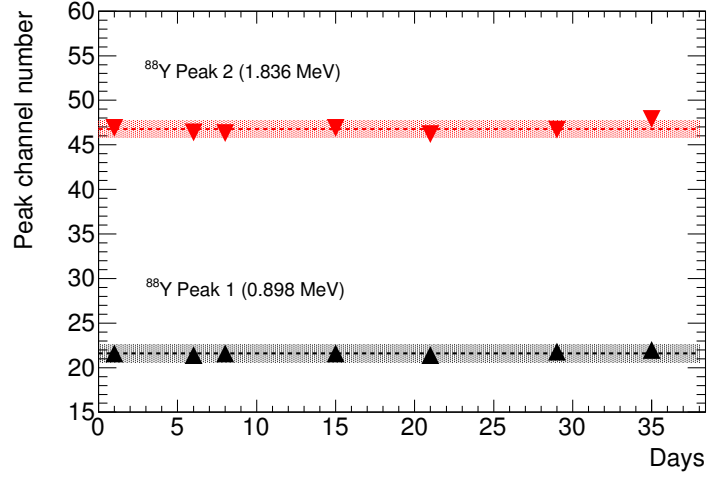


Figure 3.5: Example of a single BaF_2 modules response to the two ^{88}Y peaks over time. The shaded areas represent one channel either side of the mean value.

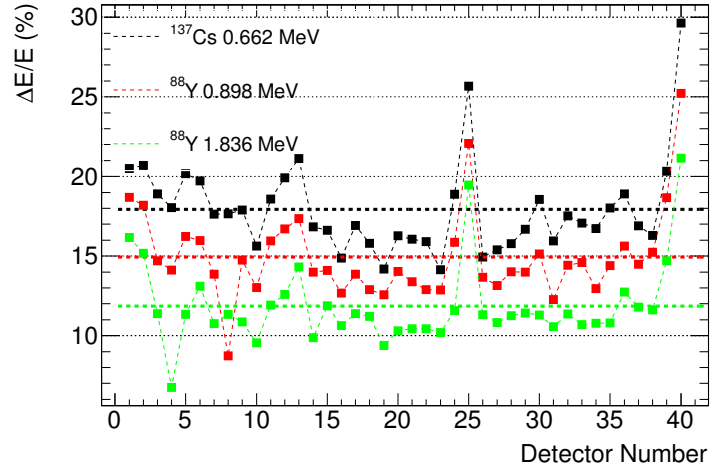


Figure 3.6: Individual detector resolutions for three separate energy points.

3.1.4 Coincidence analysis

The aim of measuring with a calorimeter such as the TAC is to detect all the γ -rays emitted in a capture cascade. Therefore, after calibrating the 40 modules in both time and energy one must transform the information from the individual crystals into so-called TAC events. This is done offline by analysing the 40 modules in coincidence using software. The software *baf2root* scans these data and, after registering a signal in any detector, opens a coincidence window during which any other signal throughout the TAC is grouped into the same event with the same detection time as the initial signal. If this is the case and multiple signals fall within one time window, the signal energies are summed to give a total deposited

energy E_{sum} , and the number of crystals involved is recorded as the multiplicity, m_{cr} .

A key point within this process is the width of the coincidence time window. Although γ -rays from a capture cascade are all released typically within $\sim 10^{-15}$ s, there is a much larger uncertainty in time from the flash-ADCs, and also a γ -ray can take ~ 1 ns to transverse the TAC therefore by making the coincidence window too small, one could miss γ -rays that are from the same capture cascade. Of course, if one makes the coincidence window too wide signals from different capture cascades will start to be grouped together, thus a compromise must be found. Studies have been performed, investigating the optimum coincidence window during previous measurements with the TAC [74] which found the TAC is able to accurately use a 10 ns coincidence window, however to be certain not to miss γ -rays from the same capture cascade a 20 ns time window width has been adopted for this work.

3.1.5 Time-of-flight to neutron energy calibration

As described in section 1.4, to determine the neutron energy using the time-of-flight method one must know the production and detection times of the neutron and also the flight path length. The PKUP detector is situated within the proton beam line before the spallation target and thus registers the proton pulse, therefore this signal gives a reference estimation time for the neutron production. The neutron detection time (t_{det}) is given by the time the capture event is registered in the TAC. Since the time of the PKUP signal does not exactly coincide with the neutron production time, we must introduce another constant, t_{offset} into Equation 1.4 to obtain the accurate neutron production time:

$$E_n(\text{eV}) = \left(\frac{72.2983 \cdot L(\text{m})}{t_{det}(\mu\text{s}) - (t_{pkup}(\mu\text{s}) + t_{offset}(\mu\text{s}))} \right)^2, \quad (3.3)$$

which takes into account the offset between the true neutron production time and the time when the PKUP registers the passage of the proton beam just before impinging upon the spallation target.

In order to determined the values of L and t_{offset} a function, given by Equation 3.3, has been fitted to the data from ²³⁸U resonances with well known energies. Indeed, the first four resonances of ²³⁸U can be considered energy standards [75], that is their position in neutron energy is known with 0.015% uncertainty. Our experimental data tell us t_{det} and t_{pkup} and the values of L and t_{offset} are fitted so that the calculated neutron energy for the resonances agrees with the ENDF/B-VII.1 values (see Figure 3.7). However, the first four resonances are thousands

of ns wide, and t_{offset} is expected to be tens or hundreds of ns therefore these resonances are insensitive to this parameter. Therefore, it is necessary to take narrower resonances at higher neutron energies, where although the resonance energies are not considered standard they are still very accurately known allowing a fit of Equation 3.3 to be performed to these data resulting in the required time-of-flight calibration parameters.

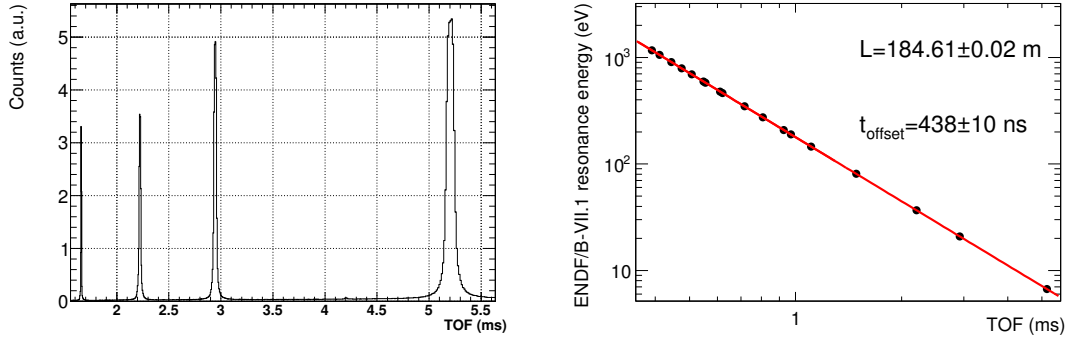


Figure 3.7: Left: ^{238}U time-of-flight spectrum showing the first four resonances included in the fit. Right: the fit to these data and the values found in the nuclear data libraries to determine the neutron energy calibration parameters.

Figure 3.7 shows the performed fit where it is observed that the points follow the expected behaviour from Equation 3.3 very closely, and the results are $L = 184.61 \pm 0.02 \text{ m}$ and $t_{\text{offset}} = 438 \pm 10 \text{ ns}$.

3.1.6 Dead-time and pile-up in the TAC

Although the n-TOF DAQ is dead-time free, the slow scintillation component of BaF_2 ($\tau_{\text{slow}} = 630 \text{ ns}$) is such that there is a non negligible probability that one signal is sitting on the tail of a previous one, and thus may be difficult to identify by the PSA routine. We consider the following situations:

1. Dead-time: The time interval following a signal in which a second is unable to be identified. In the case of the TAC, this results in a loss of counts, a reduction in the deposited energy of the event and a reduction of one unit in the multiplicity of the event.
2. Pile-up: Where two events are close in time and one signal from the first event and another signal from the second event are in the same crystal in such a way that the second one is lost and the energy reconstructed by the PSA for the first event is altered by the proximity to the second one. As a

result, the energy deposition of the first event will increase, and, as in the case of the dead-time, the multiplicity and energy of the second event will correspond to the sum of the constituent signals. In the case of the TAC, this results in a loss of counts, a loss of the measured multiplicity however an increase in the measured total energy.

In the case of a single detector, dead-time losses are usually quantified by simple formulas that depend on the dead-time model chosen: paralyzable or non-paralyzable. Here, a fixed dead-time τ is implemented after an event occurs. In the case of the paralyzable model, subsequent signals falling within the initial dead-time extend this time period by τ whereas in the non-paralyzable model subsequent signals within the initial dead-time do not extend this period any further. In the case of the TAC, the overall effect of dead-time and pile-up is a possible loss of TAC events that must be accounted for. However, the large number of detectors operating in coincidence and the complexity of the event reconstruction makes this a difficult task for which these existing methods can not be applied. Therefore a new method has been developed that allows calculating these corrections, even for the case of variable counting rates (see References [76] and [77] for details).

For the TAC, the value of the dead-time is found for each BaF₂ crystal by comparing the measured and theoretical distributions of time intervals between consecutive signals. The time (t) between subsequent signals for a constant count rate is expected to follow a distribution function $I_1(t)$ given by [78]:

$$I_1(t)dt = re^{-rt}dt, \quad (3.4)$$

where r is the rate of occurrence. Figure 3.8 shows the time interval between successive signals for a single detector in the TAC for different initial and final γ -ray energies.

As the time interval between signals decreases, it is observed at some time the measured distribution of signals deviates from the expected and it is at this time interval that we define our dead-time. From Figure 3.8 it is clear to see that the value of the dead-time varies depending on the energy of the initial (E_1) and second (E_2) signal. The value of this dead-time has been determined for all combinations of E_1 and E_2 in energy intervals of 500 keV up to 6.5 MeV [76] and the resulting two dimensional distribution is seen in Figure 3.9.

The average dead-time value ($\bar{\tau}$) is $\sim 1 \mu\text{s}$ however it can be as large as $3 \mu\text{s}$ if the first signal has a high energy and the second signal a low energy. This indicates that dead-time losses will become significant when the count rate is of the order 1 count/ μs , which as will become apparent is the case for many resonances

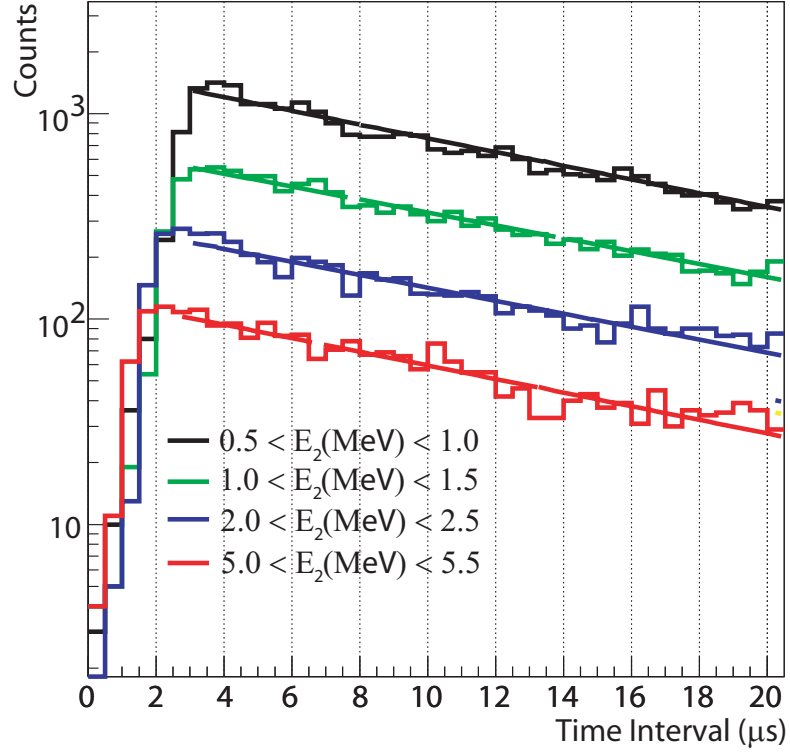


Figure 3.8: Time interval distributions for initial signals (E_1) between 6 and 6.5 MeV and subsequent (E_2) signal amplitudes.

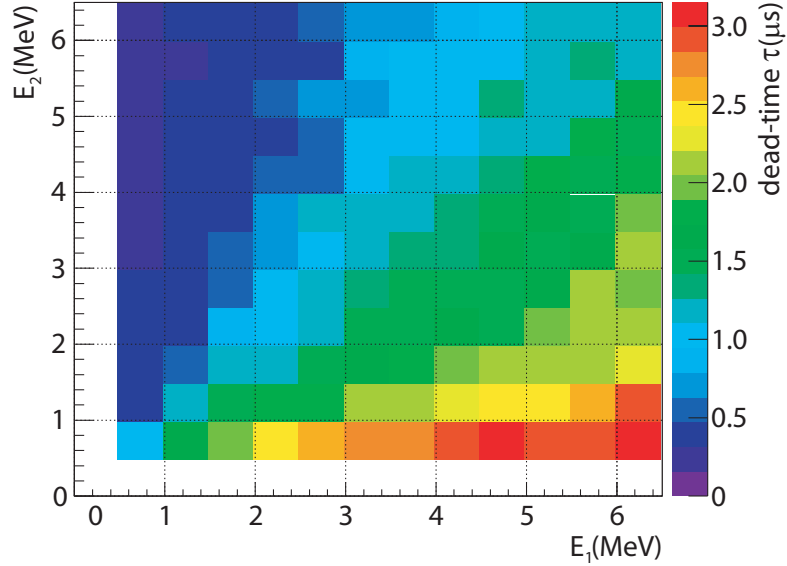


Figure 3.9: Dead-time values for the TAC for all combinations of (E_1) and (E_2).

within this work. The effects of significant dead-time and pile-up are not only a loss of events but a modification of the total energy and multiplicity measured within the TAC of the capture cascades. This changes the efficiency of detecting capture cascades depending on the analysis conditions in deposited energy and multiplicity chosen. Finally, when measuring narrow resonances in time-of-flight

we are no longer dealing with a constant count rate approximation, meaning the dead-time and pile-up effects will alter the measured data at later time-of-flights, which could be outside the resonance or even within a subsequent resonance. To make all these corrections, an innovative dead-time correction model is used within which the dead-time values as a function of E_1 and E_2 form the first ingredient. The full methodology of this correction is detailed in Section 4.1.2 for the specific case of the ^{238}U measurement.

3.2 Backgrounds

Alongside measuring capture cascades by time-of-flight there are several unavoidable background contributions to the measured data. The backgrounds present within the $^{238}\text{U}(n,\gamma)$ data are presented within this section alongside the methods used to reduce their overall contribution to the measurement. Figures 3.10 and 3.11 illustrate the typical deposited energy spectrum and neutron energy spectrum for the TAC which will be explained in detail within this section.

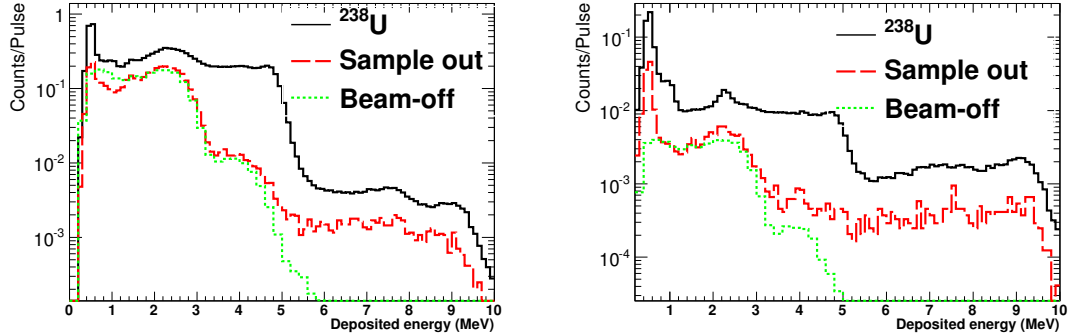


Figure 3.10: Typical TAC deposited energy spectra for the neutron energy ranges 1 eV-10 keV (left) and 1 keV-10 keV (right).

3.2.1 Beam-off background

One form of background is that which is not correlated with the neutron beam and remains constant over time. Such a background corresponds to radioactive decays from potassium within the concrete walls (1.461 MeV), β -decays from the Ra isotopes in the BaF_2 crystals (up to ~ 5 MeV) and activity from the ^{238}U and its daughter products within the sample. This background is characterised by dedicated beam-off measurements both with and without the ^{238}U sample present, where data are taken for 32 ms mimicking the equivalent time that the TAC is

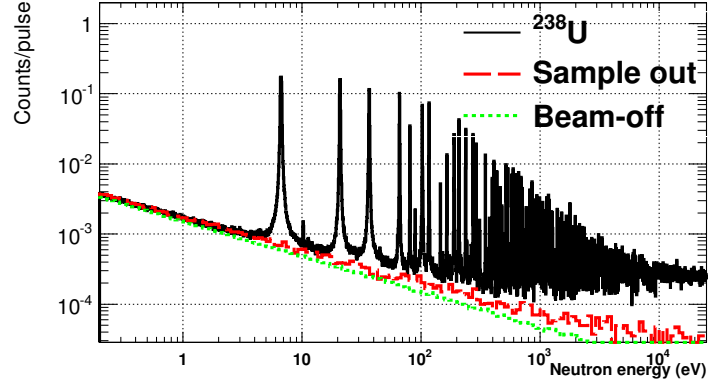


Figure 3.11: A typical neutron energy spectrum for the analysis conditions $m_{cr} > 1$ and $2.5 < E_{sum}(\text{MeV}) < 5.75$.

measuring for during a neutron pulse. This type of background, coming from radioactive decays is constant in time and thus follows the form $\frac{a}{\sqrt{E_n}}$ when expressed as a function of neutron energy. Figure 3.12 illustrates the total energy deposited in the TAC during beam-off measurements with and without the ^{238}U sample present. Here, after pulse shape analysis and coincidence analysis is performed, a histogram displays the total number of counts as a function of the total energy deposited in the TAC normalised to the total number of proton pulses received during this measurement, or in the case of beam-off the equivalent number of pulses corresponding to the total length of the measurement in time.

As can be seen from Figure 3.12 a large proportion of the beam-off background is found below 3 MeV and is thus greatly reduced by setting a condition (threshold) on multiplicity. Furthermore, the increase in background from the ^{238}U and its decay chains radioactivity is negligible above 2 MeV. Contributors to this spectrum are ^{40}K within the concrete walls giving rise to a 1.461 MeV γ -ray and the radium isotopes (^{226}Ra and ^{228}Ra) and their decay chains. Although α -particles can be discriminated due to their timing properties, β -decays within the chain (such as ^{214}Bi) give rise to electrons and coincident γ -rays with a maximum energy of 5 MeV [62].

One can histogram these counts normalised to pulses/equivalent time as a function of neutron energy. In the case of the beam-off data, the equivalent neutron energy is calculated using Equation 1.4 where the time-of-flight is given by the time elapsed after the opening of the 32 ms time window.

Figure 3.13 illustrates the experimental beam-off data as a function of equivalent neutron energy. As expected, when plotted on a (log,log) scale these data are linear and can be described by a fitted function, which has the benefit of reduc-

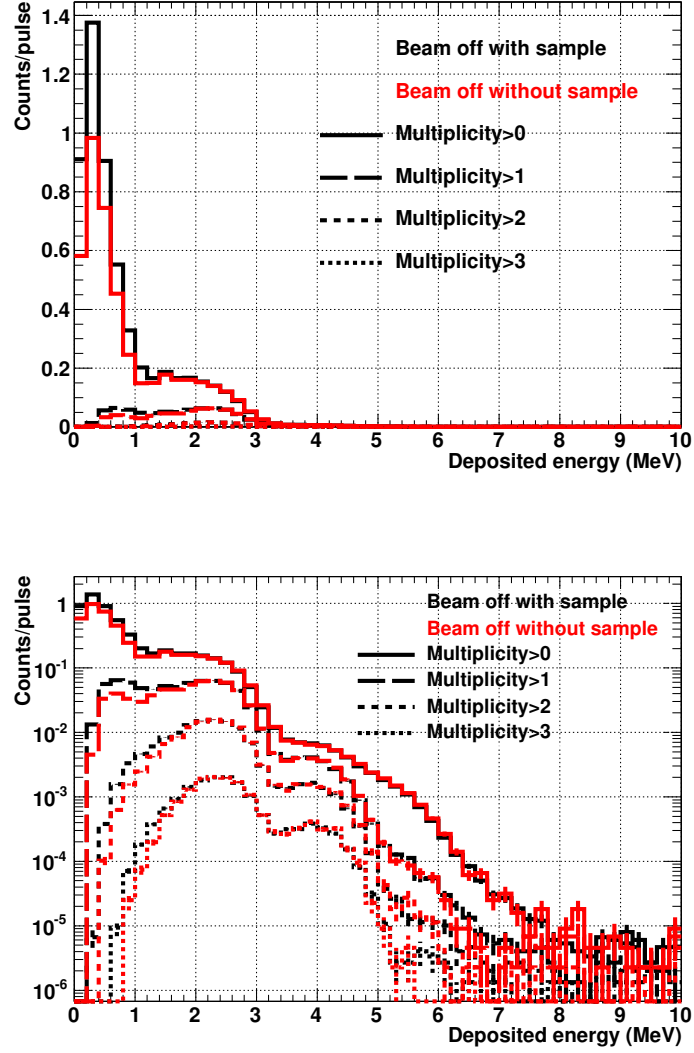


Figure 3.12: Beam-off deposited energy spectra for runs with and without the ^{238}U sample present on linear scale (above) and log scale (below).

ing statistical fluctuations. Data are shown for different analysis conditions not only corresponding to cuts in multiplicity but also restrictions in the minimum deposited energy.

From Figures 3.12 and 3.13 it is shown that the beam-off background is reduced by more than a factor of 10 when using restrictive (multiplicity>3) analysis conditions and by a factor of three when changing from multiplicity>1 to multiplicity>2.

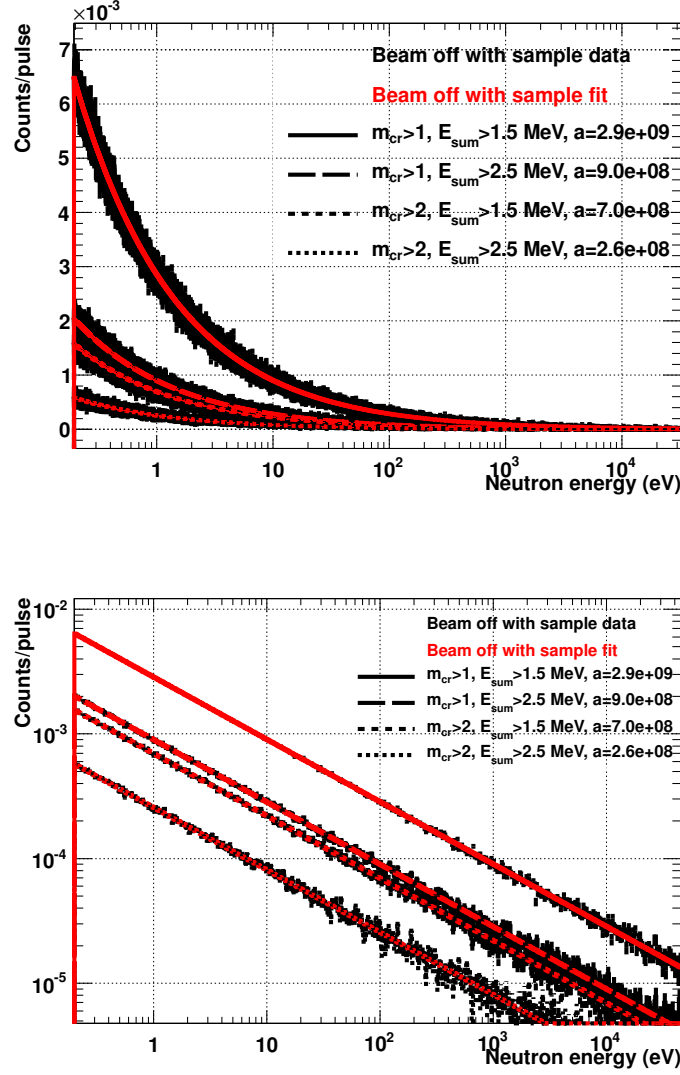


Figure 3.13: Experimental beam-off neutron energy spectra with the sample present and the corresponding fits for different analysis conditions in linear (above) and log (below) scales.

3.2.2 Beam-on (sample out) background

The main background contribution arises from the neutron beam interacting with materials other than the ^{238}U sample. This was determined by dedicated measurements with the neutron beam on but the ^{238}U sample removed from the beam line. The cross sections of the reactions giving rise to this background of course change with neutron energy, therefore the contribution varies with neutron energy. After subtracting the deposited energy beam-off background one is left with just the contributions from the neutron beam, as demonstrated for the neutron energy range 1-10 keV in Figure 3.14.

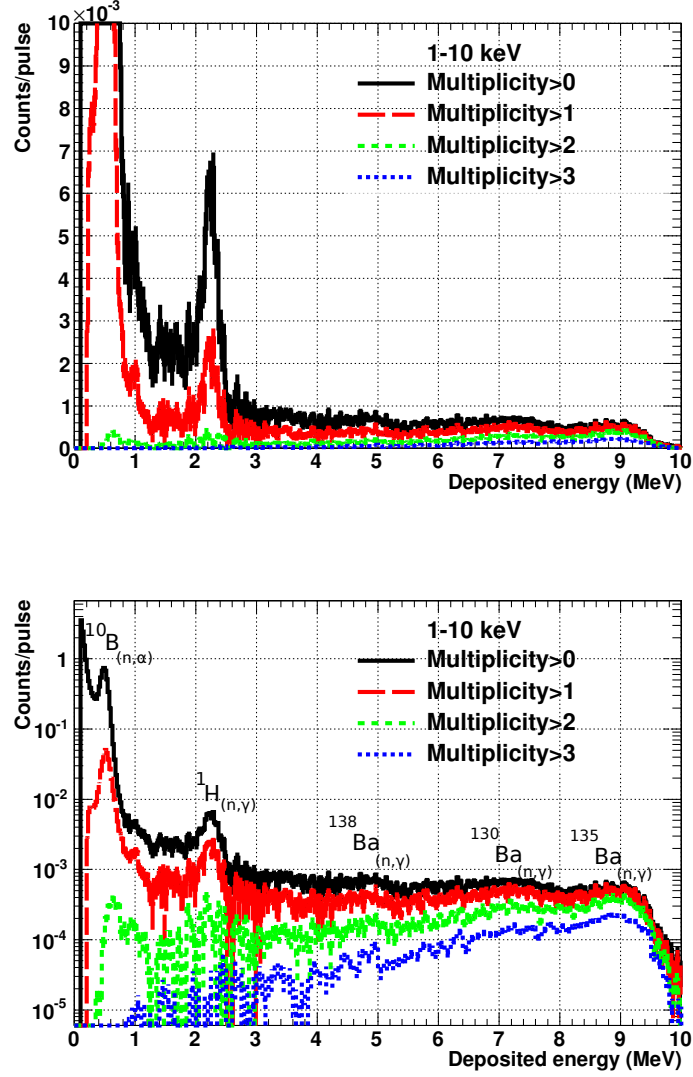


Figure 3.14: Sample out deposited energy spectra after subtracting the beam-off background with different cuts in multiplicity for 1-10 keV neutrons in linear scale (above) and logarithmic scale (below).

The deposited energy spectra in Figure 3.14 show a peak at 478 keV relating to $^{10}\text{B}(n,\alpha)$ reactions in the crystal capsules and in the neutron absorber (composed of borated polyethylene) and the subsequent decay of $^7\text{Li}^*$, a peak at 2.2 MeV from $^1\text{H}(n,\gamma)$ reactions within the neutron absorber and finally a high energy component arising from (n,γ) reactions on the various barium isotopes present within the crystals. It is observed that most of the backgrounds counts are at low γ -ray energies and these are drastically reduced by enforcing a condition in the multiplicity by one ($m_{cr} > 1$) and three ($m_{cr} > 2$) orders of magnitude compared to $m_{cr} > 0$. Furthermore it is observed that a minimum deposited energy of 2.5 MeV eliminates the majority of the background counts originating from the neutron

beam. It is also observed that the high energy contribution from capture in Ba ranges up to 10 MeV.

3.2.3 Neutron Scattering (Sensitivity) Background

The large volume of the TAC and the sizeable capture cross section of its constituents (mainly BaF₂) make it possible that neutrons scattered at the sample under study are absorbed within the TAC, generating the so-called neutron scattering background. This type of background, which becomes sizeable when the capture and scattering cross sections of the isotope under study are comparable, has the particularity that it follows the same resonant structure as the capture reactions of interest (as demonstrated in Figure 1.3).

A quantity of interest is the neutron sensitivity ($\varepsilon_{n,n}$) which is defined as the probability of detecting a scattered neutron as a function of neutron energy. One possible method of calculating $\varepsilon_{n,n}$ is with Monte Carlo simulations which transport the neutrons throughout the whole geometry. However, it is possible to calculate $\varepsilon_{n,n}$ experimentally. To do this, one measures a sample that can be considered a pure scatterer. For this work, a natural carbon sample was used, whose scattering to capture ratio (σ_n/σ_γ) is $\sim 10^4$ at 1 eV and $\sim 10^5$ at 1 keV. Making the assumption that all counts detected within the TAC when irradiating carbon are from scattered neutrons rather than capture events, one can then compare the measured yield to the expected carbon yield from the nuclear data libraries from which the neutron sensitivity is inferred by:

$$\varepsilon_{n,n} = Y^{meas}/Y^{th}, \quad (3.5)$$

where the measured yield Y^{meas} is given by

$$Y_{n,n}^{meas}(E_n) = \frac{C(E_n) - B(E_n)}{N_{BIF} \cdot \phi_n(E_n)}, \quad (3.6)$$

where $C(E_n)$ and $B(E_n)$ are the total and background counts, N_{BIF} is the sample beam interception factor and $\phi_n(E_n)$ is the neutron flux. Assuming $\sigma_{n,n} = \sigma_{n,tot}$, the expected theoretical yield is given by:

$$Y_{n,n}^{th}(E_n) = 1 - e^{-n\sigma_{n,n}(E_n)}, \quad (3.7)$$

where n is the areal density of the sample in atoms per barn and $\sigma_{n,n}$ is the scattering cross section in barns. The neutron sensitivity is thus given by the

combination of equations 3.6 and 3.7:

$$\varepsilon_{n,n} = \frac{C(E_n) - B(E_n)}{BIF \cdot \phi_n(E_n) \cdot (1 - e^{-n\sigma_{n,n}(E_n)})}. \quad (3.8)$$

The resulting theoretical and experimental yields are shown in Fig. 3.15. As will become evident in Section 3.3, the efficiency for detecting γ -rays changes with the analysis conditions chosen, therefore the experimental yields have been created for varying cuts in multiplicity.

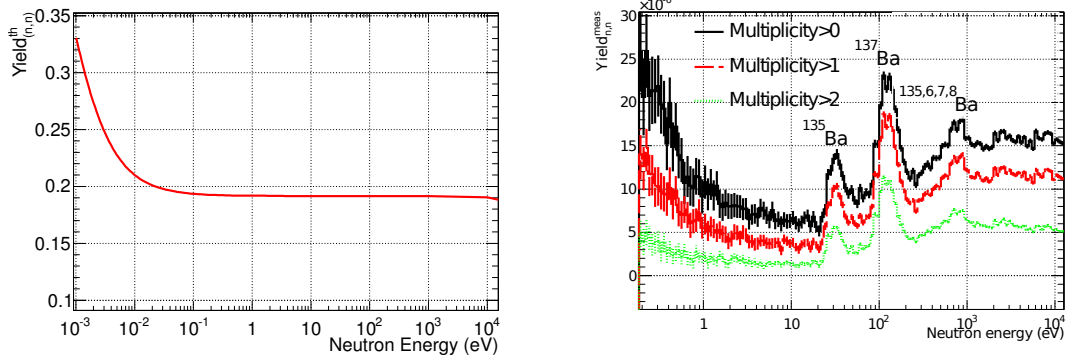


Figure 3.15: The theoretical carbon yield (left), using the cross section from JEFF-3.1.2 and the measured experimental carbon yield (right) for different cuts in multiplicities.

It can be seen that the theoretical carbon yield in the energy range of interest shows very little structure, remaining at a constant level of ~ 0.19 barns between 0.1 eV and 20 keV however the measured experimental yield exhibits large structures in this region. This is because the capture cross sections of the TAC materials have resonances; in particular, the structures at 25 and 130 eV are due to resonances in the ^{135}Ba and ^{137}Ba capture cross sections respectively.

The neutron sensitivity $\varepsilon_{n,n}$ is now calculated by taking the ratio between the theoretical and experimentally measured yields. Figure 3.16 shows $\varepsilon_{n,n}$ for different analysis conditions typical of those used for capture measurements. They correspond to cuts in the multiplicity and deposited energy to maximise the capture counts to background counts ratio (see Section 3.3).

The error bars in Figure 3.16 relate to the statistical error only, however there are also systematic effects adding to the uncertainty of $\varepsilon_{n,n}$. Dead-time and pile-up effects are negligible as the counting rate remains below 0.3 counts/ μs , however there is a lower limit of 2% for the uncertainty from the measurement of the neutron flux, therefore this experimental method of determining the neutron sensitivity is accurate to 2-3%.

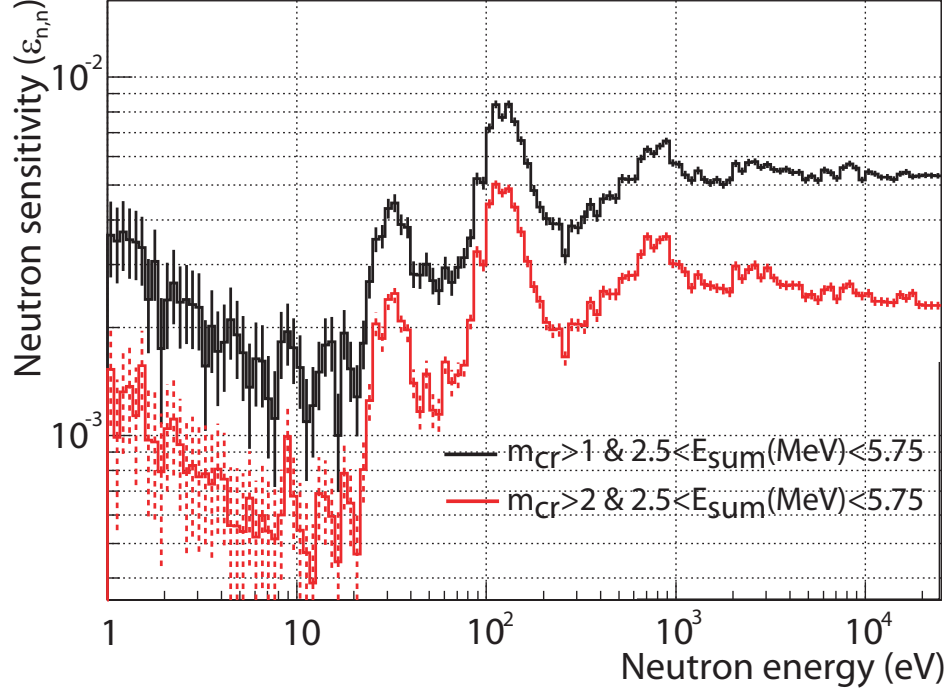


Figure 3.16: The neutron sensitivity for different multiplicities in the TAC.

It is seen that $\varepsilon_{n,n}$ varies between $\sim 0.05\%$ and 0.5% depending on the neutron energy and the analysis conditions chosen. These values correspond to a reduction by a factor of 3-5 with respect to those found with the previously used neutron absorber (see Reference [63] for more details). The neutron sensitivity is approximately 200 times lower than the efficiency of the TAC for detecting capture cascades (see Section 4.1.4), therefore the neutron scattering background becomes prominent if $\sigma_{n,n} > \sigma_{n,\gamma}$. The calculation of the neutron scattering/sensitivity background for the particular case of ^{238}U is discussed in detail in Section 4.1.1.

3.3 Detection efficiency and analysis conditions

The previous sections have demonstrated that the level of background within a TAC capture cross section measurement can be reduced by applying analysis conditions upon the multiplicity and deposited energy of the detected events. However these analysis conditions also reduce the level of detected capture counts therefore lowering the efficiency of the TAC and thus the accumulated statistics. The optimum analysis conditions will vary for each TAC measurement depending on factors such as the energy and multiplicity of the capture cascades, the sample activity and the TAC count rate. Figure 3.17 shows the deposited energy spectra for the ^{238}U sample and the corresponding backgrounds for different conditions in multiplicity.

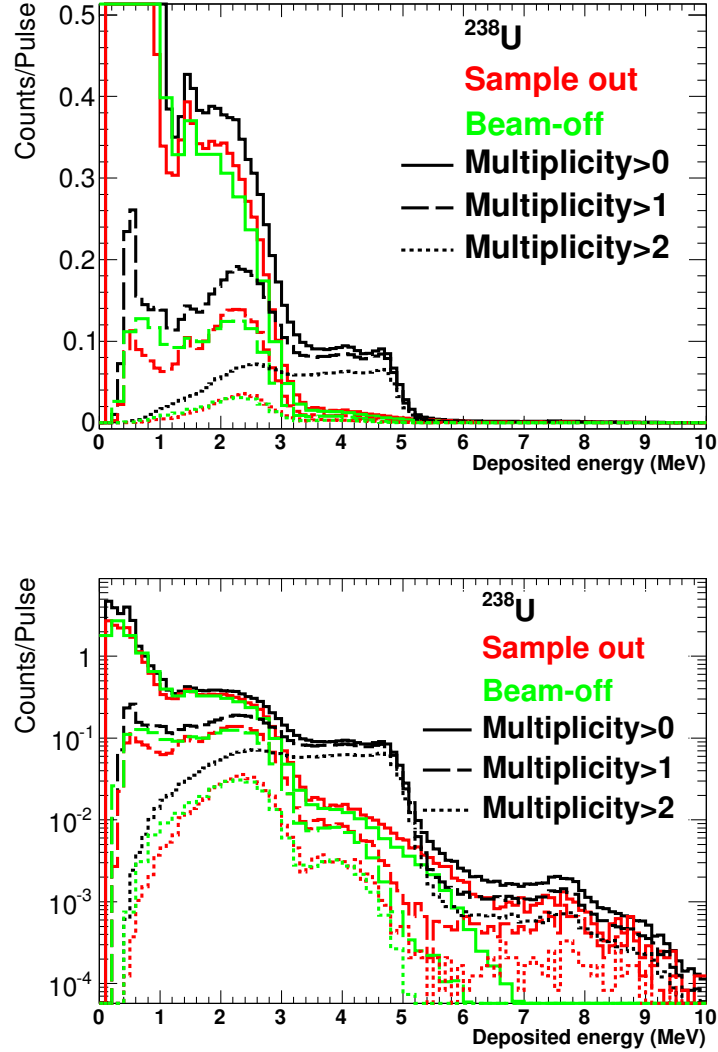


Figure 3.17: TAC ^{238}U deposited energy spectra in linear (above) and logarithmic (below) for the neutron energy range 1-10 eV.

The upper limit in deposited energy from a capture cascade corresponds to S_n of the compound nucleus formed after neutron capture, which in the case of ^{238}U is $^{239}\text{U}^*$ ($S_n=4.8$ MeV). This is illustrated in Figure 3.17 where a sharp loss of counts occurs above ~ 4.8 MeV. This upper limit in energy is extended by ~ 1 MeV due to detector resolution and pile-up of small signals, therefore an analysis condition of maximum deposited energy at 5.75 MeV has been chosen. Any events above this energy are either due to pile-up of more than one capture event, or from the contribution of the neutron scattering background. As such, the efficiency for detecting capture cascades is not affected by this upper cut in deposited energy. To determine the optimum thresholds in deposited energy and multiplicity one must investigate the loss of efficiency and background reduction, looking for a

compromise between both.

One possible method of investigating the efficiency of the TAC is to use Monte Carlo simulations [79], however in this work an experimental approach is taken using the experimental yield:

$$Y_{n,\gamma} = \frac{C(E_n) - B(E_n)}{\varepsilon_{n,\gamma}(m_{cr}, E_{sum}) \cdot \phi_n(E_n) \cdot N_{BIF}}, \quad (3.9)$$

where $C(E_n)$ and $B(E_n)$ are the total and background counts, $\varepsilon_{n,\gamma}(m_{cr}, E_{sum})$ is the efficiency for detecting capture cascades, $\phi_n(E_n)$ is the neutron flux and N_{BIF} is the beam interception factor. As it will be explained in Section 4.1.4, once the experimental yield has been found, the efficiency of the TAC can be quantified by use of the Saturated Resonance Method [80]. At this stage, we require a relative or approximate efficiency for different sets of analysis conditions to allow determination of the optimum analysis conditions. Therefore, it is adequate to subtract the beam-on (sample out) and beam-off backgrounds and divide by the neutron flux, neglecting the neutron scattering background and pile-up/dead-time effects and compare this approximate experimental yield to the yield expected from the JEFF-3.1.2 cross section library as calculated by SAMMY, as shown in Figure 3.18 for the first resonance. Assuming a N_{BIF} value of 0.975 (from the geometry of the sample and the beam profile), the scaling factor between both yields gives directly the detection efficiency. The values obtained for different analysis conditions on deposited energy and multiplicity are listed in Table 3.1.

Table 3.1: Approximate TAC efficiencies for different analysis conditions.

Multiplicity	Deposited energy	Approximate efficiency (%)
>1	$1.5 < E_{sum}(\text{MeV}) < 5.75$	83
>1	$2.5 < E_{sum}(\text{MeV}) < 5.75$	65
>2	$1.5 < E_{sum}(\text{MeV}) < 5.75$	58
>2	$2.5 < E_{sum}(\text{MeV}) < 5.75$	48

The optimum analysis conditions chosen to be used are $m_{cr} > 1$ and $2.5 < E_{sum}(\text{MeV}) < 5.75$, as this keeps the efficiency relatively high, thus minimising lost statistics, but reduces largely the background counts, in particular the 478 keV γ -ray from $^{10}\text{B}(n,\alpha)$ reactions and the subsequent decay of $^7\text{Li}^*$ and the 2.2 MeV γ -ray from $^1\text{H}(n,\gamma)$ reactions. This approximately triples the capture to background ratio which in the region 1 eV to 10 keV with no conditions is 2.13, whereas with the chosen analysis conditions is 6.07. The improvement within resonances is illustrated in the neutron energy range 1-100 eV in Figure 3.19.

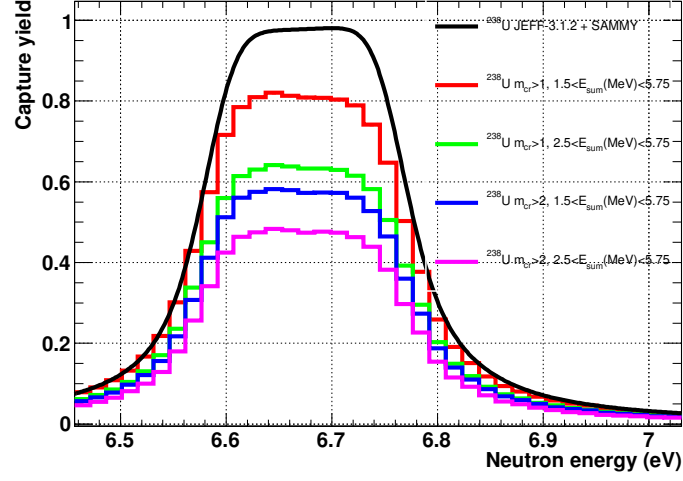


Figure 3.18: An approximation of the experimental yield (ignoring neutron scattering and pile-up/dead-time corrections) of the first ^{238}U resonance for different analysis conditions compared to the expected yield as predicted by SAMMY from the JEFF-3.1.2 ^{238}U cross section.

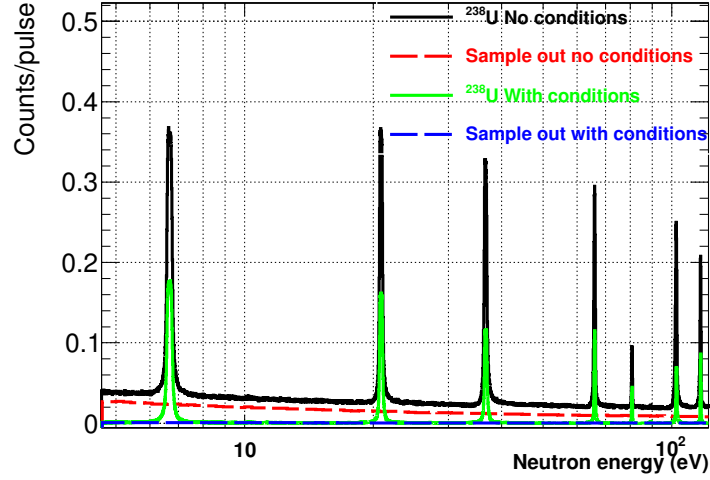


Figure 3.19: The neutron energy interval 1-100 eV for ^{238}U and background (sample out) data with and without conditions.

3.4 Effect of the γ -flash on the TAC

As introduced in 2.1, after the γ -flash the BaF_2 scintillators take a finite time (tens of μs) to recover their baseline and their normal behaviour as illustrated in Figure 3.20. The time the TAC takes to recover varies depending on the intensity of the neutron beam, however it varies from a minimum of 40 μs which corresponds to an upper limit in neutron energy of 100 keV.

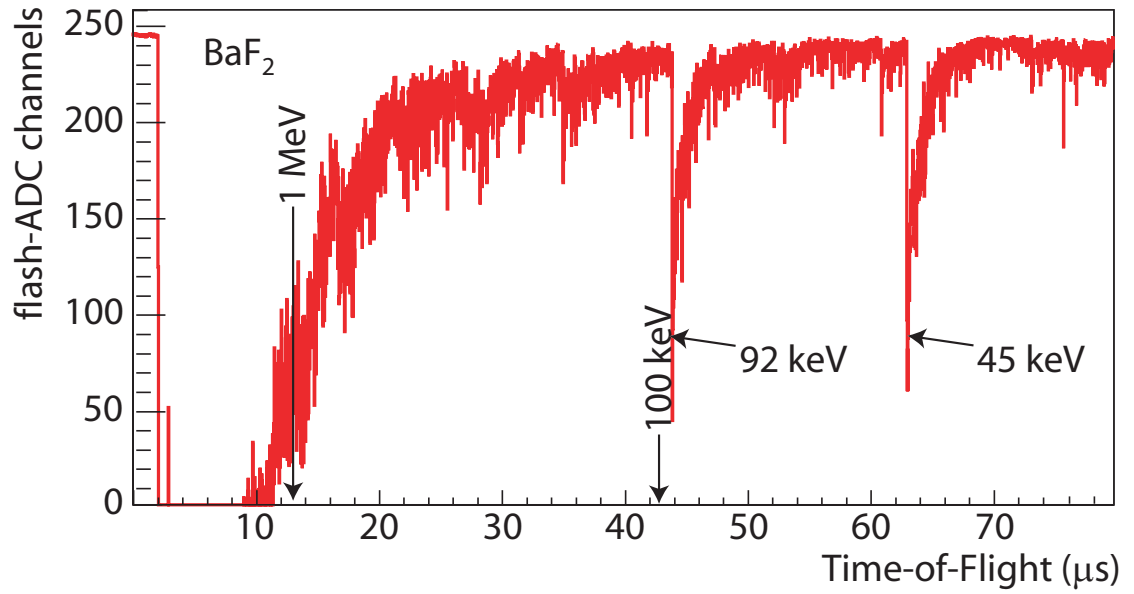


Figure 3.20: The response of a single BaF_2 crystal to the γ -flash.

In previous TAC measurements, there has always been additional limiting factors (for instance the presence of thick Al or Ti sample capsules that introduced a dominant background above a few keV) and as such an accurate analysis has never been performed before above 5 keV. The limiting factors for the higher neutron energy limit achievable in the particular case of the $^{238}\text{U}(n,\gamma)$ measurement will be discussed in Section 4.1.3.

CHAPTER 4

Analysis and results on ^{238}U

The analysis tools and techniques used to produce a precise $^{238}\text{U}(\text{n},\gamma)$ cross section are documented in this section. The final stages of the analysis are presented within this chapter leading to a comparison of these results and the current evaluated data sets.

4.1 ^{238}U Data reduction: Yield procurement

The first stage of the ^{238}U data analysis is the production of an experimental yield which can then be analysed looking at individual resonances (Resolved Resonance Region formalism) or averaging out the data over wide energy intervals (Unresolved Resonance Region). The following analysis stages all apply the conditions in multiplicity and deposited energy as discussed in Section 3.3 ($m_{cr} > 1$, $2.5 < E_{sum}(\text{MeV}) < 5.75$).

4.1.1 Background subtraction

There are three components in the background of the $^{238}\text{U}(\text{n},\gamma)$ measurement: environmental background, beam-related/sample-unrelated background, and the background from neutrons scattered at the sample and then captured somewhere else giving rise to signals in the TAC. The first two are determined experimentally by means of a beam-off and a sample out measurement. The beam-off background is constant in time and thus follows a $\frac{1}{\sqrt{E}}$ when represented as function of the neutron energy; thus the measured distribution in neutron energy is fitted to this function. The beam-off background is subtracted from the sample out and ^{238}U data, and then the sample out is subtracted from the ^{238}U data. In this way the only remaining background is that produced by neutrons scattering in the

^{238}U sample. The situation is illustrated in Figure 4.1, where one sees the very favourable capture to background ratio achieved in this measurement.

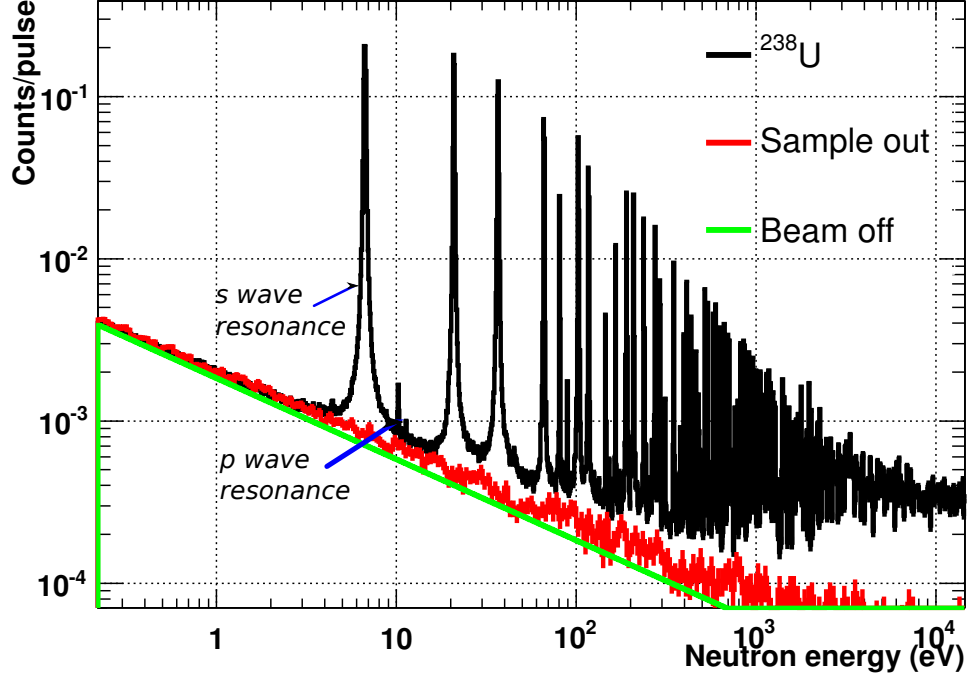


Figure 4.1: ^{238}U , sample out and beam-off neutron energy spectrum.

The background from scattered neutrons is a particularly problematic one, as the scattering cross section follows the same resonant pattern as the capture cross section that we are interested in. This background can be determined through two different methods: one analytical, one experimental.

To determine this background contribution analytically, the approximate efficiencies of the TAC to detect capture cascades ($\varepsilon_{n,\gamma}(m_{cr}, E_{sum})$) and scattered neutrons ($\varepsilon_{n,n}(m_{cr}, E_{sum})$) (see Sections 3.2.3 and 3.3 respectively) are used. With these efficiencies and considering the scattering to capture ratio for each resonance as the ratio of radiative and neutron widths (Γ_γ and Γ_n) as found in JEFF-3.1.2 we can estimate the expected neutron scattering contribution for each resonance as $\frac{\varepsilon_{n,n}\Gamma_n}{\varepsilon_{n,\gamma}\Gamma_\gamma}$. This is shown in Figure 4.2 for all resonances up to 20 keV.

Figure 4.2 illustrates a slight rise in the expected scattering contribution on a resonance by resonance basis with neutron energy. However, within this a vast variation is seen for the expected contribution on a resonance by resonance basis from $<10^{-2}$ which can be considered negligible, up to $\sim 50\%$ which implies this background is dominating compared to the sample out and beam-off and would be comparable to the contribution from $^{238}\text{U}(n,\gamma)$. However, this estimation does

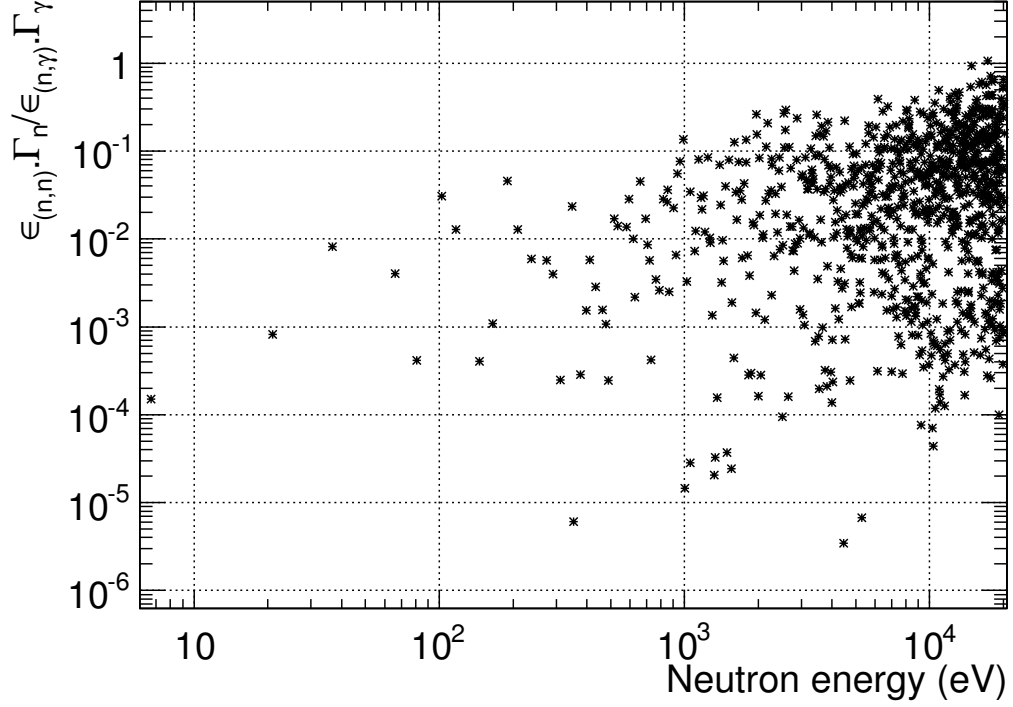


Figure 4.2: Expected ^{238}U neutron scattering contribution for the chosen analysis conditions of $m_{cr} > 1$ and $2.5 < E_{sum}(\text{MeV}) < 5.75$ taking the resonance parameters in the JEFF-3.1.2 database.

not take into account the strength (size) of the resonance, so can be misleading. To quantify the expected contribution across an energy region, we calculate a weighted mean where the weighting is the strength of each resonance, defined as the *resonance kernel* (RK):

$$RK = g_J \cdot \frac{\Gamma_n \cdot \Gamma_\gamma}{\Gamma_n + \Gamma_\gamma}, \quad (4.1)$$

where the spin factor g_J is defined as:

$$g_J = \frac{2J + 1}{(2l + 1)(2L + 1)}, \quad (4.2)$$

where l , L and J are the spins of the incident particle, target nucleus (^{238}U : $L=0^+$) and compound nucleus (^{239}U) respectively. Thus the neutron scattering contribution estimation in any one given energy region is:

$$(n, n)_{contribution} = \frac{1}{\sum_j RK_j} \cdot \sum_i RK_i \cdot \frac{\Gamma_n \cdot \varepsilon_{n,n}(m_{cr}, E_{sum})}{\Gamma_\gamma \cdot \varepsilon_{n,\gamma}(m_{cr}, E_{sum})}. \quad (4.3)$$

The expected contribution has been calculated for all known s-wave ($l=0$) resonances as p-wave ($l=1$) resonances will not be considered for this analysis and thus $g_J=1$. This is because the goal of this work is to perform an accurate cross section measurement and the statistics within p-waves are typically very small due to their weak strength (see an example p-wave resonance highlighted in Figure 4.1). The values of the average neutron scattering background contribution in different energy regions for all s-wave resonances are in Table 4.1.

Table 4.1: Expected scattering contribution for s-wave resonances in different neutron energy regions.

Neutron energy range (eV)	Expected contribution(%)
$1 < E_n < 500$	1.4
$500 < E_n < 1000$	3.6
$1000 < E_n < 2000$	5.6
$2000 < E_n < 5000$	6.6
$5000 < E_n < 10000$	7.5
$10000 < E_n < 20000$	13.2

As can be seen, on average the scattering contribution remains below 7% in the Resolved Resonance Region (below 5 keV) and below 13.2% in the Unresolved Resonance Region (5-20 keV). However, this analytical method will overestimate the scattering contribution. In practice, a neutron scattered within a resonance will be subsequently captured at a later time-of-flight. This is especially important at high neutron energies, as the width in time-of-flight of the resonances is small (~ 500 ns at 1 keV and ~ 100 ns at 5 keV), which is the same order of magnitude needed for a 1 keV neutron to transverse the TAC (~ 500 ns); therefore, neutrons scattered at the sample and subsequently scattered within the TAC before absorption are recorded at a later time-of-flight, often falling outside of the resonance. Furthermore, this method is only as accurate as the resonance parameters used as input. Indeed, the strength of the resonance will be reasonably well known, however the individual resonance widths (Γ_γ and Γ_n) may not be so accurately known due to the large correlation between the two. This can lead to differences between the analytical prediction and the actual contribution, therefore this method can not be used to give more than an estimation.

A more accurate way for determining and then subtracting the neutron scattering contribution makes use of the high efficiency and good energy resolution of the TAC. The neutron separation energy S_n for ²³⁹U is ≈ 4.8 MeV, whereas for the barium isotopes present in the crystals it is higher (between 4.2 and 9.1 MeV, depending on the isotope). Thus, if a neutron is captured in the TAC, γ -ray cascades can be emitted with a higher total energy than possible from a ²³⁸U capture reaction, thus we assume that all TAC events above a certain energy originate from

scattered neutrons. Following this principle, the counts from neutrons scattering in ^{238}U registered in the TAC at each neutron energy are calculated by comparing the ^{238}U and carbon deposited energy spectrum above 7 MeV, as illustrated in Figure 4.3. The high energy counts in the ^{238}U spectrum tell us the level of neutron scattering and the carbon data are used to scale this value to obtain the neutron scattering contribution within the chosen analysis conditions ($m_{cr} > 1$ and $2.5 < E_{sum}(\text{MeV}) < 5.75$).

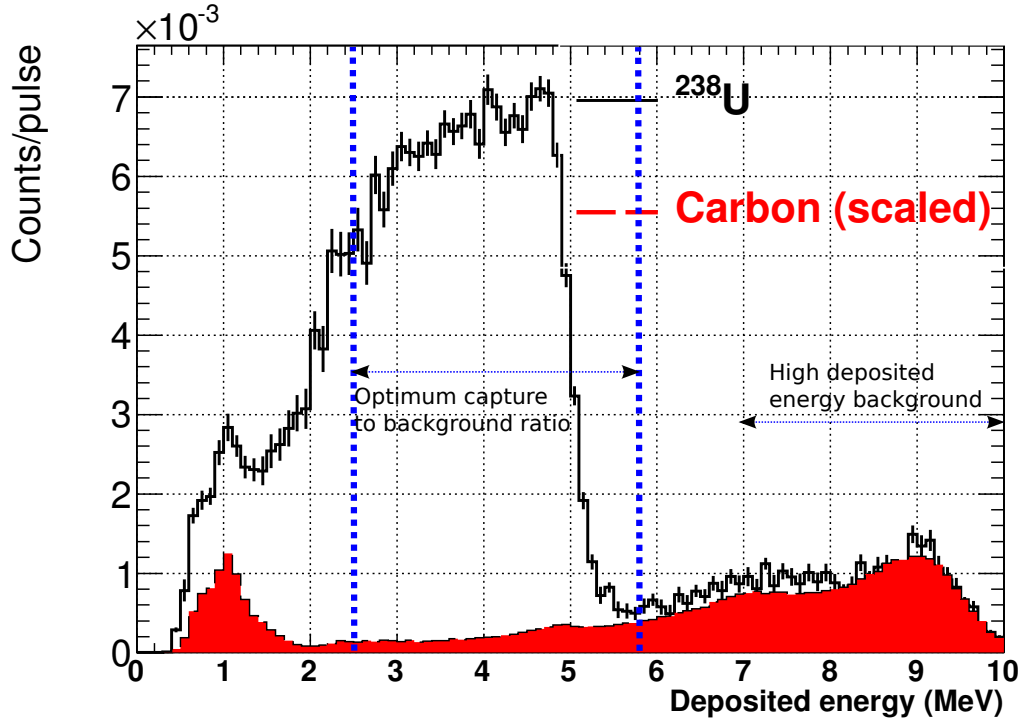


Figure 4.3: ^{238}U and carbon deposited energy spectrum in the neutron energy range 1 keV to 10 keV for $m_{cr} > 2$. The carbon spectrum has been scaled to match the number of ^{238}U counts above 7 MeV to allow an estimation of the scattering contribution within the ^{238}U analysis conditions chosen ($m_{cr} > 1$ and $2.5 < E_{sum}(\text{MeV}) < 5.75$).

Figure 4.4 displays the ^{238}U data before (red) and after (black) subtracting the neutron scattering background (green) for various resonances with differing $\frac{\Gamma_n}{\Gamma_\gamma}$ ratios utilising this experimental method.

For these example resonances, the contribution from scattered neutrons calculated in this way is 0.8% for the 36.7 eV resonance which is in perfect agreement with the analytical estimation (see Figure 4.2, also 0.8%). In the case of the 347.8 eV resonance the measured contribution is 3.5%, whereas the analytical correction is 2.5%. Finally the experimental contribution at the resonance peak for the 991

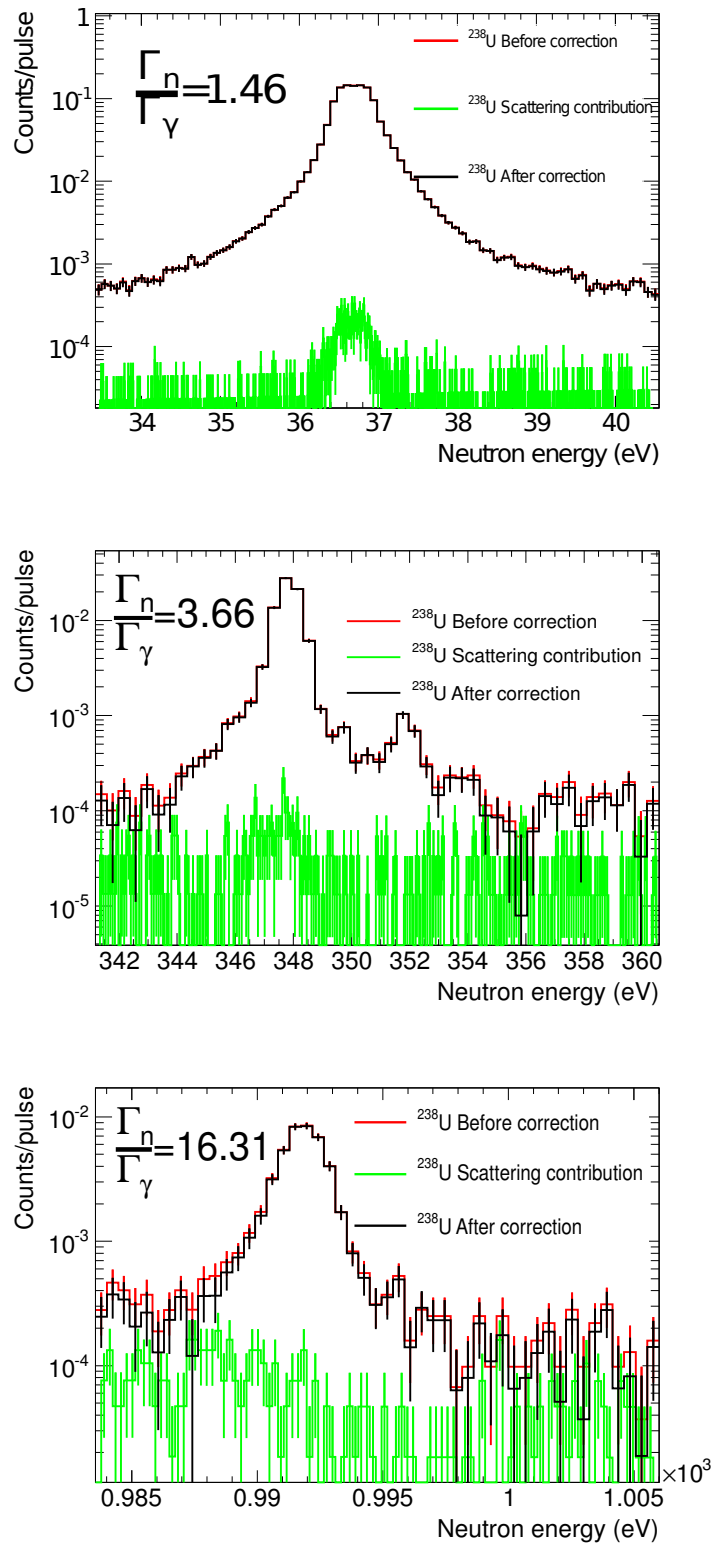


Figure 4.4: Three example resonances (top: 36.7 eV, middle: 347.8 eV, bottom: 991.8 eV) and their neutron scattering contribution as determined experimentally.

eV resonance is 7.75% and the analytical correction is 13.8%.

The observed differences can be attributed to many factors other than just the potential uncertainty in the values of Γ_γ and Γ_n . One possibility is that when the count rate is high the correction will be overestimated, as pile-up of signals lead to TAC events >7 MeV which are not just from scattered neutrons but also ^{238}U capture reactions, which is likely the case for the 347.8 eV resonance. This could be minimised by increasing the scattering high deposited energy limit from 7 MeV to 8 MeV, however this would greatly reduce the statistics for the experimental correction. At high neutron energies, as expected the scattering contribution is not as large as predicted analytically due to the time it takes a scattered neutron to be captured moving it out of the resonance in time-of-flight. Finally, the statistics of the high energy ^{238}U data can be low, leading to a large statistical uncertainty in this correction. However, the uncertainty introduced by this background does not go above 2%, as demonstrated between the general good agreement between measured and analytical scattering contributions at low neutron energies.

As will be discussed in Section 4.1.3, at high neutron energies the statistics within resonances is not high enough to allow an accurate resonance analysis to be performed. To analyse these data, a wider histogram binning is used which has the consequence that individual resonances can no longer be resolved. A further consequence of this is that the neutron scattering in the valleys between the resonances also contributes to these data, increasing the neutron scattering background.

Figure 4.5 shows the scattering effect with 20 bins per decade, where it is seen in the neutron energy region 5-10 keV around 10% of the recorded counts originate from scattered neutrons, increasing to $\sim 20\%$ at 20 keV. Although the magnitude of the correction is higher in this region, an uncertainty as large as 10% within the background estimation only corresponds to a 2% uncertainty for the final correction.

The neutron scattering correction is always a difficult and sometimes restricting component of a capture cross section measurement, however as demonstrated for the case of $^{238}\text{U}(n,\gamma)$ with the TAC the use of an experimental method measuring a pure neutron scattering sample the uncertainty introduced is at a maximum of 2% in the resonance region and $\sim 2\%$ when analysing the resonances as unresolved as there is a higher contribution owing to the valleys between resonances.

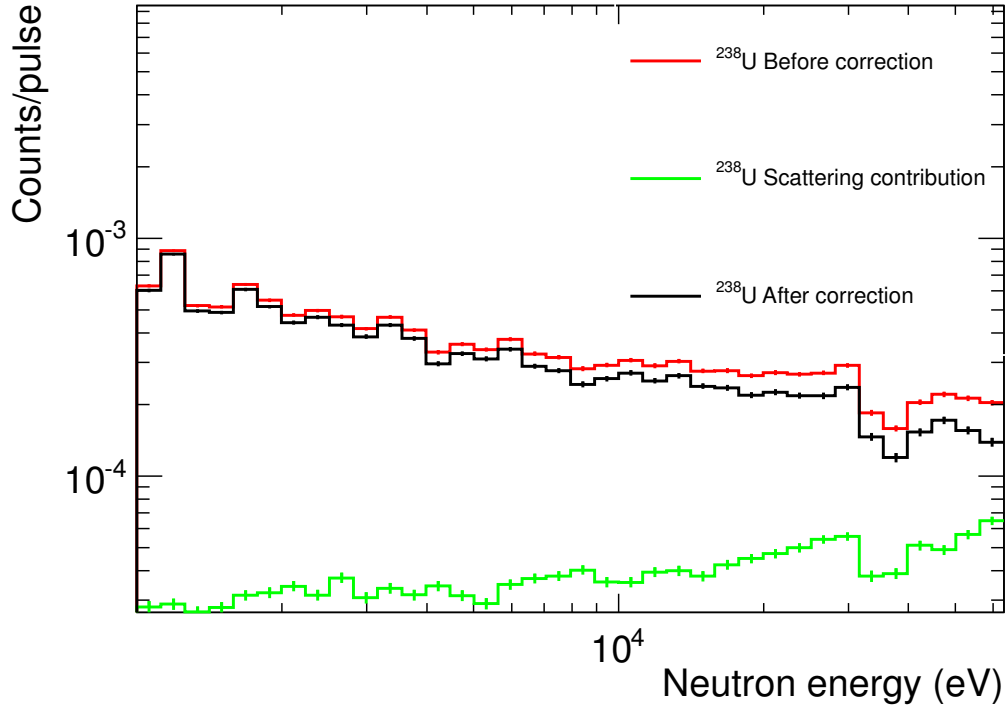


Figure 4.5: Neutron scattering contribution at high neutron energies for ^{238}U with 20 bins per decade.

4.1.2 Pile-up and dead-time correction

As introduced in Section 3.1.6, the TAC can suffer from dead-time and pile-up effects. In the present measurement these have been minimised by reducing the proton beam intensity per pulse and thus the count rate. However, as illustrated in Figure 4.6 high count rates are still present ($>1 \text{ count}/\mu\text{s}$) for many resonances especially for the MED pulse intensities.

The correction of dead-time losses and its effect on the efficiency for sizeable counting rates is based on a Monte Carlo simulation method that mimics the full counting and coincidence process in the TAC which is fully detailed in References [76] and [77]. The method requires three inputs:

1. The measured counting rate distribution under light analysis conditions (see Figure 4.6).
2. Detailed information on the energies and multiplicities of the capture cascades.
3. The identification probability for consecutive signals as a function of their energies and also separation in time (see Section 3.1.6).

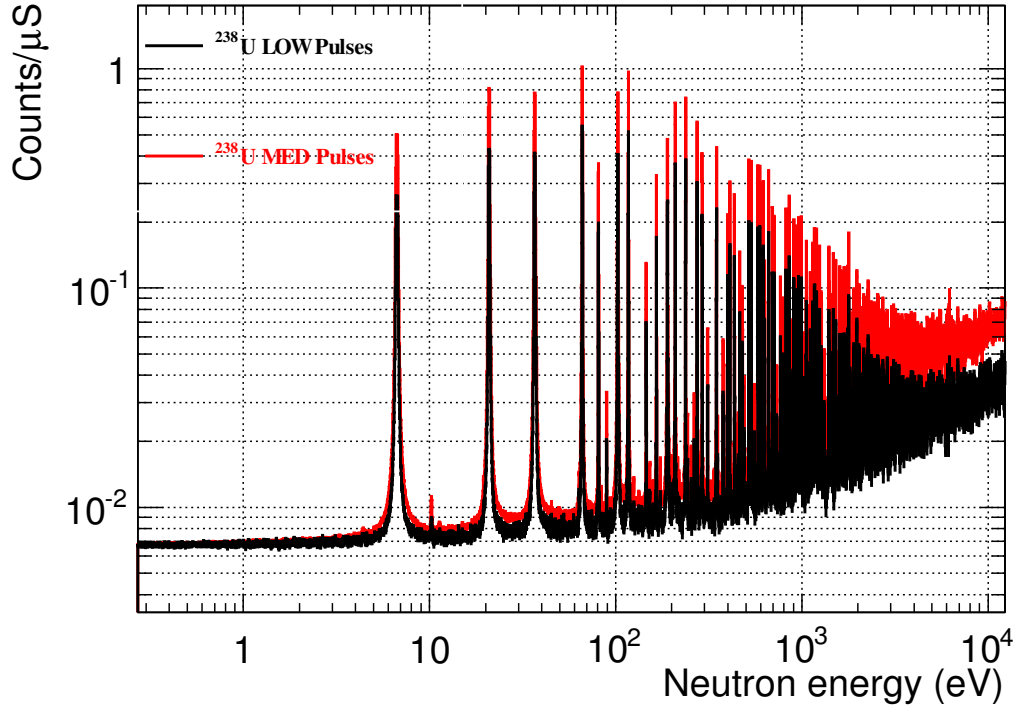


Figure 4.6: ^{238}U count rate for minimal conditions ($m_{cr} > 0$, $E_{sum} > 1$ MeV) for the two pulse intensities used for this work.

Details of the capture cascades requires knowledge of the complete nuclear level scheme below the neutron separation energy, which is not known for ^{239}U . At low energies, some experimental information is available of the capture cascade and by combining this with statistical models at high excitation energies a theoretical model can be developed. This technique has been used for TAC measurements in the past [81]; however, for this work an experimental approach has been taken making use of the high efficiency and good γ -ray energy resolution offered by the TAC. The cascade details (crystals involved in the detection and energy deposited in each of them) are found in list mode by taking measured data at low counting rates (i.e. unaffected by dead-time losses) within a ^{238}U resonance. For this work, the tails of the first 6.7 eV resonance have been used where the count rate is lower than 0.1 count/ μs . This, combined with the dead-time values for the TAC as outlined in Section 3.1.6 and the measured count rate allow the pile-up and dead-time corrections to be accurately corrected for count rates up to 1 count/ μs .

Following Poissonian statistics, the signals from the individual TAC modules are sampled and ordered in time-of-flight depending on the measured count rate. Then, the dead-time is calculated for each signal with respect to those registered at previous times and if the dead-time is larger than the time difference between

the signals, the latter signal is marked as killed, following a paralyzable dead-time model. With enough statistics, an initial value for the dead-time correction is found which depends on the analysis conditions in multiplicity and the deposited energy chosen. The comparison of the number of events registered with and without taking into account the dead-time provides the magnitude of the dead-time losses. After a first iteration, the counting rate distribution used as input is corrected by the dead-time losses and a second iteration, this time with a more realistic counting rate distribution is performed to obtain the final dead-time correction as function of the neutron energy.

After subtracting the beam-off, sample out and neutron scattering backgrounds, these data sets from the different proton pulse intensities differ due to the different magnitudes of dead-time and pile-up present within these data. After applying the correction, these two data sets should agree, which allows this correction model to be validated. Figure 4.7 shows data for different resonances with varying count rates for the two beam intensities before and after the correction is applied.

In all cases it is observed that the recorded experimental counts are affected by dead-time losses, where the effect is larger for MED intensity pulses than LOW intensity pulses. Before the dead-time correction is applied, the two data sets differ in the resonance peaks shown in Figure 4.7 by 3.4%, 6.25% and 8.3%, while the differences after the correction is applied is reduced to only 0.3%, 0.3% and 1.1%, for the 6.7, 20.9 and 66.1 eV resonances respectively. Furthermore, it is observed how the shape of the resonance at 66.1 eV is asymmetric due to dead-time losses as its size in time-of-flight ($\sim 2 \mu\text{s}$) is comparable to the dead-time of the TAC crystals, however the expected symmetric shape is recovered after applying the dead-time correction method.

To minimise the uncertainty associated with this correction, below 1 keV only LOW proton pulse intensity data has been used for the final analysis and the good agreement between LOW and MED pulse intensities over the whole neutron energy range gives confidence that this dead-time and pile-up correction method is accurate within 1%.

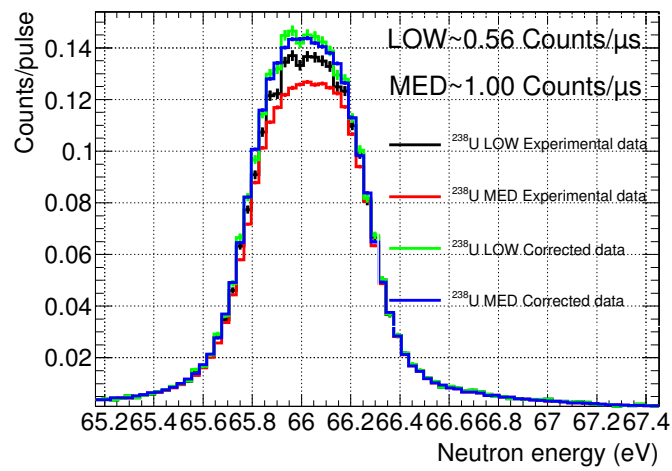
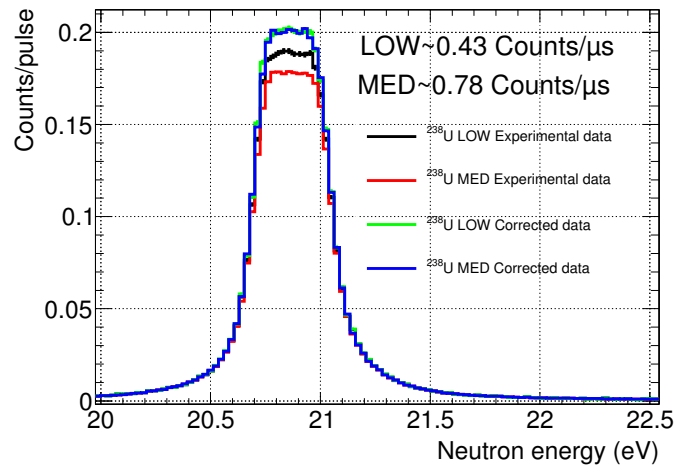
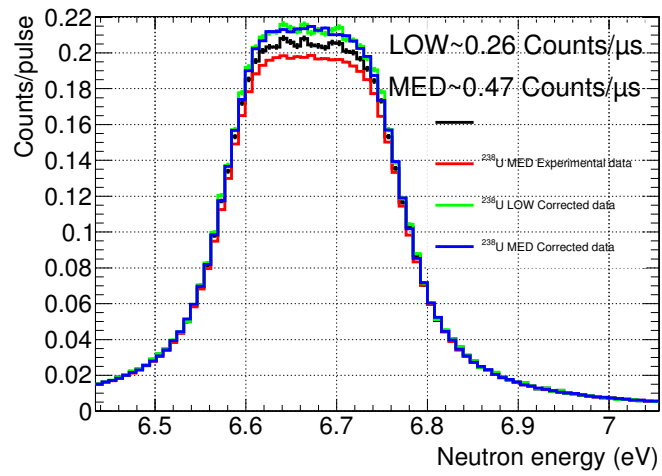


Figure 4.7: Three example resonances (top: 6.7 eV, middle: 20.9 eV, bottom: 66.1 eV) corresponding to different count rates before and after applying the dead-time correction.

4.1.3 Discussion on the high neutron energy limit

In previous TAC actinide measurements, the samples have been encapsulated in for example titanium and large resonances in the sample canning material have limited the upper neutron energy limit to 2 keV [65]. This analysis is the first actinide not to be constrained by such a background, allowing higher neutron energies to be reached. Furthermore, this will be the first analysis performed above 5 keV with the TAC.

There are four factors that determine the high neutron energy limit of this measurement:

1. Structures within the neutron flux.
2. The effect of the γ -flash on the TAC.
3. Pile-up and dead-time effects.
4. Adequate statistics.

The first upper limit is set by the neutron flux, as at certain neutron energies structures within the flux mean it cannot be used to accurately measure the cross section. As discussed in Section 2.2.1, aluminium resonances are present within the neutron flux between 25 and 50 keV (see Figure 4.8), increasing the uncertainty of the yield calculation. Since we aim for a very high accuracy measurement, data are not analysed in the region above 20 keV.

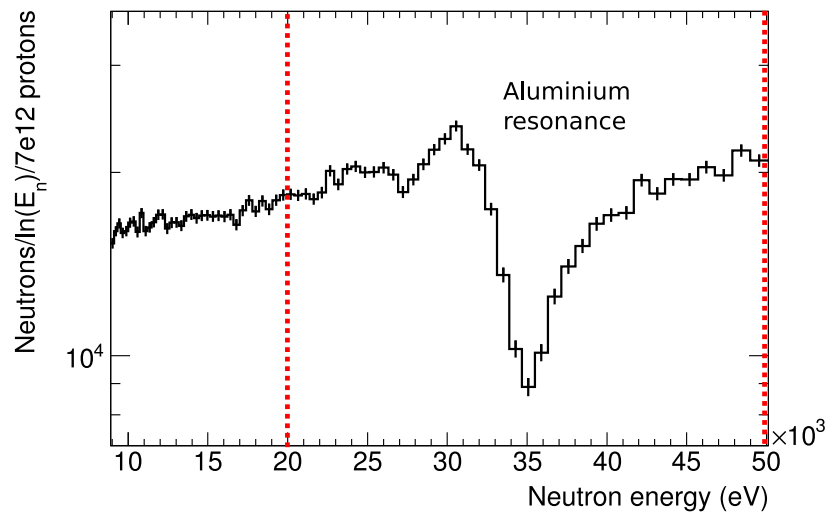


Figure 4.8: The evaluated neutron flux in the energy region 10 to 50 keV highlighting the structures present within this energy region.

The intensity of the γ -flash is proportional to the proton beam intensity, therefore by comparing data sets with different proton beam intensities one can investigate the effect of the γ -flash on the TAC. As well as LOW ($\sim 0.5 \times 10^{12}$ ppp) and MED pulses ($\sim 1.0 \times 10^{12}$ ppp), some data were taken with HIGH pulses ($\sim 3.0 \times 10^{12}$ ppp). It is expected that as one reduces the proton beam intensity, the effect of the γ -flash is also reduced allowing higher neutron energies to be reached. By comparing the background subtracted data at different pulse intensities, we can estimate the energy where the γ -flash starts to affect these data from where these data sets start to deviate.

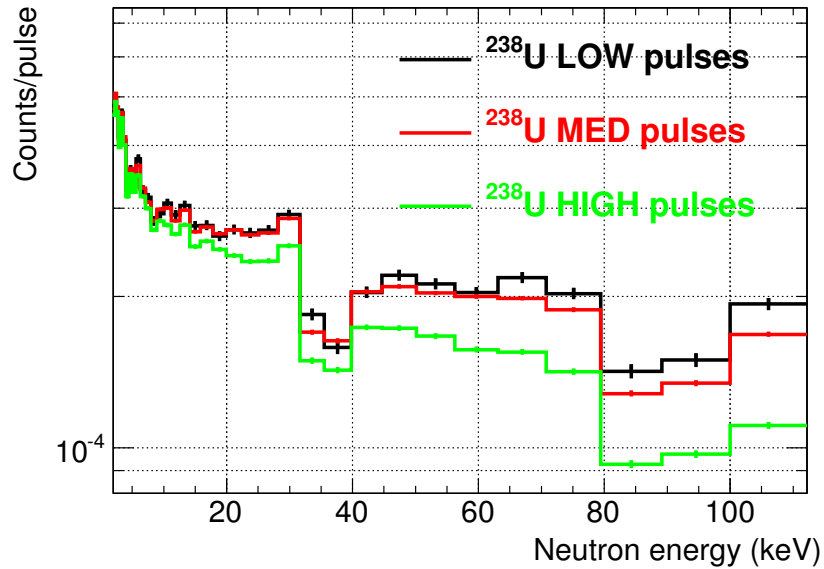


Figure 4.9: ^{238}U neutron spectrum for differing pulse intensities; the points at which these data sets deviate indicate the effect of the γ -flash.

The results shown in Figure 4.9 indicate that data taken with HIGH pulse intensities begins to deviate from that with LOW and MED above 5-10 keV therefore are not used at all in the analysis. The MED data are in perfect agreement with the LOW up to 30 keV above which it seems to differ but not systematically until above ~ 45 keV. To accurately determine the point at which the γ -flash effects these data one must look to the signals in individual crystals, however data displayed in Figure 4.9 gives confidence that the LOW and MED data are certainly unaffected by the γ -flash up to 30 keV, therefore the upper analysis limit in neutron energy is still limited to 20 keV due to the neutron flux. This allows almost all of the most important energy range, as specified in the HPRL (22.6 eV-24.8 keV) to be analysed within this work.

As higher neutron energies are reached, the distance in time-of-flight between

neutrons of increasing energy decreases, so even though the capture cross section diminishes the count rate rises. As illustrated in Figure 4.10, even at very high neutron energies (100 keV) the count rate for MED pulses is still ~ 0.2 counts/ μs therefore the pile-up and dead-time effects are manageable.

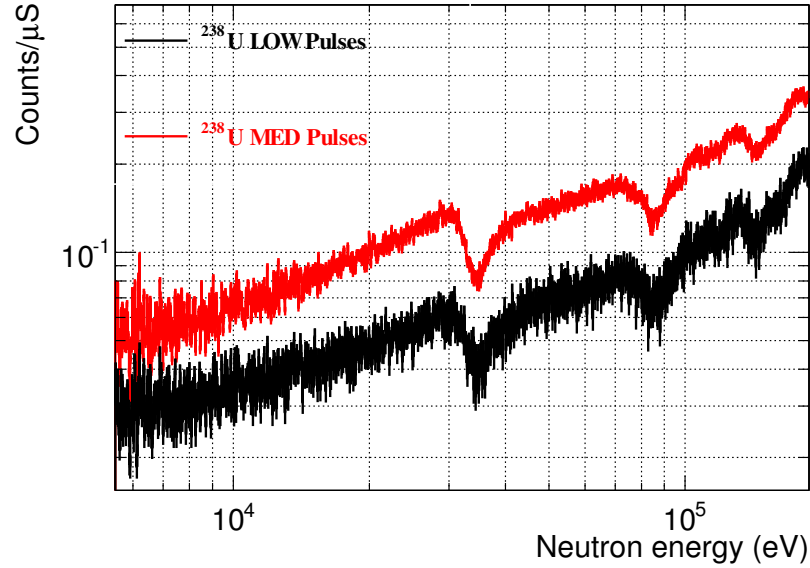


Figure 4.10: ^{238}U counting rate for LOW and MED pulses at high neutron energies.

Finally, the statistics become limiting at higher neutron energies as the capture cross section is lower. To do an accurate resonance analysis with a 2% uncertainty, one requires at least ~ 2500 counts in the resonance. Figure 4.11 displays the total number of counts acquired during the experimental campaign after applying the chosen analysis conditions and subtracting the backgrounds.

Around 500 counts are required in the peak of a resonance for the integral to reach 2500 counts and as illustrated in Figure 4.11 this is the case only below ~ 2.5 keV. The resonances are still well resolved up to ~ 5 keV therefore above this limit the data are rebinned from the current fine binning (10000 bins/decade) which allows individual resonances to be resolved to a much wider binning (20 bins/decade) allowing high statistics to be retained, but not allowing individual resonances to be analysed.

The upper limit in neutron energy of 20 keV has been chosen as we can be confident that the TAC is unaffected by the γ -flash in this energy region and the neutron flux is accurately known. A resonance analysis cannot be performed above 5 keV however above this the yield can be analysed as unresolved providing important information about the cross section in this region.

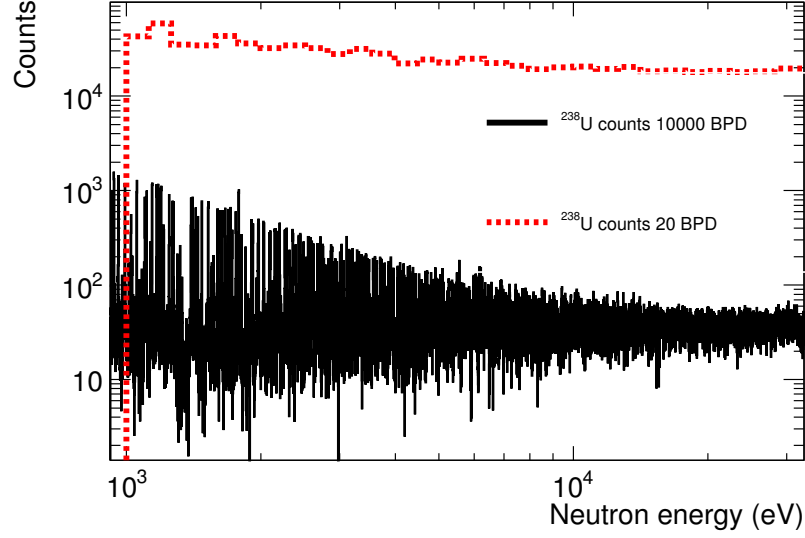


Figure 4.11: ^{238}U total number of counts for the two binnings used for this analysis.

4.1.4 Yield creation using the Saturated Resonance Method

The experimental capture yield is calculated using:

$$Y_{(n,n)}^{meas} = \frac{C(E_n) - B(E_n)}{\varepsilon_{n,\gamma} \cdot N_{BIF} \cdot \phi_n(E_n)} \quad (\text{see Section 1.4.1}). \quad (4.4)$$

The ^{238}U sample used for this measurement was chosen in such a way that in the first three resonances all the neutrons arriving at the sample undergo at least one interaction, thus being saturated at their peaks and allowing the Saturated Resonance Method [80] to be used. This allows the product $\varepsilon_{n,\gamma} \cdot N_{BIF}$ to be accurately determined by comparing the measured yield with the expected one at the saturated region of the first three resonances. The resonance analysis code SAMMY [18] has been used to calculate the expected capture yield from the resonance parameters in the JEFF-3.1.2 library and a fit has been performed leaving only the neutron energy and normalisation value as free parameters. The result for the first 6.7 eV resonance is shown in Figure 4.12.

To accurately find the normalisation value, the resonance was fitted just in the plateau resulting in a better normalisation value as shown in Figure 4.13 where the residuals demonstrate the quality of the fit:

$$\text{Residual} = \frac{DATA - FIT}{\Delta_{statistical}}, \quad (4.5)$$

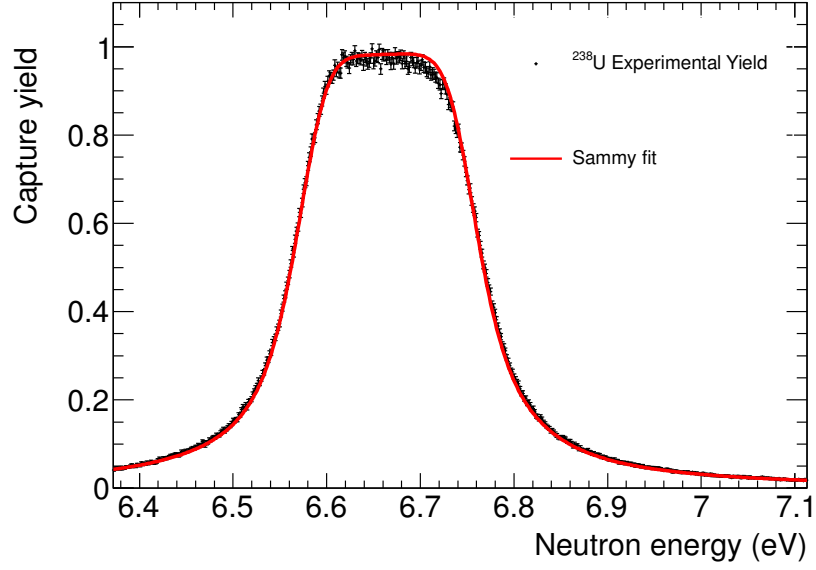


Figure 4.12: The first 6.7 eV saturated ^{238}U resonance as fitted by SAMMY.

where $\Delta_{\text{statistical}}$ is the statistical uncertainty of each data point.

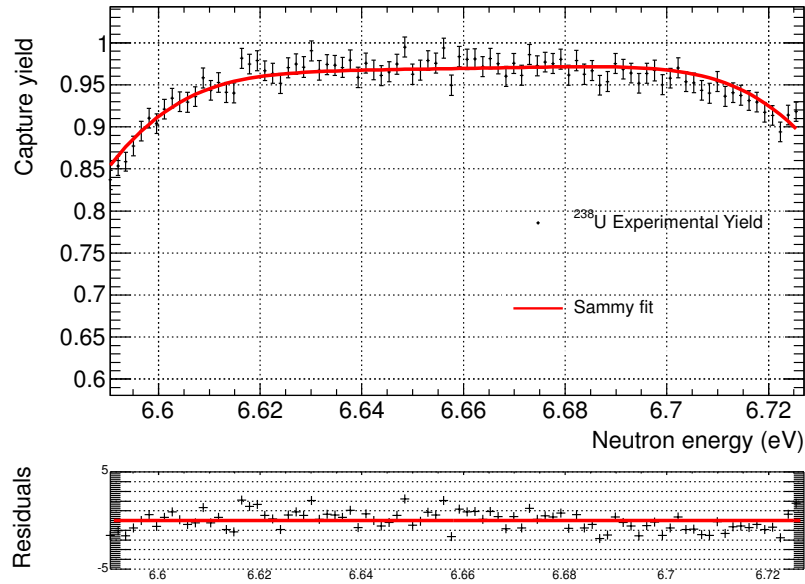


Figure 4.13: The saturated peak of the first 6.7 eV ^{238}U resonance as fitted by SAMMY.

From the first resonance, the product $\varepsilon_{n,\gamma} \cdot N_{BIF}$ was found to be 0.676. Since the ^{238}U sample covers $\sim 97\%$ of the beam this gives a value of $\sim 69.7\%$ efficiency for the analysis conditions $m_{cr} > 1$ and $2.5 < E_{sum}(\text{MeV}) < 5.75$.

The second (20.9 eV) and third (36.7 eV) resonances have a higher scattering

cross section ($\frac{\Gamma_n}{\Gamma_\gamma}=0.06, 0.44$ and 1.46 for the $6.7, 20.9$ and 36.7 eV resonances respectively) and thus a larger multiple scattering correction, which is implemented in SAMMY. However, this correction is not accurate enough to deal with high levels of multiple scattering [82], therefore the resonances are unable to be accurately fitted as illustrated in Figures 4.14 and 4.15.

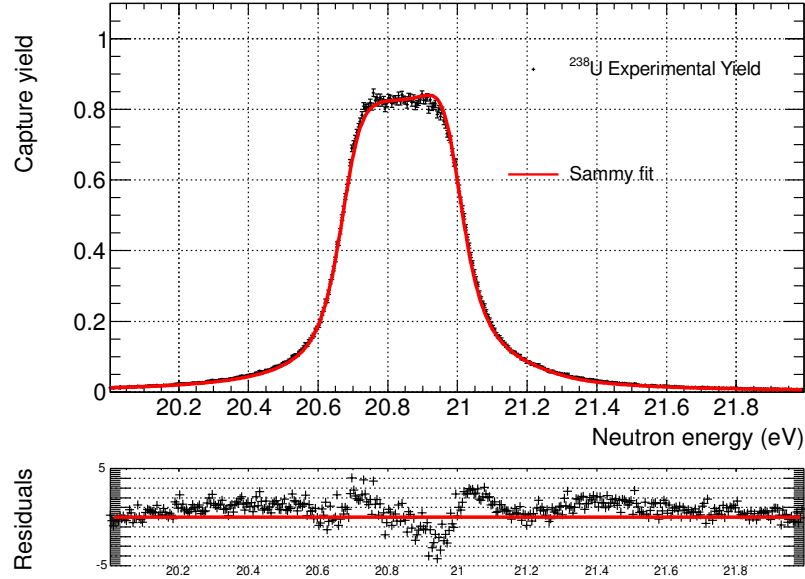


Figure 4.14: The second saturated resonance of ²³⁸U as fitted by SAMMY, where the normalisation has been taken from the first resonance and only the neutron energy has been left as a free parameter within the fit.

Although the second and third saturated resonance peaks are unable to be fitted due to the multiple scattering contribution, a good agreement between these data and the fit is seen in the tails of the resonances and at the general height of the resonance if the normalisation is taken from the fit to the first resonance. In fact, the normalisation calculated from the three resonances agree within 1% suggesting that this is the level of the uncertainty in the normalisation ($\varepsilon_{n,\gamma} \cdot N_{BIF}$).

The normalisation is a crucial point in any cross section measurement and the possibility to self normalise using the Saturated Resonance Method means that several sources of uncertainty are kept to a minimum. In particular, the saturated resonance method allows the product $\varepsilon_{n,\gamma} \cdot N_{BIF}$ to be experimentally determined, instead of determining them individually from auxiliary measurements (for the N_{BIF}) and Monte Carlo simulations (for $\varepsilon_{n,\gamma}$). This method has the final advantage over others in that any error due to sample alignment is eliminated.

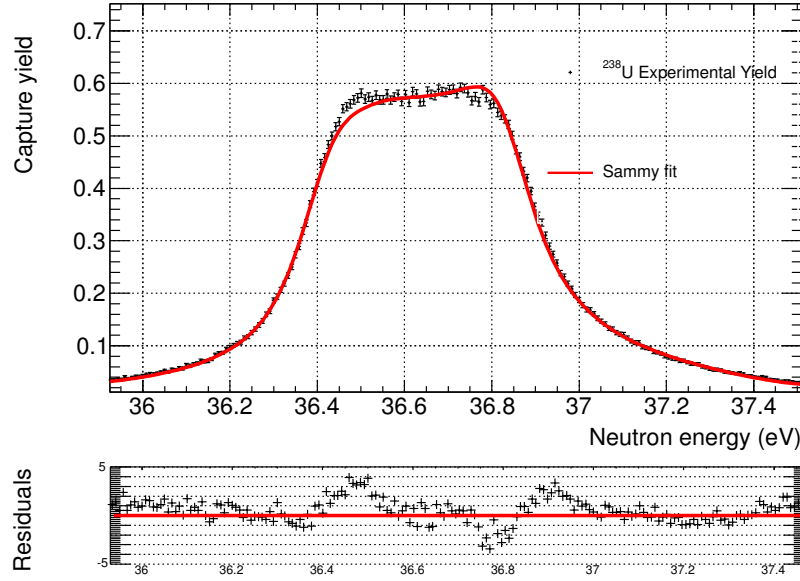


Figure 4.15: The third saturated resonance of ^{238}U as fitted by SAMMY, where the normalisation has been taken from the first resonance and only the neutron energy has been left as a free parameter within the fit.

4.1.5 Uncertainties

The sources of uncertainty discussed during the calculation of the experimental capture yield are related to the beam-on and beam-off background subtraction, the neutron scattering background subtraction, the pile-up and dead-time correction, the normalisation, variation of the beam interception factor as a function of neutron energy (which is negligible for this experiment because N_{BIF} is 97%) and the n_TOF neutron flux. Furthermore, any uncertainty in the sample mass will propagate to the resulting cross section calculation. These sources have been discussed in their relevant sections, therefore Table 4.2 is a summary of all the sources of systematic uncertainties and their associated sections within this manuscript.

Table 4.2: Summary of all the uncertainties related to the experimental ^{238}U capture yield.

Source of uncertainty	Uncertainty		Reference
	$E_n < 5$ keV	5-20 keV	
Sample mass	0.03%		Section 2.4.1
Neutron flux (shape in E_n)	1-2%	2-3%	Section 2.2.1
Normalisation ($\varepsilon_{n,\gamma} \cdot N_{BIF}$)	1%		Section 2.2.1
Dead-time and pile-up	0-1%	0%	Section 4.1.2
Neutron scattering	0-2%	2%	Section 4.1.1
Other background subtraction	Negligible		Section 4.1.1
Overall	1.4-2.2%	3.0-3.7%	

Overall, the systematic error of the neutron capture yield resulting in this work is at the limit of the aimed 2% (1.4-2.2%) in the neutron energy region below 5 keV and slightly above this (3.0-3.7%) in the high energy region between 5 and 20 keV. The latter is higher because of the larger neutron scattering background as neutron energy increases combined with the larger uncertainty in the shape of the n.TOF neutron flux in the keV region. Indeed, the uncertainty in the resolved resonance region (<5 keV) drastically varies from resonance to resonance as the dominant sources of uncertainty is from the dead-time and pile-up correction and the neutron scattering background.

4.2 ^{238}U Cross section analysis

4.2.1 Resonance analysis below 5 keV

Before analysing the individual resonances, the experimental capture yield may still contain a residual background which has not been subtracted yet. The R-matrix resonance analysis code SAMMY provides an independent value for the background which can be found by performing a fit in the valleys between resonances. Two additional background components were found, as shown in Figure 4.16 which has been found to follow a function of the type $a + \frac{b}{\sqrt{E_n}}$.

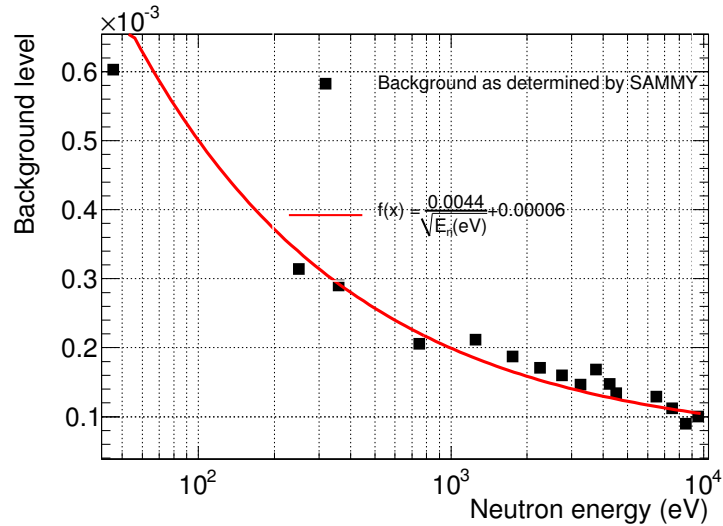


Figure 4.16: The remaining background levels found in the valleys between ^{238}U resonances as fitted by SAMMY.

The background follows the function (see Figure 4.16):

$$f(E_n) = \frac{0.0044}{\sqrt{E_n(\text{eV})}} + 0.00006. \quad (4.6)$$

Within the resolved resonance region (below 5 keV), this corresponds to less than 1% of the capture yield in the resonances and up to 10% in the valleys and within the unresolved resonance region (5-20 keV) this corresponds to between 10-17%.

The resonances were analysed in groups of ~ 20 leaving Γ_n , Γ_γ and E_n as free parameters and taking as initial parameters those found in the JEFF-3.2.1 evaluation. Some resonances required an adjustment of the initial parameters before a good fit could be obtained and some resonances were unable to be fitted due to the limitation of SAMMY to model strong multiple scattering effects. The resulting fits and residuals are shown in Figures 4.17-4.30, while the discussion of the results is given in Section 4.3.1.

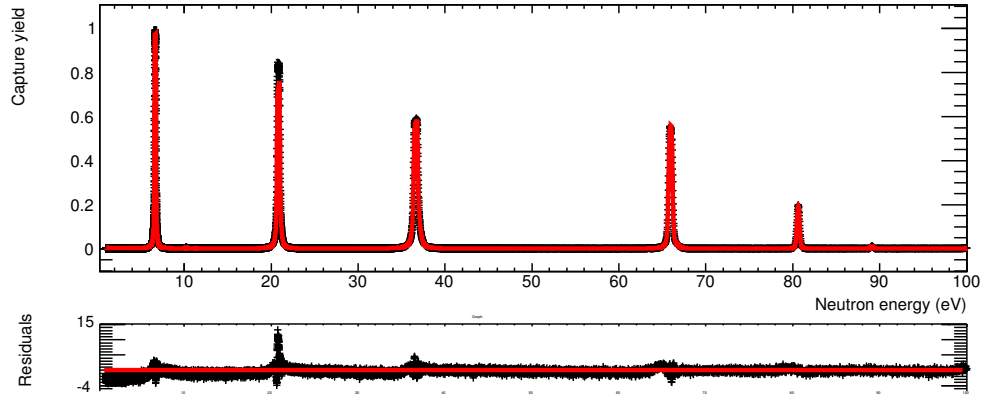


Figure 4.17: SAMMY fits (red) to experimental data (black) in the neutron energy interval 1-100 eV.

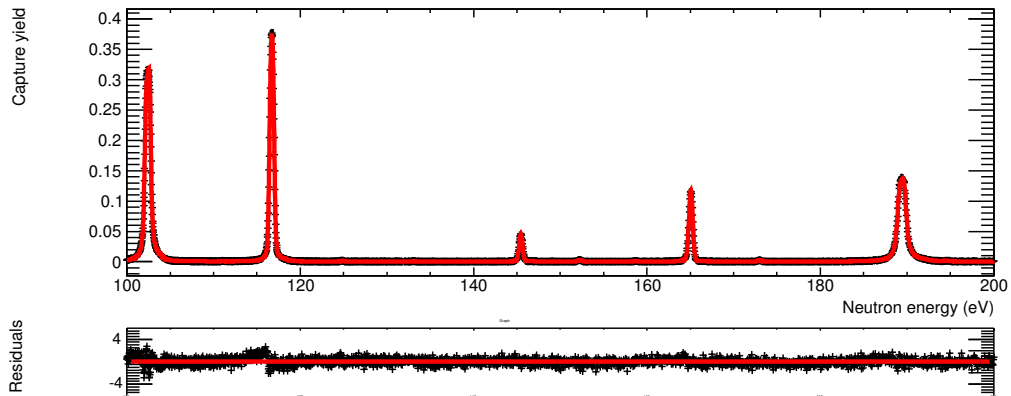


Figure 4.18: SAMMY (red) to experimental data (black) fits in the neutron energy interval 100-200 eV.

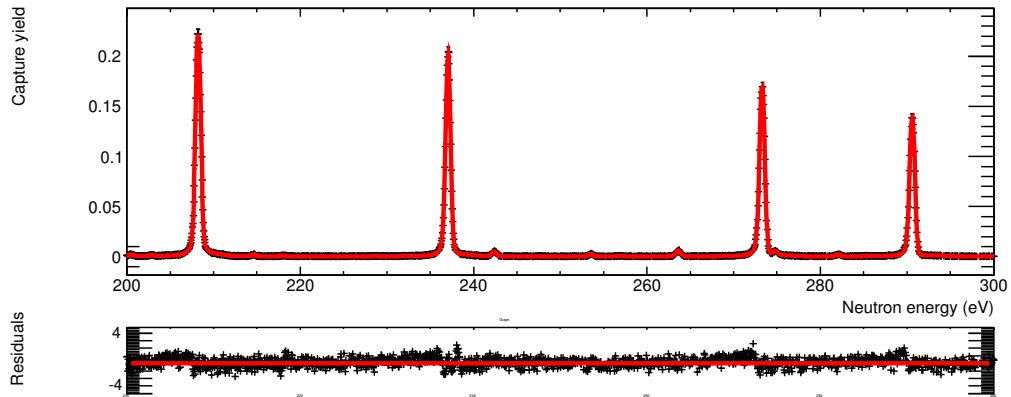


Figure 4.19: SAMMY (red) to experimental data (black) fits in the neutron energy interval 200-300 eV.

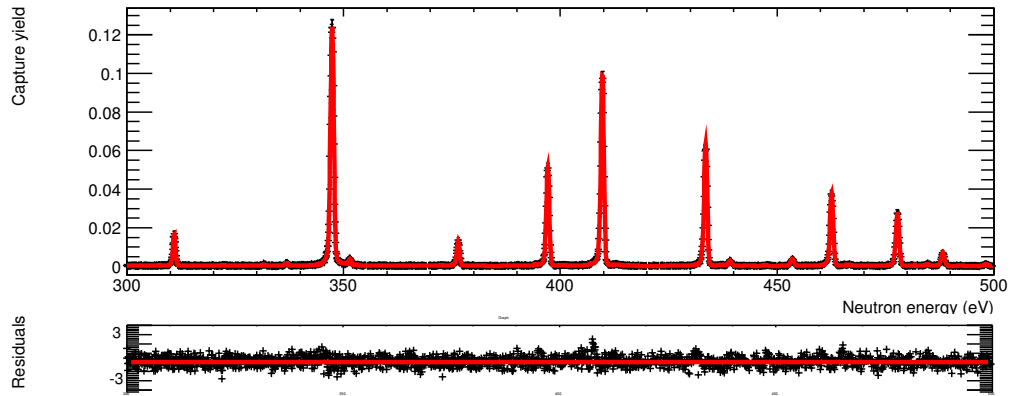


Figure 4.20: SAMMY (red) to experimental data (black) fits in the neutron energy interval 300-500 eV.

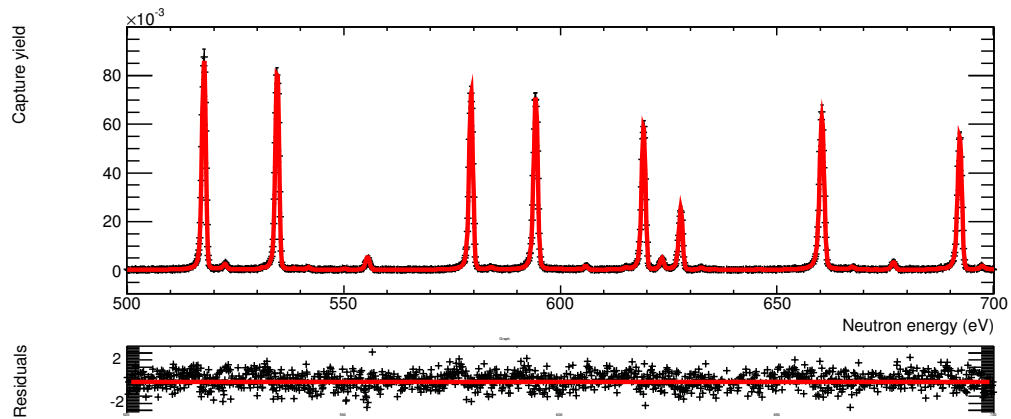


Figure 4.21: SAMMY fits (red) to experimental data (black) in the neutron energy interval 500-700 eV.

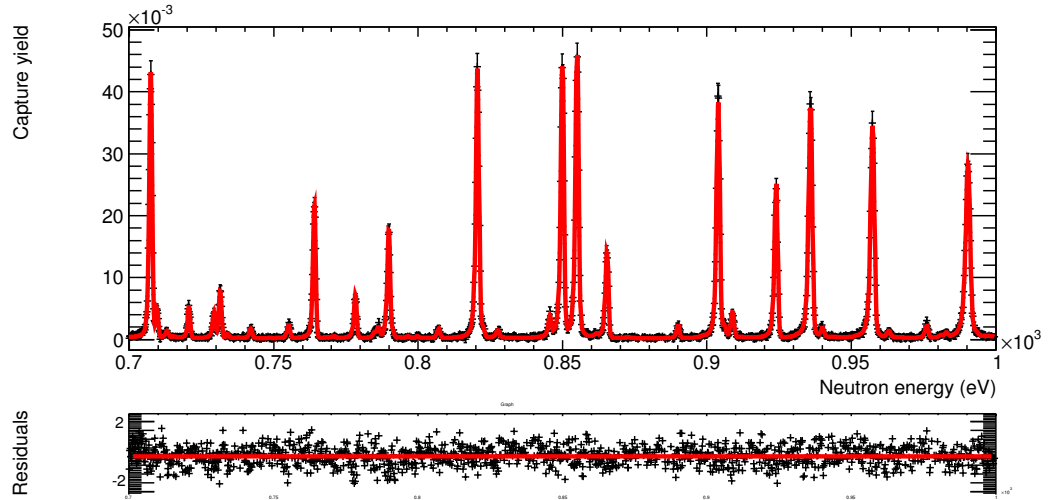


Figure 4.22: SAMMY fits (red) to experimental data (black) in the neutron energy interval 700-1000 eV.

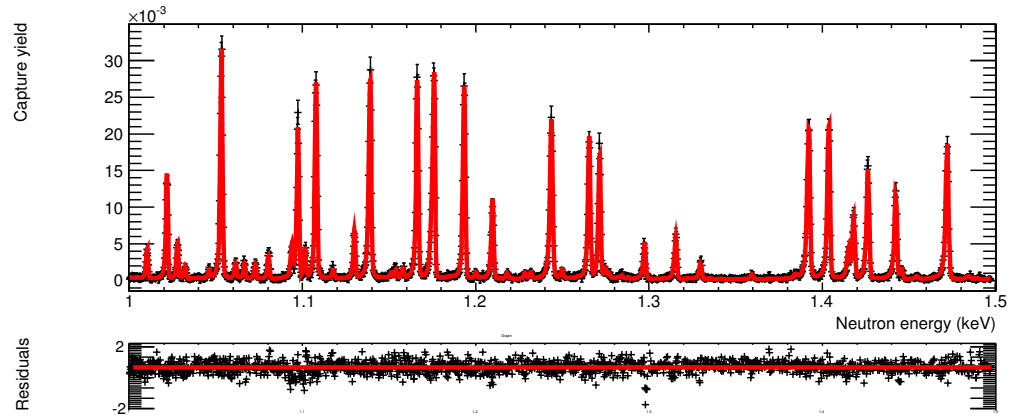


Figure 4.23: SAMMY fits (red) to experimental data (black) in the neutron energy interval 1-1.5 keV.

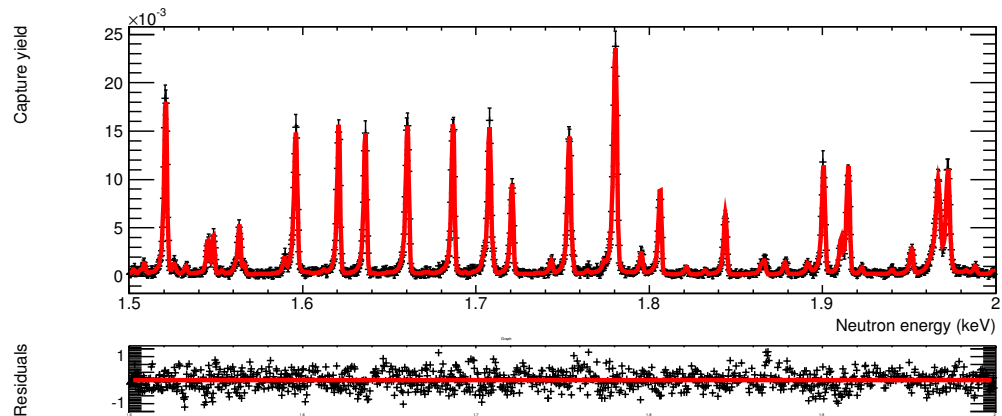


Figure 4.24: SAMMY fits (red) to experimental data (black) in the neutron energy interval 1.5-2 keV.

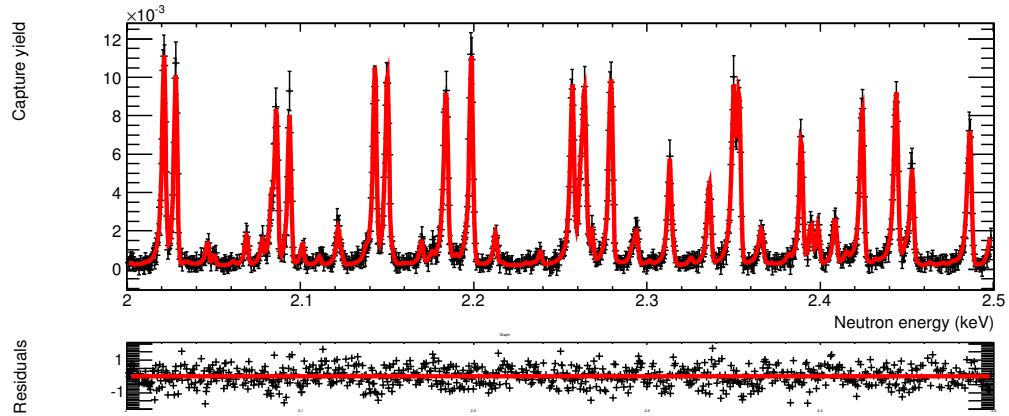


Figure 4.25: SAMMY fits (red) to experimental data (black) in the neutron energy interval 2-2.5 keV.

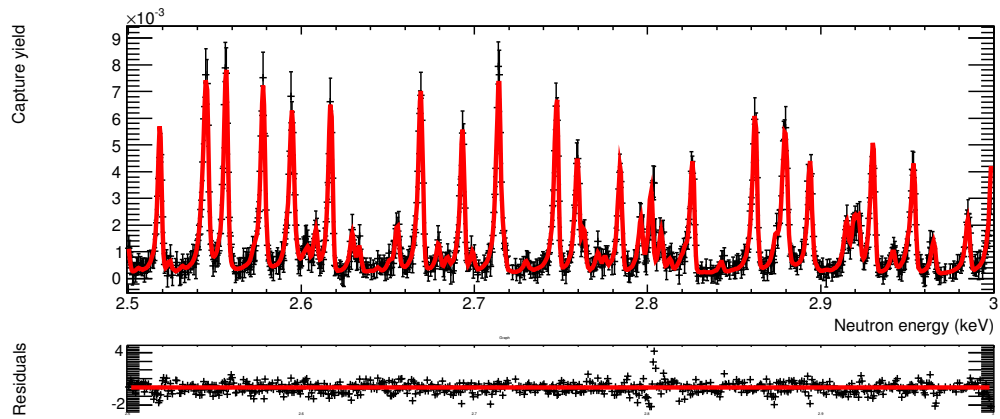


Figure 4.26: SAMMY fits (red) to experimental data (black) in the neutron energy interval 2.5-3 keV.

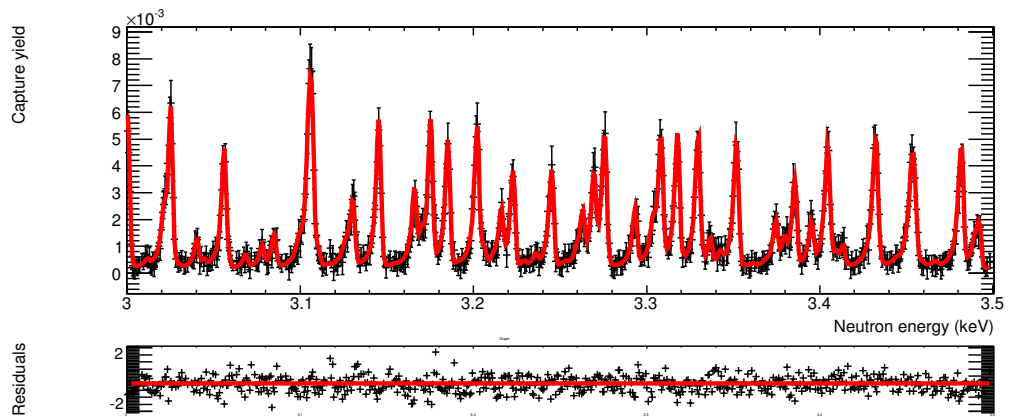


Figure 4.27: SAMMY fits (red) to experimental data (black) in the neutron energy interval 3-3.5 keV.

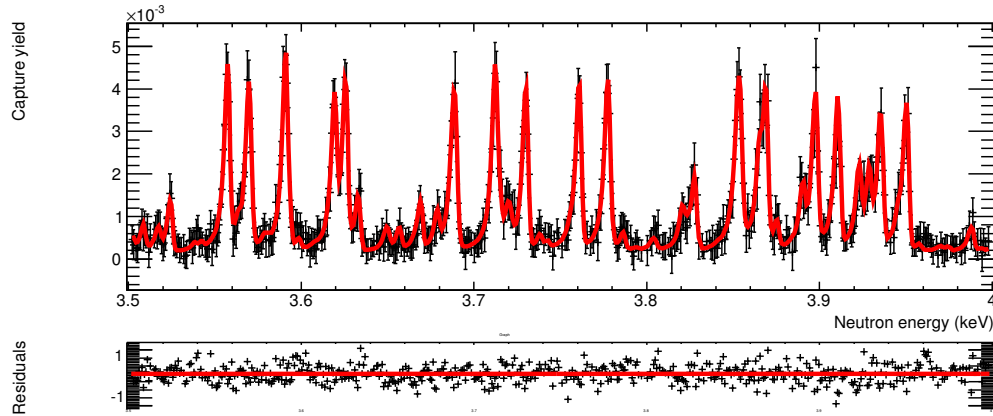


Figure 4.28: SAMMY fits (red) to experimental data (black) in the neutron energy interval 3.5-4 keV.

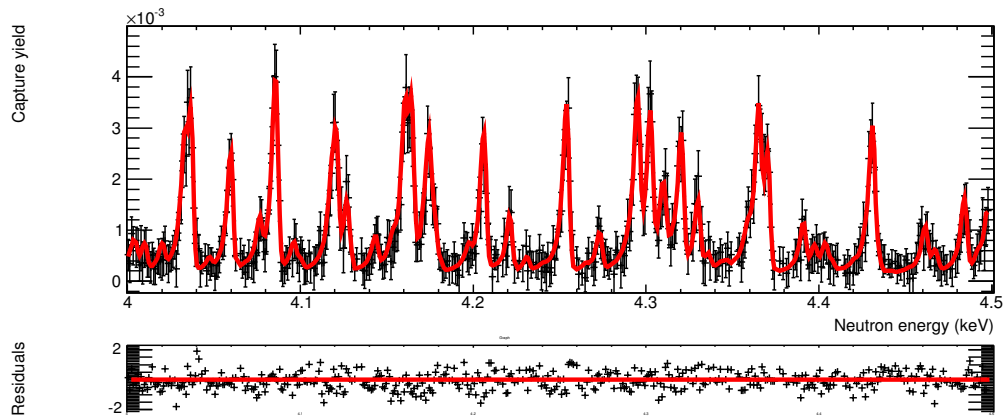


Figure 4.29: SAMMY fits (red) to experimental data (black) in the neutron energy interval 4-4.5 keV.

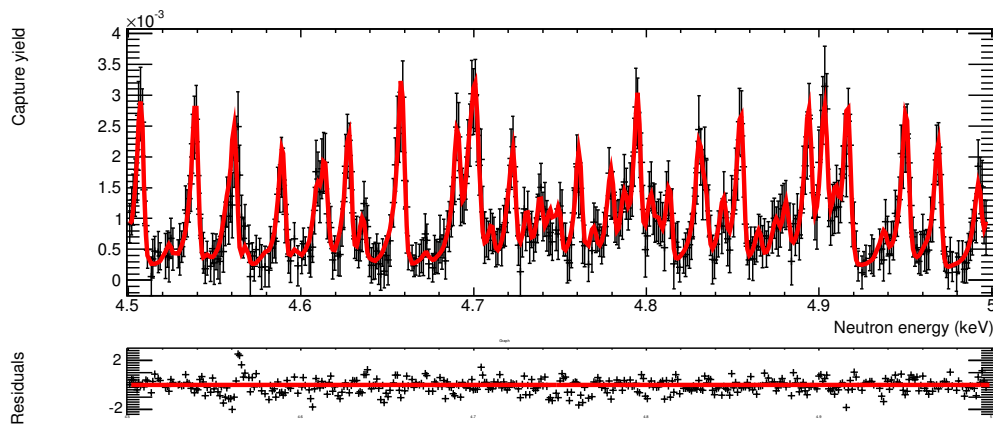


Figure 4.30: SAMMY fits (red) to experimental data (black) in the neutron energy interval 4.5-5 keV.

Table 4.3: ^{238}U resonance parameters from the performed SAMMY fits and the JEFF-3.1.2 and ENDF/B-VII.1 libraries. The first three resonances (marked with *) were saturated, thus could not be correctly fitted.

Energy eV	n_TOF TAC		JEFF-3.1.2		ENDF/B-VII.1	
	Γ_γ meV	Γ_n meV	Γ_γ meV	Γ_n meV	Γ_γ meV	Γ_n meV
6.67*	20.389	1.618	23.000	1.476	23.000	1.476
20.86*	16.597	13.228	22.910	10.071	22.864	10.094
36.67*	22.877	34.410	22.890	33.554	23.002	33.546
66.02	23.177	25.241	23.360	24.235	23.308	24.178
80.74	29.626	1.840	23.000	1.877	23.387	1.874
102.54	23.250	73.655	23.420	71.030	24.082	70.771
116.88	19.829	29.101	22.990	25.338	22.276	25.354
145.66	29.243	0.910	23.528	0.885	23.825	0.886
165.29	32.983	3.225	24.066	3.199	24.374	3.190
189.66	21.285	177.238	23.557	170.351	23.580	170.185
208.51	20.898	58.086	22.906	49.939	22.835	49.882
237.39	19.487	40.834	25.376	26.452	25.178	26.448
273.67	18.490	34.935	23.100	24.726	24.408	24.865
291.01	16.094	25.231	22.430	16.624	23.226	16.544
311.34	25.594	1.069	23.000	1.049	23.494	1.056
347.85	20.055	87.497	21.984	80.012	21.815	79.297
353.74	23.026	0.022	23.000	0.022	23.001	0.022
376.97	23.544	1.123	23.000	1.118	23.335	1.116
397.67	25.327	6.049	23.000	5.774	22.574	5.802
410.29	22.146	21.398	23.180	19.313	22.507	19.482
434.13	25.554	9.744	22.886	9.807	23.298	9.824
463.25	25.912	5.526	23.000	5.472	23.779	5.446
478.50	24.976	3.954	23.000	3.985	24.439	3.956
488.93	23.363	0.932	23.000	0.863	23.383	0.863
518.46	21.126	63.037	22.271	49.828	22.068	49.719
535.40	20.738	53.359	24.218	44.788	23.985	44.651
580.22	21.241	50.428	22.514	40.665	22.303	40.570
595.17	21.148	95.178	23.010	87.134	23.010	87.134
620.10	20.870	30.363	23.080	30.575	22.860	30.356
628.68	22.757	6.322	23.000	6.714	23.000	6.591
661.33	23.019	140.168	24.370	127.151	24.155	126.598
693.20	21.008	44.961	23.033	42.365	22.828	42.353
708.42	21.607	21.584	23.289	22.196	23.284	21.995
721.70	22.758	1.317	23.000	1.475	3.150	1.965
730.28	22.941	1.052	23.000	1.027	23.000	1.053
765.19	22.563	8.096	23.000	8.923	23.000	8.928
790.95	22.481	6.529	23.000	6.694	23.000	6.743
821.74	19.972	76.103	22.280	68.386	22.080	67.593
851.17	21.551	67.965	23.379	65.291	23.534	66.473
856.28	21.568	94.979	23.197	90.531	23.275	90.952
866.63	22.542	5.801	23.000	5.973	23.000	5.973
905.23	21.792	50.760	23.000	54.654	23.738	55.768
925.31	23.468	16.113	23.000	16.717	23.000	15.780
937.25	21.360	158.293	23.660	157.788	23.681	155.920
958.76	21.078	188.362	22.862	213.125	23.181	212.978
991.86	22.450	396.893	24.204	394.941	24.223	394.718

Notes: Although Γ_n is not directly measured, this quantity is still an output from the SAMMY fit.

4.2.2 Analysis above 5 keV

Above 5 keV these data are rebinned to 20 bins/decade and it is no longer possible to obtain information on individual resonances, just the overall magnitude of the yield however the statistical uncertainty is less than 1% (See Figure 4.11). A comparison of the yields that will be used below and above 5 keV is given in Figure 4.31 where one observes all structure is lost above ~ 7 keV resulting in a smooth cross section.

At these high energies and given the low value of the capture yield one can apply the thin target approximation ($\sigma_{n,\gamma} = \frac{Y_{n,\gamma}}{n(\text{atoms/barn})}$) and thus calculate the point-wise cross section from the measured yield. The comparison of the measured cross section with the evaluated cross sections is given in Section 4.3.2.

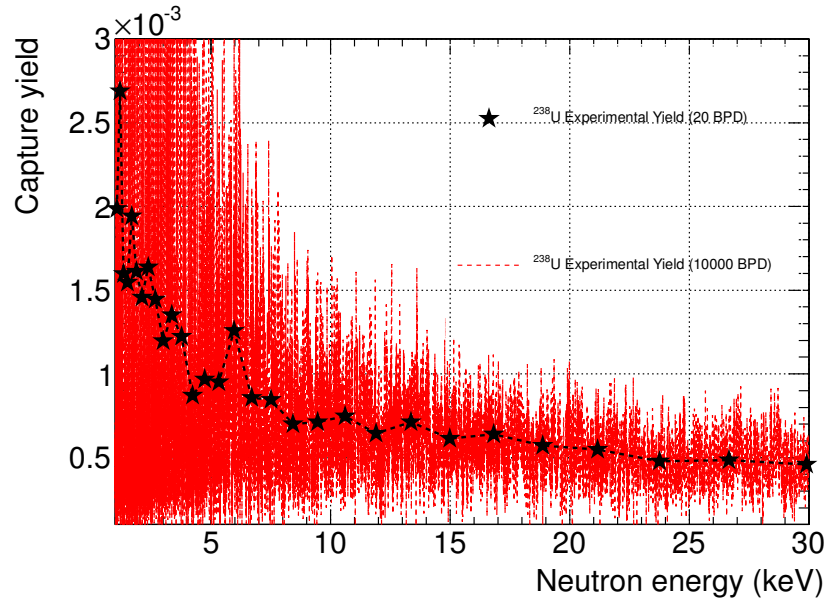


Figure 4.31: Experimental data for 20 bins/decade (black) and 10000 Bins/decade (red) in the neutron energy interval 1-30 keV.

4.3 Results for the $^{238}\text{U}(n,\gamma)$ cross section

In the neutron energy region below 5 keV, we have a set of resonance parameters (found in full in Appendix A and up to 1 keV in Table 4.3) which can be compared to the evaluated data. The resonance kernel, defined in Equation 4.2, is a representation of the resonance strength which is used to compare these measured data with other results. Above 5 keV, we have a point-wise cross section (thin target approximation) which can be directly compared to the evaluated cross section. As

outlined in Section 1.6 all the evaluated libraries contain very similar data sets for the ^{238}U capture cross section with only minor differences occurring between them, thus for this work a comparison has been performed between only the JEFF-3.1.2 and ENDF/B-VII.1 libraries.

4.3.1 Comparison and discussion with resolved resonance evaluated data below 5 keV

The resonance kernels are calculated from the SAMMY fits and then compared between JEFF-3.1.2 and ENDF/B-VII.1 by calculating the corresponding ratios. In Figure 4.32 one sees the agreement is always within 10%, except for seven resonances which are $\sim 12\%$ higher in the evaluations and one resonance at 1.211 keV where the fitted kernel disagrees with the ENDF/B-VII.1 by $\sim 60\%$, however is in general good agreement with the JEFF-3.1.2 value. This is because the ENDF/B-VII.1 evaluation considers this resonance to have a small capture width ($\Gamma_\gamma = 6.6$ meV) whereas this is not the case in JEFF-3.1.2 ($\Gamma_\gamma = 17.6$ meV). Figure 4.33 illustrates the kernel ratios disregarding this one resonance, where the two dotted lines at 0.9 and 1.1 illustrate how the agreement between resonance kernels almost always is within 10%.

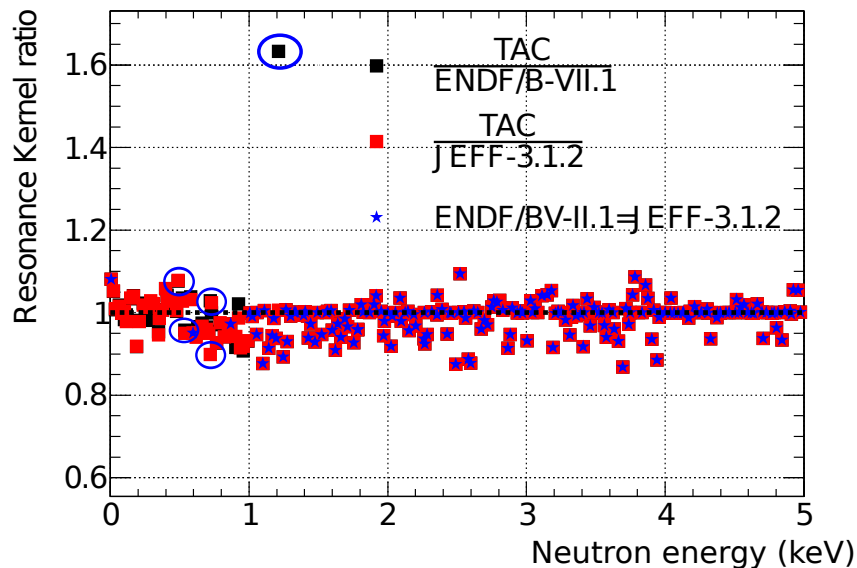


Figure 4.32: Ratios of all resonance kernels below 5 keV from the SAMMY fits and the ENDF/B-VII.1 and JEFF-3.1.2 libraries, where the starred points represent resonances where the kernels are the same in both evaluated libraries. The SAMMY fits to the resonances circled in blue are shown in Figure 4.34

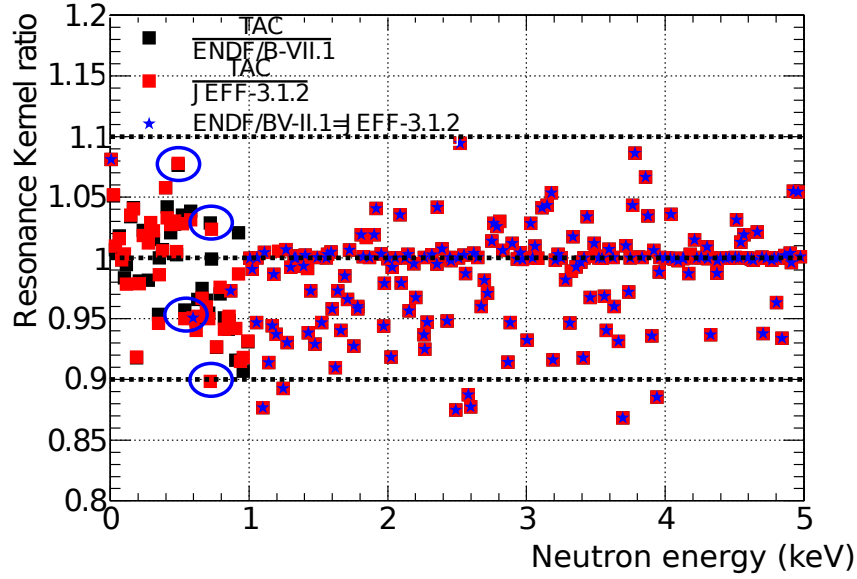


Figure 4.33: Ratios of all resonance kernels below 5 keV from the SAMMY fits and the ENDF/B-VII.1 and JEFF-3.1.2 libraries, where the starred points represent resonances where the kernels are the same in both evaluated libraries excluding the 1211 eV resonance. The SAMMY fits to the resonances circled in blue are shown in Figure 4.34

As an illustrative example, some resonances (circled in Figures 4.32 and 4.33) where our data differ from the evaluations are shown in Figure 4.34. In the upper left panel of Figure 4.34, the TAC data for these particular resonances are above (8%) the evaluated libraries, in the upper right, it is below (5%) the evaluated libraries, in the lower left it is between the evaluated (10% below JEFF-3.1.2, 3% above ENDF/B-VII.1) libraries and in the lower right it is in good agreement with the JEFF-3.1.2 evaluation but above ENDF/B-VII.1 (63%).

In the resonance region, it is evident that significant differences are seen for certain resonances between the TAC data and the evaluated libraries. By projecting the value of the resonance kernel ratios onto the y-axis, a Gaussian distribution has been fitted to estimate the mean and spread of ratios compared to the libraries. These projections are shown for various neutron energy regions in Figure 4.35. This method of comparison takes all resonances into account, regardless of their strength. In the latter part of this section, similar projections are made for these ratios weighted by their strength.

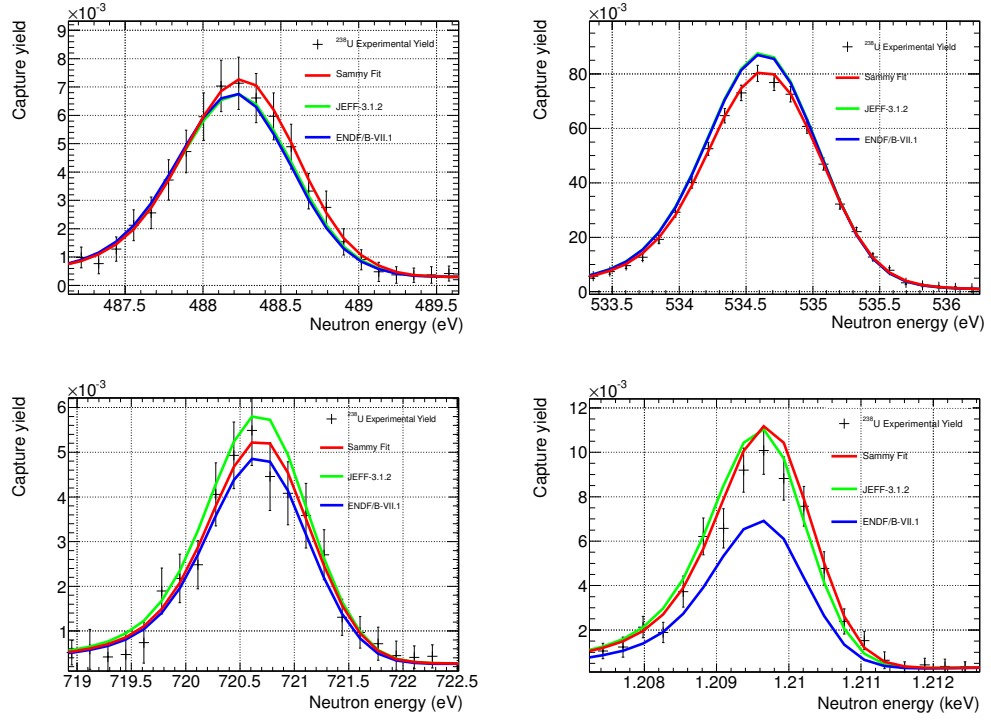


Figure 4.34: Experimental data (black) and fits (red) for four example resonances compared to the ENDF/B-VII.1 (blue) and JEFF-3.1.2 (green) libraries.

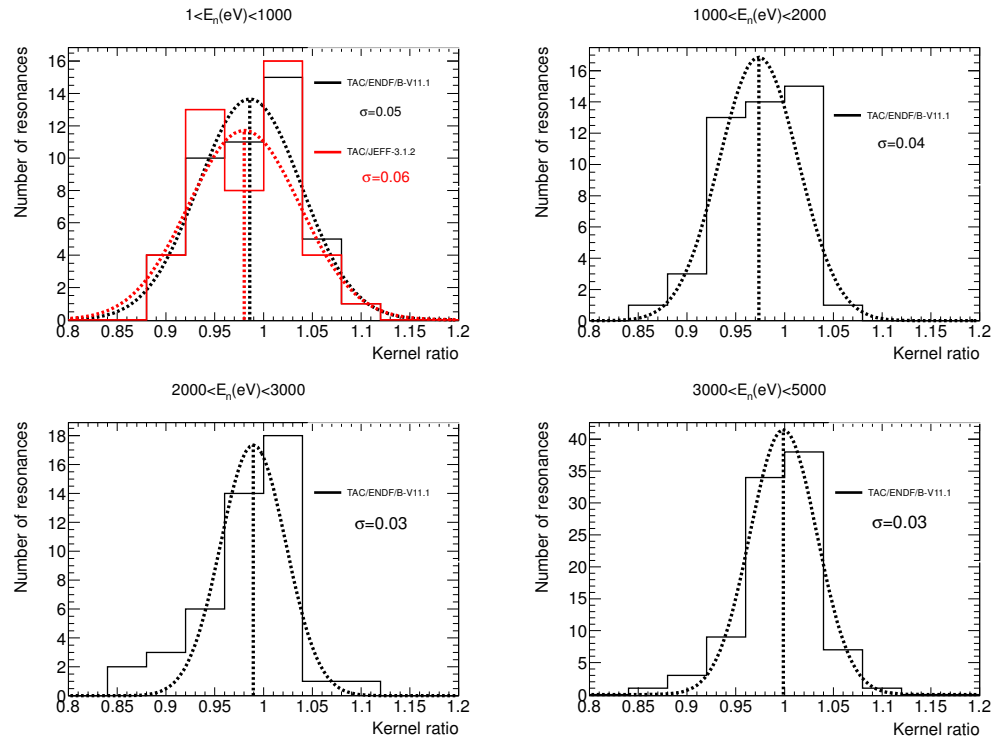


Figure 4.35: Projections of the resonance kernel ratios between TAC data and the ENDF/B-VII.1 and JEFF-3.1.2 libraries for different energy regions. Above 1 keV the two libraries are equal therefore just one projection is shown.

It is observed that below 1 keV, the TAC resonance strengths are $\sim 2\%$ lower on average than that found in JEFF-3.1.2 and $\sim 1\%$ lower than that found in ENDF/B-VII.1. Above 1 keV, where both the JEFF-3.1.2 and ENDF/B-VII.1 contain the same resonance parameters, these TAC resonance strengths are around 3% lower between 1 and 2 keV, around 1% lower between 3 and 4 keV and finally in good agreement between 4 and 5 keV. These differences shall be considered in the light of the accuracy of the present measurement which on average is 1.8% in this energy region.

To investigate the differences between data and evaluations highlighted, possible sources of systematic uncertainties are investigated. In the resolved resonance region, it has been shown that if the multiple scattering contribution is very large, SAMMY is unable to correctly fit the resonances (see for example Figure 4.14). Since for heavy elements such as ^{238}U the capture width remains relatively constant for all resonances, the resonance strength increases with the scattering width of the resonance therefore the resonance kernel ratios are plotted as a function of this (the resonance kernel) as shown in Figure 4.36.

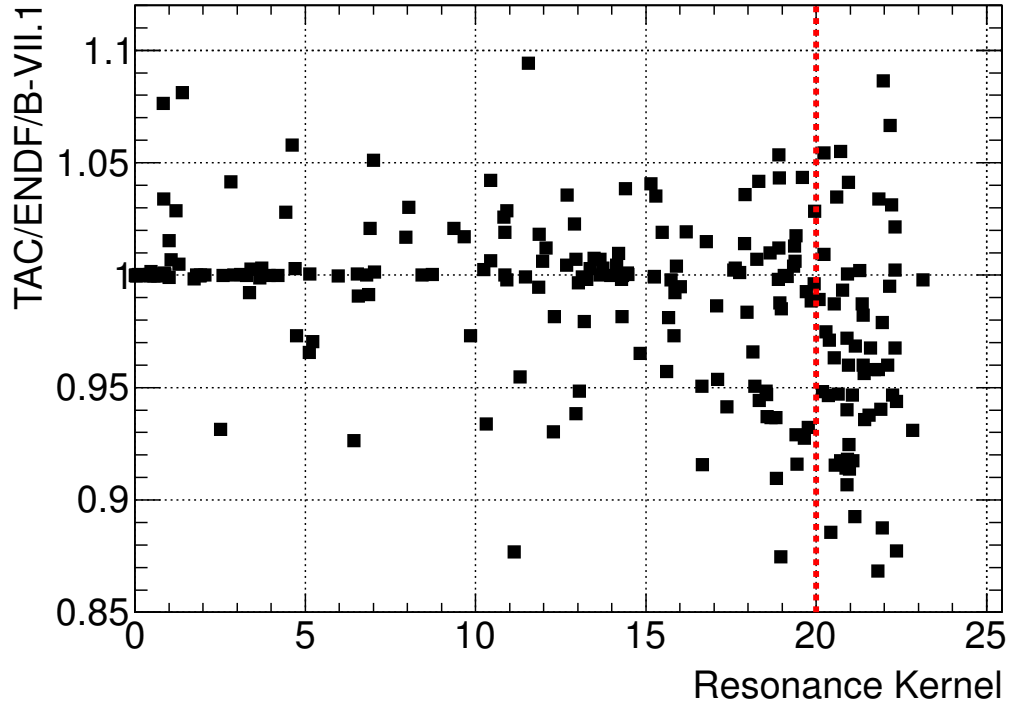


Figure 4.36: Kernel ratios as a function of the resonance kernel.

As illustrated in Figure 4.36 it seems there is could be some systematic trend at high resonance kernel values for the TAC data to fall below that in the evaluations. To quantify this, projections are made in two regions: low kernel values ($\text{RK} < 20$

meV) and high kernel values ($\text{RK} > 20$ meV).

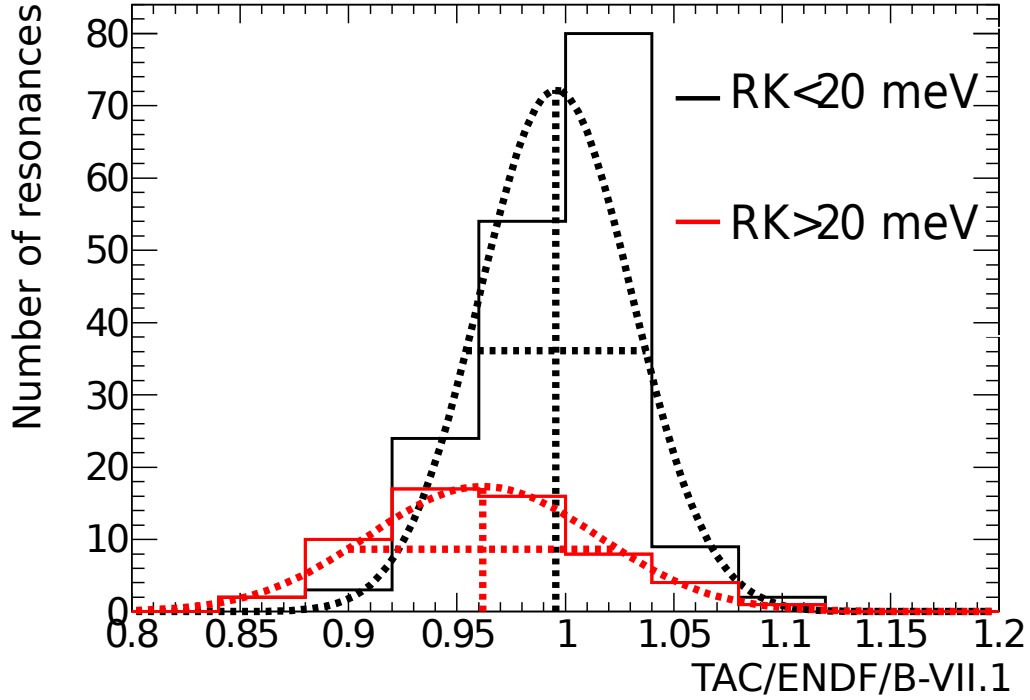


Figure 4.37: Projections of the TAC/evaluated resonance kernels for two regions: weak and strong resonances. The dashed lines represent Gaussian fits to the data and the horizontal lines are the full width at half maximum.

For the 174 resonances with a resonance kernel < 20 meV, excellent agreement is seen between the TAC data and that in the evaluated libraries (the resulting Gaussian fit has a mean of 0.996 and $\sigma = 0.035$), however for the 58 stronger resonances with a kernel > 20 , TAC data are on average 4% below the evaluated data (the resulting Gaussian fit has a mean of 0.962 and $\sigma = 0.053$). This suggests that there may be some systematic effect in the analysis of strong resonances in either our data or in the evaluations. The evaluations use capture data from samples with more than three times thickness than the sample used within this work, thus multiple scattering effects should be larger in the capture data used within the evaluations. This should be clarified when the TAC data are compared to the other new measurements within the ANDES project (not available yet). Until this is clarified, we consider the results from this analysis very accurate ($\sim 2\%$) when the resonance kernel is below 20, however a larger uncertainty ($> 2\%$) is assigned when the resonance kernel is above 20. Although these results confirm the excellent quality of the evaluations, it is noted that many measured resonances differ slightly which is expected due to the 3% uncertainty assigned to the capture cross

section in this energy region. These new results, in combination with previous and current measurements will help to reduce the cross section uncertainty moving closer to the 1% required by industry within this neutron energy region.

4.3.2 Comparison and discussion with unresolved resonance evaluated data

The evaluated cross sections can be directly compared to the capture yield at higher neutron energies, where the cross section is lower. As the product $n(\text{atoms/barn}) \cdot \sigma_{n,tot}(\text{barn})$ is very low, self shielding effects can be ignored and the thin target approximation can be applied ($Y_{n,\gamma}(E_n) \approx n\sigma_\gamma(E_n)$) therefore by multiplying the point-wise cross section by the atomic density of the ^{238}U sample these data sets can be compared (see Section 1.4.1 and Equation 1.6). In Figure 4.38 the capture yield is compared with the most recent versions of the JEFF (JEFF-3.1.2) and ENDF/B (ENDF/B-VII.1) libraries.

From Table 1.2 it is seen that there are three energy regions of interest to industry: 22.6-454 eV, 2.03-9.12 keV and 9.12-24.8 keV. In the present work the first region has been fully analysed in terms of individual resonances, while the latter two regions (up to a maximum neutron energy of 20 keV) are discussed in terms of point-wise and averaged cross section.

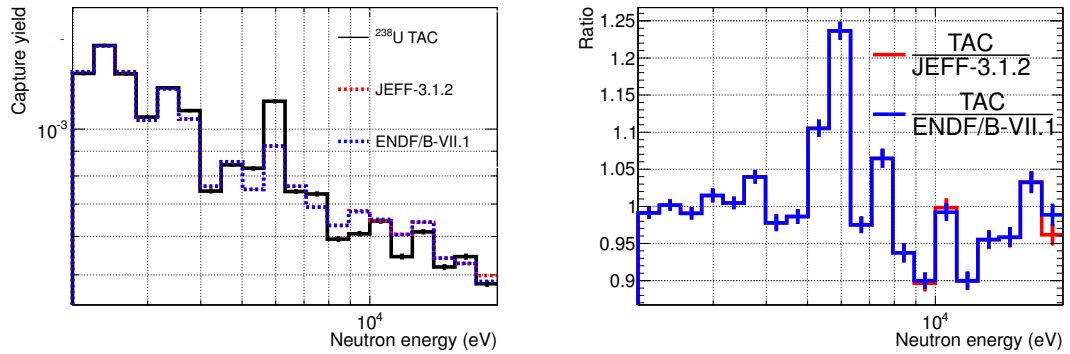


Figure 4.38: Unresolved resonance capture yield compared to current JEFF and ENDF evaluations.

The average ratios between experimental and evaluated data (shown in the right panel of Figure 4.38) have been calculated in the two relevant energy regions and the results are given in Table 4.4.

For the purpose of this work, the unresolved resonance region begins at 5 keV in contrast to 20 keV in the JEFF-3.1.2 and ENDF/B-VII.1 libraries. The current evaluations have a 3% uncertainty in the energy range 2-9 keV. As displayed in

Table 4.4: Comparison of experimental and evaluated data for the $^{238}\text{U}(n,\gamma)$ cross section in the energy interval 3 keV - 25 keV.

Ratio of this work to	Energy region	Mean	Standard deviation
JEFF-3.1.2	2-9 keV	1.02	0.07
ENDF/B-VII.1	2-9 keV	1.02	0.07
JEFF-3.1.2	9-20 keV	0.95	0.05
ENDF/B-VII.1	9-20 keV	0.95	0.05

Table 4.4, our data confirm the evaluations (agreement within the 3% uncertainty of the evaluations), and suggest a slight increase in the cross section by 2% (within the limit of our uncertainty, which is 3% below 9 keV). A close look to the ratios between n_TOF data and the evaluations reveals large discrepancies (up to 24% around 6 keV) that are worth a deeper investigation. A comparison of the individual resonances in the energy intervals concerned does not provide any hint about these differences; thus it is one of the issues to be studied in detail during the forthcoming combined analysis of all the new measurements carried out within the ANDES project.

In the second energy region of interest, 9-25 keV, the uncertainty in the evaluations is considered 9% therefore the evaluations are not as accurate as at lower energies. As explained in Section 4.1.3, our data analysis is limited to 20 keV. The values summarised in Table 4.4 suggest that the evaluated cross section in this region should be reduced by $\sim 5\%$, which within the uncertainty of the evaluations is significant according to the uncertainty of our data (3.7% in this region).

If this 5% decrease of the cross section is confirmed by the other transmission and capture measurements within ANDES, the uncertainty in the cross section between 9 and 25 keV should be reduced from the current 9% to only 3.7%, which is the target of the ANDES project, following the suggestion of the NEA-HPRL.

CHAPTER 5

Summary and conclusions

There is a pressing need to improve the accuracy of the present evaluated $^{238}\text{U}(\text{n},\gamma)$ cross section. Although previous high accuracy measurements have been performed, the uncertainty still remains high for this key isotope due to differences between experimental data sets. In particular, previous experimental capture data has had to be adjusted for the evaluations in order to be in agreement with high quality transmission data.

As part of the ANDES project, new measurements have been performed with the goal of reducing the overall uncertainty in the $^{238}\text{U}(\text{n},\gamma)$ cross section. This manuscript has presented the measurement using the TAC detection system at the n_TOF facility. These new measurements are very timely as there is currently a new international evaluation underway on ^{238}U as part of the CIELO project.

The combination of the world class neutron time-of-flight facility n_TOF, a high efficiency calorimeter utilising cutting edge analysis techniques and a highly pure ^{238}U sample has allowed a very accurate cross section measurement to be performed. The $^{238}\text{U}(\text{n},\gamma)$ cross section has been successfully measured with the TAC detection system at the n_TOF facility, CERN in the energy range 0.3 eV - 20 keV. Within this manuscript, the n_TOF facility has been described in detail with a focus on all elements which are crucial to this cross section measurement, especially the Total Absorption Calorimeter detection set-up. The stages of the analysis from raw signals to a capture yield have been documented in detail highlighting all sources of systematic uncertainty that could affect the final result. The main steps in the calculation of the capture yield have been:

- Beam-off and sample out background subtraction, which has been performed through dedicated measurements.
- Pile-up and dead-time effects, which have been corrected for using an inno-

vative Monte Carlo technique which replicates the full capture cascades and their detection and event reconstruction processes, allowing one to apply the correction for variable count rates and any analysis conditions in deposited energy and multiplicity.

- The background subtraction from neutrons scattered by the sample, which has been subtracted using an experimental technique of measuring a carbon sample, considered a pure scatterer and comparing this deposited energy spectrum to that of ^{238}U .
- The normalisation of the capture yield, which has been determined by means of the Saturated Resonance Method which has an uncertainty of less than 1%.

The resulting capture yield has been assigned a maximum uncertainty of 3.7% in the neutron energy region above 5 keV and 2% below this energy, making it one of the most accurate measurements performed of this quantity. A resonance analysis has been performed up to 5 keV with the code SAMMY, where the good energy resolution of n-TOF and the high statistics collected have allowed resonances to be easily resolved. Furthermore, the capture yield has been analysed as unresolved up to 20 keV, an unprecedented high neutron energy limit for the TAC detection system. The resulting capture yield has been compared extensively to the available evaluations. The results are always in agreement with the evaluations within the given evaluated uncertainties, however some differences are apparent which are larger than the uncertainties quoted for this measurement. In the energy region 2-9 keV, the capture cross section is found to be on average 2% above the evaluations whereas in energy region 9-20 keV the capture cross section measured is found to be systematically 5% lower.

The performed resonance analysis using the code SAMMY has highlighted some systematic differences between these results and that of the evaluations. The new calculated resonance parameters and resulting resonance kernels are in worse agreement with the evaluations for the strongest resonances, that is the ones with the largest scattering to capture ratio. It is not clear if this is a problem with the present data analysis (for example the multiple scattering correction method implemented in SAMMY) or the evaluations as previous measurements used thicker samples and also used SAMMY to perform a resonance analysis therefore this issue deserves further investigation. For the purpose of this work, resonances with a larger strength are conservatively assigned a larger uncertainty.

It is worth noting that the measured cross section presented within this manuscript is the first to agree with the evaluated cross section over the whole energy range

of interest (0.3 eV-20 keV) within accepted uncertainties without any external or unexplained normalisation (see Section 1.6).

The results of this work will be rigorously validated against the measurement of the same sample at the same facility with the C_6D_6 detectors to allow even higher accuracies to be reached for this cross section. As a final stage of the ANDES project, in a second step, the TAC and C_6D_6 data shall be compared to the transmission and capture data from GELINA before a new evaluated cross section is delivered. This final goal is very timely and will contribute to the new $^{238}U(n,\gamma)$ cross section evaluation currently on-going as part of the CIELO collaborative evaluated library project.

APPENDIX A

^{238}U Resonance paramters

Table A.1: ^{238}U resonance parameters. Resonances marked with * should be assigned a larger uncertainty due to the large multiple scattering contrbution. Furthermore, the first three resonances (marked with ^a) were saturated therefore could not be correctly fitted.

Energy eV	n_TOF TAC			JEFF-3.1.2			RK Ratio TAC/JEFF
	Γ_γ meV	Γ_n meV	RK	Γ_γ meV	Γ_n meV	RK	
6.67 ^a	20.389	1.618	1.499	23.000	1.476	1.387	1.081
20.86 ^a	16.597	13.228	7.361	22.910	10.071	6.996	1.052
36.67 ^a	22.877	34.410	13.741	22.890	33.554	13.607	1.010
66.02	23.177	25.241	12.083	23.360	24.235	11.895	1.016
80.74	29.626	1.840	1.732	23.000	1.877	1.735	0.998
102.54	23.250	73.655	17.672	23.420	71.030	17.613	1.003
116.88	19.829	29.101	11.793	22.990	25.338	12.053	0.978
145.66	29.243	0.910	0.883	23.528	0.885	0.853	1.035
165.29	32.983	3.225	2.938	24.066	3.199	2.824	1.041
189.66	21.285	177.238	19.003	23.557	170.351	20.695	0.918
208.51	20.898	58.086	15.368	22.906	49.939	15.703	0.979
237.39	19.487	40.834	13.191	25.376	26.452	12.952	1.019
273.67	18.490	34.935	12.091	23.100	24.726	11.943	1.012
291.01	16.094	25.231	9.826	22.430	16.624	9.548	1.029
311.34	25.594	1.069	1.026	23.000	1.049	1.003	1.022
347.85	20.055	87.497	16.315	21.984	80.012	17.246	0.946
353.74	23.026	0.022	0.022	23.000	0.022	0.022	0.986
376.97	23.544	1.123	1.072	23.000	1.118	1.066	1.006
397.67	25.327	6.049	4.883	23.000	5.774	4.615	1.058
410.29	22.146	21.398	10.883	23.180	19.313	10.535	1.033
434.13	25.554	9.744	7.054	22.886	9.807	6.865	1.028
463.25	25.912	5.526	4.555	23.000	5.472	4.420	1.030
478.50	24.976	3.954	3.414	23.000	3.985	3.396	1.005
488.93	23.363	0.932	0.896	23.000	0.863	0.832	1.078
518.46	21.126	63.037	15.823	22.271	49.828	15.391	1.028
535.40	20.738	53.359	14.934	24.218	44.788	15.719	0.950
580.22	21.241	50.428	14.946	22.514	40.665	14.491	1.031
595.17	21.148	95.178	17.303	23.010	87.134	18.203	0.951

Continued on next page

Table A.1 – *Continued from previous page*

Energy eV	n-TOF TAC			JEFF-3.1.2			RK Ratio TAC/JEFF
	Γ_γ meV	Γ_n meV	RK	Γ_γ meV	Γ_n meV	RK	
620.10	20.870	30.363	12.368	23.080	30.575	13.152	0.940
628.68	22.757	6.322	4.947	23.000	6.714	5.197	0.952
661.33	23.019	140.168	19.772	24.370	127.151	20.451	0.967
693.20	21.008	44.961	14.318	23.033	42.365	14.921	0.960
708.42	21.607	21.584	10.798	23.289	22.196	11.365	0.950
721.70	22.758	1.317	1.245	23.000	1.475	1.386	0.898
730.28	22.941	1.052	1.006	23.000	1.027	0.983	1.024
765.19	22.563	8.096	5.958	23.000	8.923	6.429	0.927
790.95	22.481	6.529	5.060	23.000	6.694	5.185	0.976
821.74	19.972	76.103	15.820	22.280	68.386	16.805	0.941
851.17	21.551	67.965	16.363	23.379	65.291	17.215	0.950
856.28	21.568	94.979	17.576	23.197	90.531	18.466	0.952
866.63	22.542	5.801	4.614	23.000	5.973	4.741	0.973
905.23	21.792	50.760	15.246	23.000	54.654	16.188	0.942
925.31	23.468	16.113	9.554	23.000	16.717	9.681	0.987
937.25	21.360	158.293	18.820	23.660	157.788	20.575	0.915
958.76	21.078	188.362	18.957	22.862	213.125	20.647	0.918
991.86*	22.450	396.893	21.248	24.204	394.941	22.807	0.932
1006.05	23.001	0.041	0.041	23.000	0.041	0.041	1.000
1023.20	22.715	9.099	6.497	23.000	9.173	6.558	0.991
1054.71	21.335	99.050	17.554	23.000	95.601	18.540	0.947
1057.67	22.999	0.079	0.078	23.000	0.079	0.078	1.000
1098.98	20.236	18.869	9.764	23.000	21.589	11.136	0.877
1109.39	23.052	37.022	14.206	23.000	36.719	14.142	1.005
1140.61	20.837	238.035	19.159	23.000	237.350	20.968	0.914
1167.92	21.404	90.541	17.312	23.000	90.331	18.332	0.944
1177.49	22.758	64.886	16.849	23.000	66.358	17.080	0.986
1195.11	21.530	90.428	17.390	23.000	96.018	18.555	0.937
1211.40	21.706	9.553	6.634	17.557	10.569	6.597	1.006
1245.38	20.361	256.332	18.863	23.000	260.271	21.133	0.893
1267.37	23.279	29.635	13.038	23.000	29.621	12.947	1.007
1273.29	21.382	24.528	11.424	23.000	26.342	12.279	0.930
1299.33	22.818	3.901	3.331	23.000	3.932	3.358	0.992
1326.27	22.999	0.060	0.059	23.000	0.060	0.059	1.000
1336.97	23.008	0.094	0.094	23.000	0.094	0.094	1.000
1361.28	23.036	0.478	0.468	23.000	0.477	0.467	1.002
1394.18*	22.729	224.134	20.636	23.000	214.615	20.774	0.993
1405.79	23.379	71.542	17.621	23.000	74.625	17.581	1.002
1420.13	22.803	9.697	6.804	23.000	9.781	6.863	0.991
1428.36	21.422	28.095	12.154	23.000	29.644	12.951	0.938
1444.43	22.431	16.757	9.592	23.000	17.249	9.857	0.973
1474.21	20.750	137.648	18.032	23.000	124.269	19.408	0.929
1491.23	23.008	0.117	0.116	23.000	0.117	0.116	1.000
1523.11	21.908	220.866	19.931	23.000	248.743	21.053	0.947
1558.14	23.000	0.076	0.076	23.000	0.076	0.076	1.000
1565.67	23.054	5.937	4.721	23.000	5.919	4.708	1.003
1591.79	23.069	1.369	1.292	23.000	1.362	1.286	1.005
1598.35*	21.915	403.831	20.787	23.000	383.630	21.699	0.958
1623.12	20.522	103.615	17.129	23.000	103.957	18.833	0.910
1638.48	22.439	49.043	15.395	23.000	50.702	15.822	0.973

Continued on next page

Table A.1 – *Continued from previous page*

Energy eV	n-TOF TAC			JEFF-3.1.2			RK Ratio TAC/JEFF
	Γ_γ meV	Γ_n meV	RK	Γ_γ meV	Γ_n meV	RK	
1662.85	21.587	219.873	19.657	23.000	229.821	20.908	0.940
1689.18	22.294	115.763	18.694	23.000	108.485	18.977	0.985
1710.19	22.031	85.489	17.517	23.000	85.736	18.135	0.966
1723.25	23.064	19.327	10.515	23.000	19.146	10.449	1.006
1756.31	20.854	144.439	18.223	23.000	134.773	19.647	0.928
1782.76*	22.034	229.202	20.102	23.000	234.032	20.942	0.960
1783.27*	22.055	401.891	20.908	23.000	426.492	21.823	0.958
1808.81	23.407	20.981	11.064	23.000	20.560	10.856	1.019
1824.07	23.021	0.895	0.862	23.000	0.894	0.861	1.001
1846.56	23.382	12.350	8.082	23.000	12.143	7.947	1.017
1867.11	23.012	0.913	0.878	23.000	0.913	0.878	1.000
1903.31	23.564	47.643	15.766	23.000	47.261	15.471	1.019
1917.62	23.937	46.117	15.758	23.000	44.317	15.142	1.041
1954.26	23.081	4.463	3.740	23.000	4.450	3.728	1.003
1969.48*	21.644	845.241	21.103	23.000	802.001	22.359	0.944
1975.35*	22.425	507.379	21.476	23.000	474.367	21.936	0.979
2000.91	23.001	0.450	0.442	23.000	0.450	0.442	1.000
2024.23	21.036	220.750	19.206	23.000	230.905	20.917	0.918
2030.96	22.742	50.918	15.721	23.000	50.930	15.845	0.992
2053.35	23.001	0.782	0.756	23.000	0.782	0.756	1.000
2089.10	23.793	29.366	13.144	23.000	28.317	12.692	1.036
2096.74	22.539	30.239	12.914	23.000	30.894	13.184	0.979
2124.76	23.007	3.318	2.899	23.000	3.317	2.899	1.000
2146.07	23.148	74.680	17.671	23.000	75.261	17.616	1.003
2153.24*	21.886	316.904	20.472	23.000	309.043	21.407	0.956
2187.18*	22.942	565.052	22.047	23.000	602.329	22.154	0.995
2201.83*	25.771	110.405	20.894	26.804	111.096	21.594	0.968
2260.19	21.271	102.865	17.626	23.000	103.456	18.817	0.937
2264.92	23.016	6.618	5.140	23.000	6.616	5.138	1.000
2267.22	21.071	240.897	19.377	23.000	235.639	20.955	0.925
2282.47	21.634	202.175	19.543	23.000	200.699	20.635	0.947
2316.41	23.038	18.517	10.266	23.000	18.458	10.240	1.003
2353.35	22.948	52.078	15.929	23.000	52.691	16.011	0.995
2356.43	24.100	91.557	19.078	23.000	89.888	18.314	1.042
2392.48	23.220	32.732	13.584	23.000	32.591	13.484	1.007
2427.58	21.725	160.619	19.137	23.000	164.774	20.183	0.948
2447.33*	23.047	227.500	20.927	23.000	230.838	20.916	1.001
2456.45	22.938	20.746	10.893	23.000	20.777	10.916	0.998
2489.76	19.636	106.623	16.582	23.000	107.841	18.957	0.875
2509.50	23.001	0.260	0.257	23.000	0.260	0.257	1.000
2521.90	25.136	25.405	12.635	23.000	23.185	11.546	1.094
2548.83*	23.156	648.421	22.357	23.000	737.536	22.304	1.002
2560.26*	22.559	319.996	21.074	23.000	297.270	21.348	0.987
2581.75	20.281	484.704	19.466	23.000	473.150	21.934	0.887
2598.43	20.097	819.012	19.615	23.000	797.430	22.355	0.877
2620.74	23.110	51.611	15.962	23.000	51.498	15.899	1.004
2648.05	23.005	0.438	0.430	23.000	0.438	0.430	1.000
2672.88*	22.016	301.302	20.517	23.000	301.660	21.371	0.960
2697.02	22.447	37.491	14.040	23.000	37.837	14.305	0.982
2717.95	22.314	175.688	19.799	23.000	179.556	20.388	0.971

Continued on next page

Table A.1 – *Continued from previous page*

Energy eV	n-TOF TAC			JEFF-3.1.2			RK Ratio TAC/JEFF
	Γ_γ meV	Γ_n meV	RK	Γ_γ meV	Γ_n meV	RK	
2751.43	28.829	48.963	18.145	28.414	48.343	17.896	1.014
2763.35	23.635	21.407	11.233	23.000	20.792	10.920	1.029
2788.19	23.593	21.026	11.118	23.000	20.495	10.838	1.026
2805.95	23.661	12.757	8.288	23.000	12.375	8.046	1.030
2829.92	23.153	25.088	12.041	23.000	24.949	11.967	1.006
2866.23	20.829	227.719	19.084	23.000	226.098	20.876	0.914
2883.70*	21.674	736.333	21.054	23.000	672.308	22.239	0.947
2897.98	23.272	25.724	12.218	23.000	25.413	12.073	1.012
2934.39	22.986	45.212	15.239	23.000	45.271	15.251	0.999
2957.79	23.080	28.355	12.724	23.000	28.200	12.668	1.004
2969.43	22.980	4.361	3.666	23.000	4.366	3.670	0.999
3004.39	21.165	141.987	18.419	23.000	140.148	19.758	0.932
3029.45*	23.728	151.770	20.520	23.000	150.541	19.952	1.028
3044.59	22.998	3.814	3.272	23.000	3.814	3.272	1.000
3060.37	23.211	37.476	14.333	23.000	37.087	14.196	1.010
3082.21	22.996	2.921	2.592	23.000	2.922	2.593	1.000
3111.06*	24.168	222.864	21.804	23.000	233.657	20.939	1.041
3149.90*	24.077	135.252	20.439	23.000	132.010	19.587	1.043
3179.78	24.208	112.304	19.915	23.000	106.126	18.903	1.054
3189.80	20.796	123.571	17.801	23.000	125.262	19.432	0.916
3206.69	22.932	105.884	18.850	23.000	105.536	18.884	0.998
3227.44	23.053	32.018	13.403	23.000	31.903	13.365	1.003
3249.79	22.998	33.629	13.658	23.000	33.620	13.657	1.000
3280.41*	22.520	311.042	21.000	23.000	303.986	21.382	0.982
3313.01	21.569	179.620	19.257	23.000	176.439	20.348	0.946
3322.61	22.703	158.735	19.862	23.000	158.161	20.080	0.989
3334.51	23.437	125.162	19.740	23.000	123.876	19.398	1.018
3356.70	22.807	137.774	19.568	23.000	137.915	19.713	0.993
3390.42	22.920	29.909	12.976	23.000	30.009	13.021	0.997
3409.49	20.966	249.736	19.342	23.000	252.525	21.080	0.918
3414.07	23.000	1.962	1.808	23.000	1.962	1.808	1.000
3437.25*	23.764	453.730	22.582	23.000	433.927	21.842	1.034
3459.04*	22.237	745.154	21.593	23.000	750.593	22.316	0.968
3486.71	23.296	107.003	19.131	23.000	106.052	18.901	1.012
3496.92	23.030	10.152	7.046	23.000	10.136	7.036	1.001
3522.30	22.994	2.258	2.056	23.000	2.258	2.056	1.000
3543.27	22.995	0.574	0.560	23.000	0.574	0.560	1.000
3562.51*	22.216	261.139	20.475	23.000	261.635	21.141	0.968
3574.93*	21.563	452.076	20.581	23.000	452.984	21.889	0.940
3595.88	27.165	56.843	18.381	27.000	56.315	18.250	1.007
3624.44	26.995	31.189	14.470	27.000	31.158	14.465	1.000
3630.79*	22.026	570.757	21.207	23.000	560.545	22.093	0.960
3661.96	22.794	2.617	2.348	23.000	2.831	2.521	0.931
3694.28	19.816	425.783	18.935	23.000	419.173	21.804	0.868
3717.58	23.232	99.330	18.828	23.000	98.402	18.643	1.010
3735.25*	22.279	230.748	20.317	23.000	229.313	20.903	0.972
3747.60	23.001	0.915	0.880	23.000	0.914	0.879	1.000
3766.22	24.018	110.446	19.728	23.000	106.356	18.911	1.043
3783.01*	25.024	512.464	23.859	23.000	486.634	21.962	1.086
3808.32	23.014	0.602	0.587	23.000	0.602	0.587	1.001

Continued on next page

Table A.1 – *Continued from previous page*

Energy eV	n-TOF TAC			JEFF-3.1.2			RK Ratio TAC/JEFF
	Γ_γ meV	Γ_n meV	RK	Γ_γ meV	Γ_n meV	RK	
3833.08	23.008	14.070	8.731	23.000	14.065	8.728	1.000
3859.03*	24.573	625.232	23.643	23.000	611.317	22.166	1.067
3874.33*	23.850	200.785	21.318	23.000	197.662	20.603	1.035
3903.18*	21.428	309.647	20.041	23.000	311.426	21.418	0.936
3916.18	23.130	124.347	19.502	23.000	123.160	19.381	1.006
3940.91	20.072	182.373	18.082	23.000	181.962	20.419	0.886
3955.89	22.676	145.859	19.625	23.000	145.171	19.854	0.988
3963.25	23.003	0.870	0.838	23.000	0.870	0.838	1.000
3999.31	23.001	0.402	0.395	23.000	0.402	0.395	1.000
4016.17	22.996	2.087	1.914	23.000	2.088	1.914	1.000
4037.38	22.995	0.693	0.673	23.000	0.694	0.673	1.000
4042.39	23.931	82.454	18.548	23.000	80.846	17.906	1.036
4065.57	22.980	30.565	13.118	23.000	30.587	13.128	0.999
4091.59*	28.230	126.643	23.085	28.272	127.240	23.132	0.998
4126.54	22.971	45.303	15.242	23.000	45.271	15.251	0.999
4133.81	22.996	4.753	3.939	23.000	4.754	3.939	1.000
4170.24*	22.680	190.302	20.265	23.000	190.763	20.525	0.987
4180.28	23.077	34.193	13.778	23.000	34.104	13.736	1.003
4212.10	23.329	63.018	17.026	23.000	61.992	16.776	1.015
4227.24	23.009	9.652	6.800	23.000	9.652	6.799	1.000
4259.01	23.006	3.583	3.100	23.000	3.582	3.099	1.000
4301.17*	23.236	168.427	20.419	23.000	168.067	20.231	1.009
4308.59	23.003	113.832	19.136	23.000	114.253	19.146	0.999
4326.50	21.288	97.799	17.483	23.000	99.031	18.665	0.937
4336.22	22.999	13.323	8.436	23.000	13.320	8.435	1.000
4371.37	22.652	106.867	18.690	23.000	106.808	18.925	0.988
4376.48	22.944	49.723	15.700	23.000	49.792	15.733	0.998
4397.22	22.993	8.054	5.965	23.000	8.057	5.967	1.000
4437.33	22.962	112.126	19.059	23.000	111.342	19.062	1.000
4460.45	23.000	0.010	0.010	23.000	0.010	0.010	1.000
4504.22	23.010	9.129	6.536	23.000	9.124	6.533	1.000
4513.74*	23.731	661.023	22.909	23.000	648.795	22.213	1.031
4530.09	23.003	2.106	1.929	23.000	2.106	1.929	1.000
4545.41	23.307	123.825	19.615	23.000	122.512	19.365	1.013
4567.83	23.430	55.793	16.501	23.000	54.667	16.189	1.019
4595.77	23.001	37.853	14.307	23.000	37.857	14.307	1.000
4620.13	22.980	22.811	11.448	23.000	22.830	11.457	0.999
4634.38	22.953	31.255	13.234	23.000	31.313	13.260	0.998
4664.84*	26.688	156.373	22.797	26.109	153.608	22.316	1.022
4697.22	23.020	38.946	14.468	23.000	38.912	14.456	1.001
4707.36*	21.460	347.359	20.211	23.000	342.558	21.553	0.938
4729.56	22.996	35.554	13.964	23.000	35.558	13.966	1.000
4738.51	23.003	0.756	0.732	23.000	0.756	0.732	1.000
4767.88	22.961	37.624	14.259	23.000	37.716	14.287	0.998
4786.38	23.001	20.581	10.862	23.000	20.576	10.860	1.000
4801.92	22.060	190.335	19.769	23.000	190.657	20.524	0.963
4813.49	22.996	5.146	4.205	23.000	5.147	4.206	1.000
4840.93	21.661	17.357	9.636	23.000	18.712	10.318	0.934
4861.53*	23.040	283.984	21.311	23.000	282.734	21.270	1.002
4900.91	23.093	121.581	19.407	23.000	121.111	19.329	1.004

Continued on next page

Table A.1 – *Continued from previous page*

Energy eV	n_TOF TAC			JEFF-3.1.2			RK Ratio TAC/JEFF
	Γ_γ meV	Γ_n meV	RK	Γ_γ meV	Γ_n meV	RK	
4910.08	22.908	149.142	19.858	23.000	149.646	19.936	0.996
4923.36*	24.297	217.410	21.854	23.000	208.349	20.713	1.055
4957.30*	24.337	172.236	21.324	23.000	167.626	20.225	1.054
4976.12	23.026	77.876	17.771	23.000	77.804	17.752	1.001

References

- [1] IEA. World Energy Outlook, OECD Publishing. [⟨www.world-nuclear.org⟩](http://www.world-nuclear.org), 2009.
- [2] IAEA. International Atomic Energy Authority. [⟨www.iaea.org/⟩](http://www.iaea.org/).
- [3] C. Guerrero et al. Performance of the neutron time-of-flight facility n_TOF at CERN. *Eur. Phys. J A*, 49:27, 2013.
- [4] C. Guerrero et al. The n_TOF Total Absorption Calorimeter for neutron capture measurements at CERN. *Nucl. Instr. and Meth. A*, 608:424–433, 2009.
- [5] NEA-HPRL. High Priority Request List. [⟨www.nea.fr/html/dbdata/hprl⟩](http://www.nea.fr/html/dbdata/hprl).
- [6] The First Reactor, Report by United States Department of Energy. *DOE/NE-0046*, 1982.
- [7] IAEA-NDS. Experimental nuclear reaction data. [⟨www-nds.iaea.org/EXFOR⟩](http://www-nds.iaea.org/EXFOR).
- [8] IAEA-NDS. Evaluated Nuclear Data File. [⟨www-nds.iaea.org/exfor/endl00.htm⟩](http://www-nds.iaea.org/exfor/endl00.htm).
- [9] The Joint Evaluated Fission and Fusion File (JEFF-3.1). [⟨www.nea.fr/html/dbdata/JEFF⟩](http://www.nea.fr/html/dbdata/JEFF).
- [10] Japanese Evaluated Nuclear Library (JENDL). [⟨www.ndc.jaea.go.jp/jendl/j40/j40.html⟩](http://www.ndc.jaea.go.jp/jendl/j40/j40.html).
- [11] Z. G. Ge, Z. X. Zhao, H. H. Xia, Y. X. Zhuang, T. J. Liu, J. S. Zhang, and H. C. Wu. The Updated Vversion of Chinese Evaluated Nuclear Data Library (CENDL-3.1). *J. Korean Phys. Soc.*, 59:1052.
- [12] Russian Nuclear data Centre (Centr Jadernykh Danykh-CJD) BROND. [⟨www.ippe.obninsk.ru/podr/cjd/⟩](http://www.ippe.obninsk.ru/podr/cjd/).

- [13] M. Chadwick. CIELO: Goals and Timeline. *Proceedings of the 7th NEMEA Workshop on Nuclear Measurements, Evaluations and Applications.*, 2014.
- [14] T. Wright et al. High precision measurement of the $^{238}\text{U}(n,\gamma)$ cross section at the n_TOF facility, CERN. *Proceedings of the 7th NEMEA Workshop on Nuclear Measurements, Evaluations and Applications*, 2014.
- [15] G. Breit and E. Wigner. Capture of slow neutrons. *Phys. Rev.*, 49:519–531, 1936.
- [16] A. M. Lane and R. G. Thomas. R-matrix theory of nuclear reactions. *Rev. Mod. Phys.*, 30:257–353, 1958.
- [17] F. H. Frohner. Evaluation and Analysis of Nuclear Resonance Data. *JEFF Report 18, NEA/OECD*, 2000.
- [18] N.M. Larsson. Updated Users’ Guide for SAMMY: Multilevel R-matrix Fits to Neutron Data Using Bayes’ Equations. *ORNL/TM-9179/R7*, 2006.
- [19] M. C. Moxon. A Least Square Fitting program for Resonance Analysis of Neutron Transmission and Capture Data. *AEA-InTec-0470*, 1991.
- [20] R. L. Macklin and J. H. Gibbons. Capture-cross-section studies for 30-220-keV neutrons using a new technique. *Phys. Rev. C*, 159:1007, 1967.
- [21] U. Abbondanno et al. New experimental validation of the pulse height weighting technique for capture cross-section measurements. *Nucl. Instr. and Meth. A*, 521:454–467, 2004.
- [22] A. Bensussan and J. M. Salome. GELINA: A modern accelerator for high resolution neutron time of flight measurements. *Nucl. Instr. and Meth.*, 91:565–571, 1971.
- [23] M. Flaska et al. Modeling of the GELINA neutron target using coupled electronphotonneutron transport with the MCNP4C3 code. *Nucl. Instr. and Meth. A*, 531:392–406, 2004.
- [24] E. R. Gaerttner, M. L. Yeater, and R. R. Fullwood. Rensselaer Polytechnic Institute Linac Facility (RPI). *Proceedings of Symposium on Neutron Physics*, 1961.
- [25] ORELA: Oak Ridge Electron Linear Accelerator. www.phy.ornl.gov/nuclear/orela.

- [26] R. N. Silver. The Los Alamos Neutron Scattering Center. *Physica B+C*, 137:359–372, 1986.
- [27] K. Kino, M. Furusaka, F. Hiraga, T. Kamiyama, Y. Kiyanagi, K. Furutaka, S. Goko, H. Harada, M. Harada, T. Kai, A. Kimura, T. Kin, F. Kitatani, M. Koizumi, F. Maekawa, S. Meigo, S. Nakamura, M. Ooi, M. Ohta, and M. Oshima et al. *Nucl. Instr. and Meth. A*, 58:626–627, 2011.
- [28] C. Coceva, M. Frisoni, M. Magnani, and A. Mengoni. On the figure of merit in neutron time-of-flight measurements. *Nucl. Instr. and Meth. A*, 489:346–356, 2002.
- [29] E. Chiaveri et al. (The n_TOF Collaboration). Proposal for n_TOF Experimental Area 2 (EAR-2). *Proposal to the ISOLDE committee*, 2012.
- [30] M. C. Moxon. The Neutron Capture Cross Section of ^{238}U in the Energy Region 0.5 to 100 keV. *Atomic Energy Research Establishment*, 6074:385, 1967.
- [31] G. de Saussure et al. Measurement of the Uranium-238 Capture Cross-section for Incident Neutron Energies up to 100 keV. *Nucl. Sci. Eng.*, 51:385, 1973.
- [32] H. Derrien et al. New Evaluation of ^{238}U Neutron Resonance Parameters. *JAERI - Conf - 019*, 2003.
- [33] M. C. Moxon. High Energy Resolution Measurement of the ^{238}U Neutron Capture Yield in the Energy Region Between 1 and 100 keV. *Ann. nucl. Energy*, 18:567–583, 1991.
- [34] A. Trkov, G.L. Molnar, Zs. Revay, S.F. Mughabghab, R.B. Firestone, V.G. Pronyaev, A.L. Nichols, and M.C. Moxon. Revisiting the ^{238}U thermal capture cross section and gamma-ray emission probabilities from ^{23}Np decay. *Nucl. Sci. and Eng.*, 150:567–583, 2005.
- [35] F. Corvi and G. Fioni. Shape of the ^{238}U Neutron Capture Cross-Section in the Range 0.002-0.1 eV. *International Conference on Nuclear Data for Science and Technology*, 1988.
- [36] D. K. Olsen, G. de Saussure, R. B. Perez, E. G. Silver, F. C. Difilippo, R. W. Ingle, and H. Weaver. Precise Measurement and Analysis of Neutron Transmission Through Uranium-238. *Nucl. Sci. and Eng.*, 62:479–501, 1977.

- [37] A. Meister et al. Experimental Study of the Doppler Broadening of Neutron Resonances at GELINA. *International Conference on Nuclear Data for Science and Technology*, 1988.
- [38] D. K. Olsen et al. Measurement and Resonance Analysis of Neutron Transmission Through Uranium-238. *Nucl. Sci. and Eng.*, 69:202–222, 1979.
- [39] F. Corvi and G. Fioni. High Resolution Neutron Transmission Measurements on ^{235}U , ^{239}Pu and ^{238}U . *International Conference on Nuclear Data*, 1988.
- [40] Y. Kanda and M. Baba. ^{238}U Capture and Inelastic cross sections, A report by the Working Party on International Evaluation Co-operation of the NEA Nuclear Science Committee. 4.
- [41] Y. Kanda and M. Baba. OECD/NEA WPEC Subgroup 26 Final Report: "Uncertainty and Target Accuracy Assessment for Innovative Systems Using Recent Covariance Data Evaluations".
- [42] J. L. Ullman et al. Measurement of the ^{238}U Neutron-capture Cross Section and Gamma-emission Spectra from 10 eV to 100 keV Using the DANCE Detector at LANSCE. *J. Korean Phys. Soc.*, 59:1406–1409, 2011.
- [43] J. L. et al. Ullmann. Cross section and γ -ray spectra for $^{238}\text{U}(n,\gamma)$ measured with the DANCE detector array at the Los Alamos Neutron Science Center. *Phys. Rev. C*, 89:034603, 2014.
- [44] D. Cano Ott and F. Gunsing. Neutron capture cross section measurements of ^{238}U , ^{241}Am , and ^{243}Am . *Proposal to the ISOLDE and Neutron Time-Of-Flight Committee*, 2009.
- [45] Project FP7-249671 of the EURATOM FP7 ANDES. \langle www.andes-nd.eu/ \rangle .
- [46] C. Rubbia et al. A high resolution spallation driven facility at the CERN-PS to measure neutron cross sections in the interval from 1 eV to 250 MeV. *CERN/LHC/98-02*, 1998.
- [47] C. Borcea et al. Results from the Commissioning of the n_TOF Spallation Neutron Source at CERN. *Nucl. Instr. and Meth. A*, 513:524–537, 2003.
- [48] A. Carlson et al. *Proceedings from International Conference on Nuclear Data for Science and Technology 2007*.
- [49] IAEA standards. \langle <https://www-nds.iaea.org/standards/> \rangle .

- [50] M. Barbagallo, C. Guerrero, A. Tsinganis, and D. Tarrío et al. (The n_TOF Collaboration). High-accuracy determination of the neutron flux at n_TOF. *Eur. Phys. J A*, 49:156, 2013.
- [51] S. Marrone et al. A low background neutron flux monitor for the n_TOF facility at CERN. *Nucl. Instr. Meth. A*, 517:389–398, 2004.
- [52] Y. Giomataris, Ph. Rebourgeard, J.P. Robert, and G. Charpak. MICROMEGAS: a high-granularity position-sensitive gaseous detector for high particle-flux environments. *Nucl. Instr. Meth. A*, 376:29–35, 1996.
- [53] S. Andriamonje et al. A Transparent Detector for n_TOF Neutron Beam Monitoring. *J. Korean Phys. Soc.*, 59:1597, 2011.
- [54] D.B. Gayther. International intercomparison of fast neutron fluence-rate measurements using fission chamber transfer instruments. *Metrologia*, 27:221, 1990.
- [55] Physikalisch-Technische Bundesanstalt (PTB). www.ptb.de.
- [56] C. Paradela et al. (The n_TOF Collaboration). Neutron-induced fission cross section of ^{234}U and ^{237}Np measured at the CERN Neutron Time-of-Flight (n_TOF) facility. *Phys. Rev. C*, 82:034601, 2010.
- [57] F. Belloni et al. (The n_TOF Collaboration). Neutron beam imaging with an XY-micromegas detector at n_TOF at CERN. *Phys. Scr.*, 2012:014004, 2012.
- [58] A. Fasso et al. 1st workshop on Simulating Accelerator Radiation Environments. *Los Alamos Report*, LA-12835-C, 1994.
- [59] F. Gunsing. Analytical description in SAMMY of the resolution function of GELINA and n_TOF. *ND2004 (SAMMY Users' Group) Santa Fe, USA*, 2004.
- [60] U. Abbondanno et al. (The n_TOF Collaboration). The data acquisition system of the neutron time-of-flight facility n_TOF at CERN. *Nucl. Instr. Meth. A*, 538:692–702, 2005.
- [61] CERN Advanced STORage manager. castor.web.cern.ch.
- [62] K. Wisshak et al. The Karlsruhe 4π Barium Fluoride Detector. *Nucl. Instr. and Meth. A*, 292:595–618, 1990.
- [63] E. Mendoza et al. Improved neutron capture cross section measurements with the n_TOF Total Absorption Calorimeter. *J. Korean Phys. Soc.*, 59:1813–1816, 2011.

- [64] E. Berthoumieux. Preliminary report on BaF₂ Total Absorption Calorimeter test measurement. *Rap. Tech.*, 2004.
- [65] C. Guerrero et al. (The n_TOF Collaboration). Measurement and resonance analysis of the ²³⁷Np neutron capture cross section. *Phys. Rev. C*, 85:044616, 2012.
- [66] C. Carrapicio. Neutron induced capture and fission discrimination using calorimetric shape decomposition. *Nucl. Instr. and Meth. A*, 704:60–67, 2013.
- [67] M. Barbagallo et al. Results on the ²³⁶U Neutron Cross Section from the n_TOF Facility.
- [68] C. Guerrero et al. New resonant capture cross section of ²⁴⁰Pu, (in preparation).
- [69] E. Mendoza et al. Measurement of the ²⁴¹Am and the ²⁴³Am Neutron Capture Cross Sections at the n_TOF Facility at CERN. *Nucl. Data Sheets (accepted for publication)*.
- [70] F. Gunsing et al. Spin Measurements of Neutron Resonances of ⁸⁷Sr for Level Density Studies. *Nuclear Data Sheets*, 115, 2013.
- [71] C. Guerrero et al. Study of photon strength functions of actinides: the case of ²³⁵U, ²³⁸Np and ²⁴¹Pu. *J. Korean Phys. Soc.*, 59:1510–1513, 2011.
- [72] Rene Brun and Fons Rademakersb. ROOT An object oriented data analysis framework. *Nucl. Instr. and Meth. A*, 389:81–86, 1997.
- [73] C. Guerrero. Measurements of the ²³⁷Np and ²⁴⁰Pu neutron capture cross sections at the CERN n_TOF facility. *Universidad Complutense de Madrid*, Diploma thesis, Madrid 2008.
- [74] C. Massimi et al. (The n_TOF Collaboration). ¹⁹⁷Au(n,γ) cross section in the resonance region. *Phys. Rev. C*, 81:044616, 2010.
- [75] N. Colonna et al. Time-energy relation to the n_TOF neutron beam: energy standards revisited. *Nucl. Instr. and Meth. A*, 532:662–630, 2004.
- [76] E. Mendoza, C. Guerrero, E. Berthoumieux, and D. Cano-Ott. Pulse pile-up and dead time correction methods applied to the digitized signals of a segmented BaF₂ Total Absorption Calorimeter used in (n,γ) cross section measurements. *Submitted to Nucl. Instr. Meth. A*.

- [77] C. Guerrero, E. Mendoza, D. Cano-Ott, and T. Wright. A Monte Carlo based pile-up and dead-time correction method for measurements in coincidence with detector arrays. *Submitted to Nucl. Instr. Meth. A*.
- [78] Glenn F. Knoll. Radiation detection and measurements. *John Wiley and Sons*, 1978.
- [79] C. Guerrero et al. (The n_TOF Collaboration). Monte Carlo simulation of the n_TOF Total Absorption Calorimeter. *Nucl. Instr. Meth. A*, 671:108–117, 2012.
- [80] R. Macklin, J. Halperin, and R. Winters. Absolute neutron capture yield calibration. *Nucl. Instr. and Meth. A*, 164:213, 1979.
- [81] C. Guerrero et al. Application of Photon Strength Functions to (n,γ) measurements with the n_TOF TAC. *Proc. of the workshop on photon strength functions and related topics, Prague*, 2007.
- [82] F. Gunsing et al. Measurement of resolved resonances of $^{232}\text{Th}(n,\gamma)$ at the n_TOF facility at CERN. *Phys. Rev. C*, 85:064601, 2012.